QCD and electroweak NLO corrections to $\mathrm{W}+\gamma$ and $\mathrm{Z}+\gamma$ production including leptonic decays

Dissertation zur Erlangung
des naturwissenschaftlichen Doktorgrades
der Julius-Maximilians-Universität Würzburg

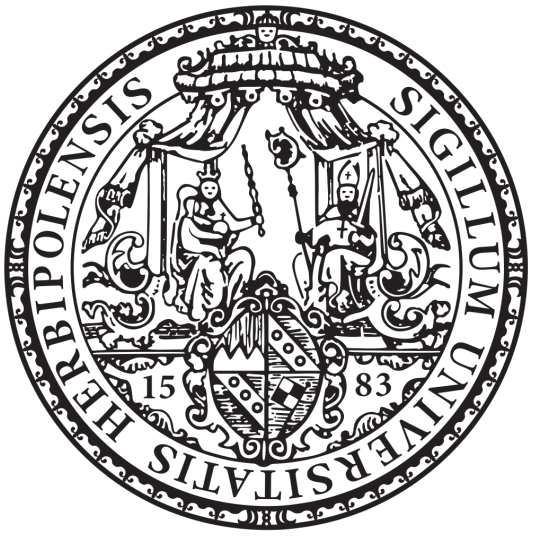

vorgelegt von

Christian Pasold

aus Ebersdorf

Würzburg 2015

Eingereicht am: 8. Dezember 2015
bei der Fakultät für Physik und Astronomie

1. Gutachter: Prof. Dr. Ansgar Denner
2. Gutachter: Prof. Dr. Raimund Ströhmer
3. Gutachter: .....
der Dissertation.

Vorsitzende(r): .....

1. Prüfer: Prof. Dr. Ansgar Denner
2. Prüfer: Prof. Dr. Raimund Ströhmer
3. Prüfer: .....
im Promotionskolloquium

Tag des Promotionskolloquiums: .....

Doktorurkunde ausgehändigt am: .....

Zusammenfassung

An einem Hadron Beschleuniger wie dem LHC oder dem Tevatron spielt die Prozessklasse der Produktion eine Photons in Kombination mit einem leptonisch zerfallenden massiven Eichbosons eine wichtige Rolle. Die Gründe für die große Bedeutung sind zum einen die klare Signatur aus einem Photon und zwei Leptonen als auch der direkte Zugang zu den Kopplungen des Photons an die massiven Eichbosonen und damit die Möglichkeit den Eichsektor des Standard-Modells der Elementarteilchenphysik zu testen.

Um die Präzision der theoretischen Vorhersagen weiter zu erhöhen wurde im Rahmen dieser Arbeit eine vollständige Berechnung der Korrekturen in nächstführender Ordnung durchgeführt. Diese umfassen alle Korrekturen der starken Wechselwirkung von $\mathcal{O}(\alpha_s)$ sowie die elektroschwachen Korrekturen von $\mathcal{O}(\alpha)$ inklusive aller photon-induzierten Beiträge. Zur Erzeugung von Matrixelementen wurde dabei auf Feynman-Diagramm basierte Methoden zurückgegriffen. Für die Behandlung der IR-Divergenzen wurde die Dipolesubtraktion verwendet wobei die Separation von kollinearen Photon–Jet-Konfigurationen mithilfe der Quark-Photon-Fragmentationsfunktion á la Glover / Morgan oder des Frixione-Kriteriums erfolgte. Außerdem wurden zwei experimentell motivierte Szenarien für die Behandlung von geladenen Leptonen im Endzustand berücksichtigt. In einem Fall werden kollineare Photon–Lepton-Paare zu einem Quasiteilchen zusammengefasst. Dieses Szenario entspricht der experimentellen Behandlung von Elektronen, die im Falle eines kollinearen Photons im elektromagnetischen Kalorimeter nicht von diesem getrennt werden können. Im zweiten Szenario werden Myonen und Photonen als experimentell separierbar angenommen, sodass Myon und Photon getrennt von einander im Detektor rekonstruiert werden können.

Für die Berechnung der Korrekturen wurden alle Beiträge in einem flexiblen Monte Carlo Programm implementiert, das neben der Berechnung des totalen Wirkungsquerschnittes auch die Erzeugung von Histogrammen für verschiedenste experimentell motivierte Observablen ermöglicht. Neben den typischen großen elektroschwachen Korrekturen bei hohen Transversalimpulsen sowie in Bereichen der Resonanzregion von transversaler beziehungsweise invarianter Masse zeigt sich, dass auch die photon-induzierten Korrekturen in der Größenordnung von einigen 10% bei hohen Transversalimpulsen beitragen. Die experimentelle Genauigkeit für Vγ Produktion in Run I mit 7/8 TeV am LHC lag bei etwa 10%. Aufgrund der gesteigerten Luminosität in Run II wird diese Genauigkeit noch weiter verbessert werden, sodass Korrekturen von $\sim 5\%$ innerhalb der theoretischen Vorhersagen nicht mehr vernachlässigt werden können. In dieser Arbeit zeigen wir Ergebnisse für den totalen Wirkungsquerschnitt am LHC für 7, 8 und 14 TeV sowie die dazugehörigen Verteilungen für 14 TeV.

Abstract

At a hadron collider as the LHC or the Tevatron the production of a photon in association with a leptonically decaying vector boson represents an important class of processes. These processes stand out due to a very clean signal of a photon and two leptons. Furthermore they provide direct access to the photon–vector-boson couplings and thus an easy opportunity to test the gauge sector of the Standard Model.

Within the scope of this work we present a full calculation of the next-to-leading-order corrections which include the $\mathcal{O}(\alpha_s)$ corrections of the strong interaction as well as the electroweak corrections of $\mathcal{O}(\alpha)$ including all photon-induced contributions. For the creation of matrix elements we use methods based on Feynman diagrams. The IR singularities are treated with the dipole subtraction technique. In order to separate photons from jets, a quark-to-photon fragmentation function á la Glover / Morgan or Frixione's cone isolation is employed. Moreover, two different scenarios for charged leptons in the final state were considered. The first scenario for dressed leptons assumes that a charged lepton and a photon will be recombined if they are collinear. In the second scenario for bare muons it is assumed that leptons and photon can be separated in a detector also if they are collinear.

For our calculation we implemented all corrections into a flexible Monte Carlo program. Besides the computation of the total cross section this program is also able to generate differential distributions of several experimentally motivated observables. Apart from the expected large electroweak corrections in the high transverse-momentum regions and sizeable corrections in the resonance regions of the transverse or the invariant masses we found photon-induced corrections up to several 10% for high transverse momenta. Within run I at the LHC for 7/8 TeV the experimental accuracy for Vγ production was roughly 10%. Due to the higher luminosity at run II this accuracy will be reduced to the level of a few percent so that corrections of the same order within the theoretical predictions might become relevant. In this work we present results for the total cross section at the LHC for 7, 8 and 14 TeV and the corresponding distributions for 14 TeV.

Contents

Introduction

With the shutdown of the Large Hadron Collider (LHC) at the end of 2014 one of the most exciting and successful time frames in particle physics ended. The first run at 7/8 TeV resulted in the discovery of the Higgs Boson [1] an so the particle content of the Standard Model (SM) of particle physics was completely approved by experiments. Until now, the SM represents the most successful theory in elementary particle physics so far. Mathematically it is a gauge theory of the strong interactions [2–4] and the electroweak (EW) interaction [5–8] including spontaneous symmetry breaking [9–13]. However, in spite of the success of the SM there are still open questions where the SM can not give an answer and it is broadly accepted that the SM is embedded as a low-energy approximation in a more fundamental description of nature. One important argument for such an approach is the possible unification of the electroweak and strong interaction or even a description of all four fundamental forces as part of one theory. Besides the unification of the electroweak and strong force and a potential connection to general relativity these beyond SM theories usually provide additional heavier particles which might be found at the LHC. In the summer of 2015 LHC started again with run II with an energy of 13 TeV. Scrutinising the properties of the Higgs boson is the most pressing task in this run but with the higher centre-of-mass energy the search of new particles beyond the SM is also possible in an unprecedented energy regime. In search of new physics beyond the SM one possible entry should be a continued detailed investigation of the EW gauge bosons. Besides the single gauge boson production in Drell–Yang processes the production of a gauge-boson pair provides an excellent possibility for various tests of the EW gauge-boson sector in the SM. The simplest gauge-boson-pair processes are the production of a vector boson in association with a photon

$$\mathrm{pp} \to \mathrm{V} + \gamma + X \to \bar{f}_1 + f_2 + \gamma + X\,, \qquad \mathrm{V} = \mathrm{W}, \mathrm{Z}\,, \tag{1}$$

where the vector boson decays leptonically. Therein the final-state fermions are $f_1, f_2 = \mathrm{e}, \mu, \nu_\mathrm{e}, \nu_\mu, \nu_\tau$.

The $\mathrm{W} + \gamma$ production process allows for direct tests of the photon coupling to W bosons and, additionally, it is an important background process to new physics searches. Since $\mathrm{W} + \gamma$ production has a total cross section in the picobarn range, it has already been measured at the Tevatron [14, 15] and the LHC [16–19]. Therein the experimental accuracies are roughly 12%.

The production of a charged lepton pair and a photon represents the dominant background to the Higgs-boson decay into a Z boson and a photon. Naturally, the Higgs-boson decay can only be measured precisely if the background processes are well under control.

The second part of $\mathrm{Z}+\gamma$ production is the process where the Z boson decays invisibly in two neutrinos. Accordingly, the experimental signature is mono-photon production in association with missing transverse energy. Such signals are relevant to the search of new physics in many exotic models (see e.g. Refs. [20–23]) and there are already several experimental analyses at the Tevatron [24, 25] and the LHC [26, 27].

$\mathrm{W}\gamma$ and $\mathrm{Z}\gamma$ production are also important background processes for the search of narrow heavy resonances [18] that decay to $\mathrm{W}\gamma$ and $\mathrm{Z}\gamma$ final states and as predicted in various new physics models (e.g. see Refs. [28, 29] for scalar particles and Ref. [30] for vector particles).

Another possible approach for the investigation of new physics effects in the electroweak gauge sector is the framework of anomalous triple gauge couplings (aTGCs). Therein the WWV, ZZV and ZγV vertices are parametrized by a set of new parameters [31]. Besides several theoretical studies (e.g. in Refs. [32,33]) the fact that so far no significant deviations between the measurements and the theoretical predictions in the SM are seen can be directly translated into limits on these parameters. Several experimental analyses reported such constraints at the Tevatron [15,34,35] and at the LHC by the experiments ATLAS [17,18] and CMS [16,36]. Due to the higher energies and luminosities in run II at the LHC an improvement of the theoretical predictions is more important than ever. Since the expected experimental uncertainties will be of the order of a few percent and because of the lacking evidence of new physics so far a further precise investigation of the SM predictions up to percent level is required.

The first calculations for $\mathrm{W}+\gamma$ [37] and $\mathrm{Z}+\gamma$ [38] production were already published more than 30 years ago. Afterwards the NLO QCD corrections for on-shell (stable) vector bosons were calculated in Refs. [39,40]. A further improvement due to the inclusion of leptonic vector-boson decays in narrow-width approximation was then achieved in Refs. [41,42]. In this approximation the NLO QCD corrections to $\mathrm{W}+\gamma$ and $\mathrm{Z}+\gamma$ production are also available in the public program `MCFM` [43]. Since the NLO QCD corrections for $\mathrm{W}+\gamma$ and $\mathrm{Z}+\gamma$ production are of the order 150% and 50%, respectively, the NNLO QCD corrections are expected to be sizeable. In Ref. [43] they were estimated to be of the order 5% due to a scale-variation analysis. The full NNLO QCD corrections for $\mathrm{V}+\gamma$ production were published in Refs. [44] and [45], respectively. These calculations show a large impact of 19–26% for Wγ and a moderate effect of 8–18% for Zγ production.

Since many years it is well known that at high energies EW corrections can cause impacts of several 10%. The origin of these effects is the existence of logarithmically enhanced contributions, so-called Sudakov logarithms [46–51]. It was shown in Ref. [52] that these EW corrections for $\mathrm{W}+\gamma$ are negative and of the order 5–20%. In Ref. [53] the NLO EW corrections were calculated for $\mathrm{Z}+\gamma$ production with on-shell Z bosons and in Ref. [54] results for NLO EW corrections to Wγ and Zγ production including the decays of the massive vector bosons in pole approximation were presented.

In this work we push the existing calculations of the EW corrections for $\mathrm{pp}\to l^+\nu_l/l^-\bar{\nu}_l+\gamma+X$ and $\mathrm{pp}\to l^+l^-/\bar{\nu}\nu+\gamma+X$ production to the level of complete NLO EW corrections including all off-shell effects and including all partonic channels with initial-state photons and we also rederive the NLO QCD corrections. Since the treatment of collinear singularities connected with photon emission of final-state leptons depends on the level of inclusiveness in the event reconstruction we consider two different scenarios. While in one scenario for dressed leptons we assume that collinear lepton–photon configurations can not be separated in a detector, in the second case describing final-state muons we suppose that the collinear photon is absorbed in the electromagnetic calorimeter and the muon is detected in the muon chamber. Finally, both particles can be separated also if they are collinear. The calculation of photon-induced and QCD corrections requires the separation of photons and jets in the final state. For an infrared-safe separation we use the concept of democratic clustering in combination with a quark-to-photon fragmentation function [55,56] or alternatively the Frixione isolation criterion [57].

In order to calculate the necessary amplitudes in the 't Hooft–Feynman gauge we use traditional methods based on Feynman diagrams. We employ the Weyl–van-der-Waerden spinor formalism as formulated in Ref. [58] for the numerical evaluation of the amplitudes. For the numerical calculation of the loop integrals the `COLLIER` library [59] is used, which is based on the results of Refs. [60–62] and involves two different independent implementations of all one-loop integrals. The amplitude calculation is based on the program `POLE` [52], which internally uses `FEYNARTS` 3 [63,64] and `FORMCALC` [65] for the generation of the amplitudes. The numerical integration is performed by the multi-channel phase-space generator `LUSIFER` [66] extended to

use VEGAS [67, 68] in order to optimize each phase-space mapping.

This thesis is organized as follows:

- In Chapter 1 we discuss the theoretical basics required for NLO calculations. We start with the Lagrangian of the Standard Model of particle physics. Additionally, we outline the procedure of renormalization. Therein we focus on the complex-mass scheme which we consistently use in this work. Furthermore, we briefly outline the parton model and we discuss its extension for the purpose of NLO calulations.

- Chapter 2 contains the definition of the partonic processes for $W\gamma$ and $Z\gamma$ production. Starting from the leading-order processes and their partonic content we also discuss the virtual and the real corrections. We show structural Feynman diagrams of the different types of contributions and we discuss the difficulties of the respective contributions.

- One of the main challenges during a NLO calculation is the treatement of IR divergencies which appear in the virtual and the real corrections. Since we consistently use the dipole subtraction formalism in this work we summarize the basic concept of the procedure in Chapter 3. Therein we discuss the different fermion–photon splittings and list the most important formulae for the emitter-spectator combinations which are used in this work. Finally, we outline our strategies for the treatment of collinear photon–jet configurations.

- In Chapter 4 we present the results of our work. First, we introduce the setup in which the calculation was performed and we define the different classes of QCD and EW corrections. Afterwards we list results for the total cross section for 7, 8 and 14 TeV. Moreover, we present several distributions for 14 TeV for $W\gamma$ and $Z\gamma$ production. Additionally, we discuss the differences between $W^+\gamma$ and the charge-conjugate process $W^-\gamma$ production. The results of this chapter have been published in Refs. [69] and [70].

- In Appendix A we outline the Monte Carlo method which is used for the numerical phase-space integration. After summarizing the general procedure we discuss the explicit phase-space decomposition which was used in all calculations.

- Appendix B contains a short overview about the numerical evaluation of one-loop integrals as well as the reduction of tensor integrals as it is implemented in the library COLLIER [59] and which we used in this work.

- In Appendix C we list distributions for $W^-\gamma$ production. The distributions of this charge-conjugated process show very similar shapes as the ones for $W^+\gamma$ production. As an addendum we show in the comparison of $W^+\gamma$ and $W^-\gamma$ production for additional observables.

- Appendix D presents further distributions for the dilepton + photon production which also might be relevant for experimental analyses.

Chapter 1

Theoretical background

1.1 The Standard Model of particle physics

Due to its great accordance with experimental measurements the Standard Model (SM) of particle physics is one of the most established theories so far. It is a relativistic quantum field theory which describes the strong and electroweak interaction between elementary particles and it is formulated as a local non-Abelian gauge theory with the underlying gauge group

$$\mathrm{SU(3)_C} \times \mathrm{SU(2)_w} \times \mathrm{U(1)_Y}\,. \tag{1.1}$$

Therein $\mathrm{SU(3)_C}$ indicates the gauge group of the strong force whose fundamental theory is quantum chromodynamics (QCD) [2–4]. It describes the interaction between quarks and gluons as well as the gluon self-interaction which is a result of the non-Abelian structure of the group. The group $\mathrm{SU(2)_w} \times \mathrm{U(1)_Y}$ is the gauge group of the electroweak (EW) interaction which is the unification of the electromagnetic and the weak forces. The fundamental theory is the Glashow-Salam-Weinberg (GSW) Model [5,7,8]. The particle content of the SM is summarized in Table 1.1.

Fermions				Bosons
Family	1	2	3	g
Quarks	u	c	t	$\mathrm{W}^{\pm}$
	d	s	b	Z
Leptons	e	μ	τ	γ
	ν_e	ν_μ	ν_τ	H

Table 1.1: Particle content of the Standard Model of particle physics. Fermions are divided in quarks and leptons and are organized in three families. While quarks interact via QCD and EW interactions the leptons only couple to the gauge bosons of the EW interaction.

The fermionic fields of matter appear in three generations for quarks and leptons where the number is not predicted by the SM, but from experiments we know that there are exactly three light neutrinos [71]. The particles of each row only differ in its masses but have the same quantum numbers. While the masses for the quarks and charged leptons increase from left to right all neutrinos in high-energy experiments are considered to be massless [1]. The gauge boson

[1] Since in the SM right-handed neutrinos do not exist even with a Yukawa coupling neutrinos remain massless. However, from the observation of solar neutrinos and their oscillation between the different flavour eigenstates it is known, that neutrinos have non-vanishing masses. One solution would be to simply add right-handed neutrinos leading up to usual Dirac mass terms. There is also the possibility that neutrinos fulfil the Majorana equation resulting in Majorana mass terms which would be an indication for physics beyond the SM.

fields are the mediator particles of the strong (gluons) and electroweak ($W^{\pm}$, Z, γ) interaction.

From experiments it is known that W and Z boson are massive, but the naive introduction of mass terms for gauge bosons in the Lagrangian would violate the gauge symmetry. Therefore the generation of gauge-boson masses in the EW sector of the SM is performed by the Higgs–Kibble mechanism [9–13]. Therein the $\mathrm{SU(2)_w \times U(1)_Y}$ gauge symmetry is spontaneously broken by the introduction of a scalar field with non-vanishing vacuum expectation value whereby an invariance under the electromagnetic subgroup $\mathrm{U(1)_{em}}$ is preserved. According to the Goldstone theorem [72] three of the four gauge bosons become massive and the remaining massless boson can be identified with the photon.

In order to generate fermion masses the naive way would be the addition of fermion mass terms to the Lagrangian. Since such terms are not invariant under $\mathrm{SU(2)_w \times U(1)_Y}$ transformation these terms are forbidden. The generation of fermion masses is implemented by so-called Yukawa-interaction terms which provide the most general renormalizable interaction between fermions and the Higgs field. The couplings of the Higgs field with the massive W and Z bosons are generated automatically by the covariant derivative in $\mathcal{L}_{\mathrm{H}}$.

Finally, the EW Lagrangian $\mathcal{L}_{\mathrm{EW}}$ for the SM is given by

$$\mathcal{L}_{\mathrm{EW}} = \mathcal{L}_{\mathrm{YM}} + \mathcal{L}_{\mathrm{F}} + \mathcal{L}_{\mathrm{H}}\,, \tag{1.2}$$

where the Yang-Mills part $\mathcal{L}_{\mathrm{YM}}$, the fermionic part $\mathcal{L}_{\mathrm{F}}$ and the Higgs part $\mathcal{L}_{\mathrm{H}}$ are separately gauge invariant. Thereby the Yukawa-interaction terms are included in $\mathcal{L}_{\mathrm{H}}$. Following the conventions in Ref. [73] each of the parts will be discussed in one of the following sections. Note, that the fermion part $\mathcal{L}_{\mathrm{F}}$ only contains the EW interaction of fermions. The interaction of quarks and of gluons via QCD is included in $\mathcal{L}_{\mathrm{QCD}}$ and will be discussed in Section 1.1.5, separately.

1.1.1 The Yang–Mills sector

The Yang–Mills part $\mathcal{L}_{\mathrm{YM}}$ describes the kinematical properties of the four gauge fields W^a_μ, ($a = 1, 2, 3$) and B_μ of the gauge group $\mathrm{SU(2)_w \times U(1)_Y}$. Thereby W^a_μ denotes the isotriplet of the weak isospin group $\mathrm{SU(2)_w}$ with its generators I^a_{W}. B_μ indicates the isosinglet of $\mathrm{U(1)_Y}$ with the hypercharge Y_{W}. The electric charge operator Q is related to I^3_{W} and Y_{W} via the Gell-Mann–Nishijima relation

$$Q = I^3_{\mathrm{W}} + \frac{Y_{\mathrm{W}}}{2}\,. \tag{1.3}$$

The corresponding Lagrangian of the Yang–Mills part is given by

$$\mathcal{L}_{\mathrm{YM}} = -\frac{1}{4}(\partial_\mu W^a_\nu - \partial_\nu W^a_\mu + g_2 \varepsilon^{abc} W^b_\mu W^c_\nu)^2 - \frac{1}{4}(\partial_\mu B_\nu - \partial_\nu B_\mu)^2\,, \tag{1.4}$$

where g_2 and ε^{abc} are the coupling constant and the total antisymmetric structure constant of $\mathrm{SU(2)_w}$. The covariant derivative reads

$$D_\mu = \partial_\mu - i g_2 I^a_{\mathrm{W}} W^a_\mu + i g_1 \frac{Y_{\mathrm{W}}}{2} B_\mu\,, \tag{1.5}$$

where g_1 is the coupling constant of $\mathrm{U(1)_Y}$.

1.1.2 The fermionic sector

In the SM weakly interacting left-handed fermions are arranged as isospin doublets $\Psi'_i = (\Psi'_{i,+}, \Psi'_{i,-})$ of the weak isospin group $\mathrm{SU(2)_w}$. The index $\pm$ is only used to distinguish between the two entries in the doublet and i indicates one of the three lepton or quark families. Each

right-handed fermion field is arranged in a one-dimensional trivial representation of $\mathrm{SU}(2)_\mathrm{w}$. The prime in our notation at Ψ' denotes the explicit basis where the covariant derivative (defined in Eq. (1.5)) is diagonal. In general, the Ψ' are not mandatory mass eigenstates.

We introduce left-handed and right-handed fermion fields as

$$\Psi'^L = \frac{1}{2}(1-\gamma_5)\Psi' \,, \qquad \Psi'^R = \frac{1}{2}(1+\gamma_5)\Psi' \,, \tag{1.6}$$

where left-handed fields live in the fundamental two-dimensional representation of $\mathrm{SU}(2)_\mathrm{w}$ with the generator $I^a_\mathrm{W} = \sigma^a/2$ and σ^a denote the Pauli matrices given by

$$\sigma^1 = \begin{pmatrix} 0 & 1 \\ 1 & 0 \end{pmatrix} , \qquad \sigma^2 = \begin{pmatrix} 0 & -i \\ i & 0 \end{pmatrix} , \qquad \sigma^3 = \begin{pmatrix} 1 & 0 \\ 0 & -1 \end{pmatrix} . \tag{1.7}$$

Right-handed fermions are associated with the trivial one-dimensional representation of $\mathrm{SU}(2)_\mathrm{w}$ with $I^a_\mathrm{W} = 0$ so that the g_2-term in Eq. (1.5) vanishes. The hypercharge is chosen such that the correct electric charge results from the Gell-Mann–Nishijima relation in Eq. (1.3).

Assuming the common convention where the left-handed doublets for leptons and quarks are written as

$$L'^L_i = \begin{pmatrix} \nu'^L_i \\ l'^L_i \end{pmatrix} , \qquad Q'^L_i = \begin{pmatrix} u'^L_i \\ d'^L_i \end{pmatrix} \tag{1.8}$$

and the right-handed singlets are l'^R_i, u'^R_i and d'^R_i the fermionic Lagrangian reads

$$\begin{aligned} \mathcal{L}_\mathrm{F} = &\sum_i \left(\bar{L}'^L_i i \not{D} L'^L_i + \bar{Q}'^L_i i \not{D} Q'^L_i \right) \\ &+ \sum_i \left(\bar{l}'^R_i i \not{D} l'^R_i + \bar{u}'^R_i i \not{D} u'^R_i + \bar{d}'^R_i i \not{D} d'^R_i \right) , \end{aligned} \tag{1.9}$$

where we used the common abbreviation $\not{D} = \gamma^\mu D_\mu$ and $i = 1, 2, 3$ denotes the generation index for leptons or quarks.

1.1.3 The Higgs sector

In the previous section we outlined the interaction between gauge bosons and fermions and we also mentioned before that naive mass terms of these particles are forbidden. In order to generate masses of gauge bosons and fermions we use the so-called Higgs mechanism to break the $\mathrm{SU}(2)_\mathrm{w} \times \mathrm{U}(1)_\mathrm{Y}$ symmetry in such a way that the electromagnetic symmetry $\mathrm{U}(1)_\mathrm{em}$ remains. Therefore we introduce a complex scalar weak-isospin doublet, the Higgs doublet. In order to achieve one neutral component of this doublet the hypercharge has to be $Y_\mathrm{W} \pm 1$ (following directly from Eq. (1.3)). We use the common choice of $Y_\mathrm{W} + 1$ so that the Higgs doublet contains a positive and a neutral component

$$\Phi(x) = \begin{pmatrix} \phi^+(x) \\ \phi^0(x) \end{pmatrix} . \tag{1.10}$$

The generation of gauge-boson masses is then implemented through the gauge-invariant coupling of the Higgs doublet with the gauge bosons. Additionally it also couples to the fermion via Yukawa couplings and creates the masses of all leptons and quarks. The corresponding Higgs part of the Lagrangian reads

$$\begin{aligned} \mathcal{L}_\mathrm{H} = &(D_\mu \Phi)^\dagger (D^\mu \Phi) - V(\Phi) \\ &- \sum_{i,j} (\bar{L}'^\mathrm{L}_i G^l_{ij} l'^\mathrm{R}_j \Phi + \bar{Q}'^\mathrm{L}_i G^u_{ij} u'^\mathrm{R}_j \Phi^c + \bar{Q}'^\mathrm{L}_i G^d_{ij} d'^\mathrm{R}_j \Phi + \mathrm{h.c.}) \,, \end{aligned} \tag{1.11}$$

where we introduced the Higgs potential

$$V(\phi) = \frac{\lambda}{4}\left(\Phi^\dagger\Phi\right)^2 - \mu^2\Phi^\dagger\Phi\,, \qquad \mu^2, \lambda > 0\,, \tag{1.12}$$

which describes the self-interaction of the scalar Higgs doublet with the coupling λ and the mass term μ^2. The G^f_{ij} denote the Yukawa coupling matrices of the fermion f and the charged conjugated Higgs doublet is defined by $\Phi^c = i\sigma^2\Phi^* = (\phi^{0*}(x), \phi^-(x))$. The covariant derivative D_μ was already introduced in Eq. (1.5).

The Higgs self-interaction (see Eq. (1.12)) leads to a non-vanishing vacuum expectation value (vev)

$$|\langle\Phi\rangle|^2 = \frac{2\mu^2}{\lambda} \equiv \frac{v^2}{2} \neq 0\,. \tag{1.13}$$

To ensure that after breaking the $\mathrm{SU(2)_w \times U(1)_Y}$ symmetry a $\mathrm{U(1)_{em}}$ is still preserved the non-vanishing vev should only appear in the neutral component of the Higgs doublet. Therefore we demand

$$Q\Phi_0 = \left(\frac{\sigma^3}{2} + \frac{Y_\mathrm{W}}{2}\right)\Phi_0 = \begin{pmatrix} 1 & 0 \\ 0 & 0 \end{pmatrix}\begin{pmatrix} \phi_{01} \\ \phi_{02} \end{pmatrix} = 0\,, \tag{1.14}$$

with the solution

$$\Phi_0 = \begin{pmatrix} 0 \\ \frac{v}{\sqrt{2}} \end{pmatrix}\,, \tag{1.15}$$

where the global complex phase was set to one. The solution Φ_0 is neither invariant under $\mathrm{SU(2)_w}$ nor under $\mathrm{U(1)_Y}$. With the aid of Eq. (1.15) the Higgs doublet in Eq. (1.10) can be expanded as

$$\Phi(x) = \begin{pmatrix} \phi^+(x) \\ \frac{1}{\sqrt{2}}[v + \eta(x) + i\chi(x)] \end{pmatrix}\,, \qquad \phi^-(x) = [\phi^+(x)]^\dagger\,. \tag{1.16}$$

Therein the fields $\eta(x)$ and $\chi(x)$ as well as $\phi^+(x)$ and $\phi^-(x)$ have vanishing vev. $\chi(x)$, $\phi^+(x)$ and $\phi^-(x)$ are the unphysical degrees of freedom called would-be Goldstone fields which can be eliminated by choosing the unitary gauge. $\eta(x)$ represents the physical massive scalar Higgs particle which is part of the SM particle content.

1.1.4 Physical fields

The easiest way to determine the particle content of the electroweak SM is to choose the unitary gauge $\phi^\pm = 0$ and $\chi = 0$ where all unphysical degrees of freedom vanish. In this gauge the physical ones can be indentified with the eigenstates of mass and charge. Therefore we insert $\Phi(x)$ from Eq. (1.16) using the unitary gauge into the Higgs part of the Lagrangian (1.11)

$$\begin{aligned}\mathcal{L}_\mathrm{H} =& \frac{1}{4}v^2 g_2^2 W^-_\mu W^{+\mu} + \frac{1}{8}v^2(g_2 W^3_\mu + g_1 B_\mu)(g_2 W^{3\mu} + g_1 B^\mu) \\ &+ \frac{1}{2}(\partial_\mu\eta)(\partial^\mu\eta) - \mu^2\eta^2 + \text{ trillinear and quadrilinear terms} \\ &- \frac{1}{\sqrt{2}}(v+\eta)\sum_{i,j}(\bar{l}'^\mathrm{L}_i G^l_{ij} l'^\mathrm{R}_j + \bar{u}'^\mathrm{L}_i G^u_{ij} u'^\mathrm{R}_j + \bar{d}'^\mathrm{L}_i G^d_{ij} d'^\mathrm{R}_j + \text{h.c.})\,.\end{aligned} \tag{1.17}$$

Hence, we can directly read off from the second term in line 2 the mass of the Higgs boson as $M_\mathrm{H} = \sqrt{2}\mu$. We used the charge eigenstates $W^\pm_\mu$ instead of $W^{1/2}_\mu$ which are defined as

$$W^\pm_\mu = \frac{1}{\sqrt{2}}[W^1_\mu \mp iW^2_\mu]\,. \tag{1.18}$$

The physical states of the neutral bosons can be determined by diagonalizing the mass matrix via

$$\begin{pmatrix} A_\mu \\ Z_\mu \end{pmatrix} = \begin{pmatrix} c_\mathrm{W} & -s_\mathrm{W} \\ s_\mathrm{W} & c_\mathrm{W} \end{pmatrix} \begin{pmatrix} B_\mu \\ W_\mu^3 \end{pmatrix} , \tag{1.19}$$

with the Weinberg angle

$$c_\mathrm{W} \equiv \cos\theta_\mathrm{W} = \frac{g_2}{\sqrt{g_2^2 + g_1^2}} , \qquad s_\mathrm{W} \equiv \sin\theta_\mathrm{W} . \tag{1.20}$$

Finally, for the masses of the gauge bosons we obtain

$$M_Z = \frac{v}{2}\sqrt{g_1^2 + g_2^2} , \qquad M_\gamma \equiv M_A = 0 , \qquad M_W = g_2 \frac{v}{2} , \tag{1.21}$$

where A_μ is massless and can be identified with the photon, Z is the massive neutral gauge boson with mass M_Z and M_W denotes the masses of the charged W bosons following directly from the first term of line 1 in Eq. (1.17).

The generation of fermion masses is also induced by spontaneous symmetry breaking. The fermion fields $f_i'^{\mathrm{L/R}}$ denote the eigenstates for lepton, up-type quarks and down-type quarks of the EW interaction. The connection between $f_i'^{\mathrm{L/R}}$ and the physical states is given by

$$f_i^\mathrm{L} = \sum_k U_{ik}^{f,\mathrm{L}} f_k'^\mathrm{L} , \qquad f_i^\mathrm{R} = \sum_k U_{ik}^{f,\mathrm{R}} f_k'^\mathrm{R} . \tag{1.22}$$

Therein $U_{ik}^{f,\mathrm{L/R}}$ denotes the matrices which diagonalizes the Yukawa couplings G_{ij}^f so that the fermion masses are

$$m_{f,i} = \frac{v}{\sqrt{2}} \sum_{k,m} U_{ik}^{f,\mathrm{L}} G_{km}^f (U_{mi}^{f,\mathrm{R}})^\dagger . \tag{1.23}$$

From this equation it follows directly that due to the absence of right-handed neutrinos no gauge-invariant Yukawa interaction term for neutrinos exists and so in the SM neutrinos remain massless. Because of that we can choose an arbitrary neutrino matrix $U_{ik}^{l,\mathrm{L}}$. We employ

$$\nu_i^\mathrm{L} = \sum_k U_{ik}^{l,\mathrm{L}} \nu_k'^\mathrm{L} , \tag{1.24}$$

in such a way that all lepton–W-boson interaction terms are diagonal in $\mathcal{L}_\mathrm{H}$. In contrast, the interaction terms between up-type or down-type quarks and W bosons is altered by additional factors

$$V_{ij} = \sum_k U_{ik}^{u,\mathrm{L}} U_{kj}^{d,\mathrm{L}\dagger} . \tag{1.25}$$

This unitary matrix characterizes the mixing between different quark families and is known as the Cabibbo–Kobayashi–Maskawa (CKM) matrix.

With the relations summarized in this section the parameter set given by g_1, g_2, λ, μ^2, G^l, G^u and G^d can be transformed into an alternative collection

$$e,\, M_\mathrm{W},\, M_\mathrm{Z},\, M_\mathrm{H},\, m_{f,i},\, V_{ij} , \tag{1.26}$$

whose values are directly accessible by experimental measurements. Thereby the electric charge e is defined as $e = \sqrt{4\pi\alpha}$ and its relation to g_1 and g_2 is given by

$$e = \frac{g_1 g_2}{g_1^2 + g_2^2} . \tag{1.27}$$

1.1.5 QCD Lagrangian

The gauge group of the SM given in Eq. (1.1) also includes the colour group $\mathrm{SU(3)_C}$ which describes the strong interaction between quarks and gluons known as quantum chromodynamics. Gluons are the gauge bosons of the $\mathrm{SU(3)_C}$ and quarks transform as triplets in the fundamental representation. Because of the non-Abelian structure of the group $\mathrm{SU(3)_C}$ self-interaction of the gluons exists. The QCD Lagrangian reads

$$\mathcal{L}_{\mathrm{QCD}} = -\frac{1}{4}(\partial_\mu G^a_\nu - \partial_\nu G^a_\mu + g_s f^{abc} G^b_\mu G^c_\nu)^2 + \sum_{q,cc'} \bar{\psi}_{q,c}(i\not{D}_{cc'} - m_q \delta_{cc'})\psi_{q,c'}\,, \tag{1.28}$$

where the first term is a Yang-Mills Lagrangian describing the kinematic properties of gluons. The strong coupling constant $g_s = \sqrt{4\pi\alpha_s}$ is defined analogous to e in Section 1.1.4. f^{abc} denote the structure constants of the $\mathrm{SU(3)_C}$ and their generators are the Gell-Mann matrices λ^a with $a = 1, ..., 8$. Furthermore $\mathcal{L}_{\mathrm{QCD}}$ contains a second term which characterizes the interaction between quarks and gluons. Therein $\psi_{q,c}$ indicates the quark fields with flavour $q = u, d, s, c, b, t$ and colour index c. The quark mass is labeled by m_q and the covariant derivative is defined as

$$D_{\mu,cc'} = \partial_\mu \delta_{cc'} - i\frac{g_s}{2}\lambda^a_{cc'} G^a_\mu\,, \tag{1.29}$$

where in $\mathcal{L}_{\mathrm{QCD}}$ we used $\not{D}_{cc'} = \gamma^\mu D_{\mu,cc'}$. Note that since we discuss the QCD and EW Lagrangians separately the partial derivative ∂_μ appears two times in Eqs. (1.5) and (1.29). However, in the total Lagrangian (which combines the EW and the QCD part) it only appears once.

1.1.6 Gauge fixing, Faddeev-Popov ghosts and quantization

Theoretical predictions in perturbation theory require to define Feynman propagators for gauge bosons. Therefore we have to choose a specific gauge for the gauge bosons which leads to an additional gauge-fixing term $\mathcal{L}_{\mathrm{fix}}$ in the Lagrangian. In order to ensure the independence of the specific gauge fixing we follow the procedure introduced by Faddeev and Popov [74] where a second term $\mathcal{L}_{\mathrm{FP}}$ is added to the Lagrangian. Then, the effective renormalizable Lagrangian for EW and QCD are given by

$$\begin{aligned}\mathcal{L}_{\mathrm{EW,eff.}} &= \mathcal{L}_{\mathrm{EW}} + \mathcal{L}_{\mathrm{EW,fix}} + \mathcal{L}_{\mathrm{EW,FP}}\,,\\ \mathcal{L}_{\mathrm{QCD,eff.}} &= \mathcal{L}_{\mathrm{QCD}} + \mathcal{L}_{\mathrm{QCD,fix}} + \mathcal{L}_{\mathrm{QCD,FP}}\,,\end{aligned} \tag{1.30}$$

with $\mathcal{L}_{\mathrm{EW}}$ and $\mathcal{L}_{\mathrm{QCD}}$ defined in Eqs. (1.2) and (1.28).

EW theory

Choosing the linear gauge fixing (R_ξ-gauge)

$$\begin{aligned}F^\pm &= (\xi^{\mathrm{W}}_1)^{-\frac{1}{2}}\partial^\mu W^\pm_\mu \mp i M_{\mathrm{W}}(\xi^{\mathrm{W}}_2)^{\frac{1}{2}}\phi^\pm\,,\\ F^{\mathrm{Z}} &= (\xi^{\mathrm{Z}}_1)^{-\frac{1}{2}}\partial^\mu \mathrm{Z}^\mu - M_{\mathrm{Z}}(\xi^{\mathrm{Z}}_2)^{\frac{1}{2}}\chi\,,\\ F^\gamma &= (\xi^\gamma_1)^{-\frac{1}{2}}\partial^\mu A_\mu\,,\end{aligned} \tag{1.31}$$

and the 't Hooft gauge with $\xi^\alpha_1 = \xi^\alpha_2 = 1$ leads to the gauge fixing Lagrangian

$$\mathcal{L}_{\mathrm{EW,fix}} = -\frac{1}{2}\left[(F^\gamma)^2 + (F^{\mathrm{Z}})^2 + 2F^+F^-\right]. \tag{1.32}$$

The effects of the $\mathcal{L}_{\text{EW,fix}}$ will be compensated by the Faddeev–Popov term

$$\mathcal{L}_{\text{EW,FP}} = \bar{u}^{\alpha}(x)\frac{\delta F^{\alpha}}{\delta\theta^{\beta}}u^{\beta}(x)\,, \tag{1.33}$$

where $\bar{u}^{\alpha}(x)$ and $u^{\beta}(x)$ $(\alpha,\beta = \pm, \text{Z}, \gamma)$ denote the Grassmann-valued ghost fields which are independent of each other. δF^{α} indicates the variation of the gauge fixing operator under an infinitesimal transformation $\delta\theta^{\beta}$.

QCD

Following the same strategy as for the EW theory we choose a specific gauge fixing

$$F^{\text{G}} = (\xi^{\text{G}})^{-\frac{1}{2}}\partial^{\mu}G_{\mu}\,, \tag{1.34}$$

with the corresponding Lagrangian

$$\mathcal{L}_{\text{QCD,fix}} = \frac{1}{2}(F^{\text{G}})^2\,. \tag{1.35}$$

The Faddeev–Popov term in QCD is

$$\mathcal{L}_{\text{QCD,FP}} = -\bar{u}^{a}(x)\partial^{\mu}D^{ab}_{\mu}u^{c}(x)\,, \tag{1.36}$$

where we introduced D^{ac}_{μ} $(a,c = 1,...,8)$ as

$$D^{ac}_{\mu} = \partial_{\mu}\delta^{ac} - g_s f^{abc}G^{b}_{\mu}\,. \tag{1.37}$$

1.2 Renormalization

In Section 1.1 we discussed the Lagrangian of the SM which depends on a set of parameters defined in Eq. (1.26). At tree-level these parameters are directly accessible by experimental measurements. However, going to next-to-leading order (NLO) this is no longer the case. More specifically, this means: the original "bare" parameters appearing in the Lagrangian and the measured values differ by a UV-divergent part and finite contributions depending on the explicit scheme. In order to make the parameters in the Lagrangian again accessible by experimental measurements it is necessary to redefine them. This redefinition is called *renormalization*.

1.2.1 General procedure

A priori, two steps have to be done during the renormalization procedure:

1. redefinition of fields and parameters and
2. solve renormalization conditions

leading to finite propagators and Green's functions. For the functional relation between the bare parameter and the renormalized one we use the counterterm approach

$$\mathcal{P}_0 = \mathcal{P} + \delta\mathcal{P}\,, \tag{1.38}$$

where $\mathcal{P}_0$ is the original unrenormalized parameter. $\mathcal{P}$ is the renormalized one which can be related to the experimentally measured value and $\delta\mathcal{P}$ denotes the renormalization constant (counterterm) which contains the UV-divergent component and finite contributions, depending

on the renormalization scheme. The counterterm will be fixed by a renormalization condition which relates the bare parameter and the renormalized parameter. In general, this condition can be chosen in a wide range but the choice of the renormalization condition affects the physical predictions. Finally, after applying the counterterm approach to all parameters and fields a renormalized Lagrangian can be deployed via

$$\mathcal{L}_0 = \mathcal{L} + \delta\mathcal{L}\,. \tag{1.39}$$

Therein $\mathcal{L}_0$ and $\mathcal{L}$ have the same form but $\mathcal{L}$ depends on the renormalized parameters and fields instead of the unrenormalized ones. $\delta\mathcal{L}$ contains the additional contribution resulting from the renormalization constants.

1.2.2 The complex-mass scheme

In this thesis we focus on the Wγ and Zγ production processes including the leptonic decay of the vector bosons so that W and Z bosons only appear as intermediate unstable particles. Therefore we need a description of particle resonances in perturbation theory. This requires a Dyson summation of self-energy insertions which automatically leads to a mixing of different orders in perturbation theory, thus, potentially breaking gauge invariance. For a proper description of the resonant vector-boson propagators we use the complex-mass scheme (CMS) [75–77] where the masses of the vector bosons are consistently treated as complex quantities

$$\mu_{\mathrm{W}}^2 = M_{\mathrm{W}}^2 - iM_{\mathrm{W}}\Gamma_{\mathrm{W}}\,, \qquad \mu_{\mathrm{Z}}^2 = M_{\mathrm{Z}}^2 - iM_{\mathrm{Z}}\Gamma_{\mathrm{Z}}\,, \tag{1.40}$$

defined as the propagator poles in the complex plane. These complex values will be used in all propagators and couplings of the Lagrangian. The CMS fully respects gauge invariance and consequently the underlying Ward identities are fulfilled and no dependence on the gauge fixing procedure remains. As a consequence of Eq. (1.40) the EW mixing angle becomes complex as well

$$c_{\mathrm{W}}^2 \equiv \cos^2\theta_{\mathrm{W}} = 1 - s_{\mathrm{W}}^2 = \frac{\mu_{\mathrm{W}}^2}{\mu_{\mathrm{Z}^2}}\,. \tag{1.41}$$

The application of the CMS at tree-level by using Eqs. (1.40) and (1.41) in the Born amplitudes leads to additional terms of $\mathcal{O}(\Gamma_{\mathrm{V}}/M_{\mathrm{V}}) = \mathcal{O}(\alpha)$ (see Ref. [76]) which are formally part of the NLO contribution.

We now follow the procedure explained in Section 1.2.1. Initially, the real bare parameters of the vector-boson masses are expressed by renormalized complex masses and complex counterterms

$$M_{\mathrm{W},0}^2 = \mu_{\mathrm{W}}^2 + \delta\mu_{\mathrm{W}}^2\,, \qquad M_{\mathrm{Z},0}^2 = \mu_{\mathrm{Z}}^2 + \delta\mu_{\mathrm{Z}}^2 \tag{1.42}$$

and the vector boson fields also are split in a complex field and a complex renormalization constant

$$\mathrm{W}_0^{\pm} = (1+\delta\mathcal{Z}_{\mathrm{W}})\mathrm{W}^{\pm}\,, \qquad \begin{pmatrix}\mathrm{Z}_0\\ \mathrm{A}_0\end{pmatrix} = \begin{pmatrix}1+\frac{1}{2}\delta\mathcal{Z}_{\mathrm{ZZ}} & \frac{1}{2}\delta\mathcal{Z}_{\mathrm{ZA}}\\ \frac{1}{2}\delta\mathcal{Z}_{\mathrm{AZ}} & 1+\frac{1}{2}\delta\mathcal{Z}_{\mathrm{AA}}\end{pmatrix}\begin{pmatrix}\mathrm{Z}\\ \mathrm{A}\end{pmatrix}\,. \tag{1.43}$$

We outline the renormalization procedure in the CMS for all values which are used in the explicit calculation of Wγ and Zγ production. Since the renormalization of the Higgs mass, the Higgs field and the mass of the top quark are not relevant for our needs, we will not discuss their renormalization. As a first step we introduce the renormalized transverse (T) gauge-boson

self-energies $\hat{\Sigma}$ as

$$\begin{aligned}
\hat{\Sigma}_{\mathrm{T}}^{\mathrm{W}}(k^2) &= \Sigma_{\mathrm{T}}^{\mathrm{W}}(k^2) - \delta\mu_{\mathrm{W}}^2 + (k^2 - \mu_{\mathrm{W}}^2)\delta\mathcal{Z}_{\mathrm{W}}\,, \\
\hat{\Sigma}_{\mathrm{T}}^{\mathrm{ZZ}}(k^2) &= \Sigma_{\mathrm{T}}^{\mathrm{ZZ}}(k^2) - \delta\mu_{\mathrm{Z}}^2 + (k^2 - \mu_{\mathrm{Z}}^2)\delta\mathcal{Z}_{\mathrm{ZZ}}\,, \\
\hat{\Sigma}_{\mathrm{T}}^{\mathrm{AA}}(k^2) &= \Sigma_{\mathrm{T}}^{\mathrm{AA}}(k^2) + k^2\delta\mathcal{Z}_{\mathrm{AA}}\,, \\
\hat{\Sigma}_{\mathrm{T}}^{\mathrm{AZ}}(k^2) &= \Sigma_{\mathrm{T}}^{\mathrm{AZ}}(k^2) + k^2\frac{1}{2}\delta\mathcal{Z}_{\mathrm{AZ}} + (k^2 - \mu_{\mathrm{Z}}^2)\frac{1}{2}\delta\mathcal{Z}_{\mathrm{ZA}}\,,
\end{aligned} \tag{1.44}$$

where Σ denotes the corresponding unrenormalized self-energy. The photon field is labeled as A. $\mu_{\mathrm{W}}^2/\mu_{\mathrm{Z}}^2$ and $\delta\mu_{\mathrm{W}}^2/\delta\mu_{\mathrm{Z}}^2$ describe the renormalized complex vector-boson masses and the complex counterterms, respectively, which are defined in Eq. (1.42).

The mass counterterms are fixed by the following renormalization conditions

$$\hat{\Sigma}_{\mathrm{T}}^{\mathrm{W}}(\mu_{\mathrm{W}}^2) = 0\,, \qquad \hat{\Sigma}_{\mathrm{T}}^{\mathrm{ZZ}}(\mu_{\mathrm{Z}}^2) = 0\,, \tag{1.45}$$

so that the renormalized masses are equal to the location of the propagator poles in the complex plane of the momenta. The solutions of these conditions are

$$\delta\mu_{\mathrm{W}}^2 = \Sigma_{\mathrm{T}}^{\mathrm{W}}(\mu_{\mathrm{W}}^2)\,, \qquad \delta\mu_{\mathrm{Z}}^2 = \Sigma_{\mathrm{T}}^{\mathrm{ZZ}}(\mu_{\mathrm{Z}}^2)\,. \tag{1.46}$$

The following conditions

$$\begin{aligned}
&\hat{\Sigma}_{\mathrm{T}}^{\mathrm{AZ}}(0) = 0\,, \qquad \hat{\Sigma}_{\mathrm{T}}^{\mathrm{AZ}}(\mu_{\mathrm{Z}}^2) = 0\,, \\
&\hat{\Sigma}_{\mathrm{T}}^{\prime\mathrm{W}}(\mu_{\mathrm{W}}^2) = 0\,, \qquad \hat{\Sigma}_{\mathrm{T}}^{\prime\mathrm{ZZ}}(\mu_{\mathrm{Z}}^2) = 0\,, \qquad \hat{\Sigma}_{\mathrm{T}}^{\prime\mathrm{AA}}(0) = 0\,,
\end{aligned} \tag{1.47}$$

fix the field renormalization constants. The explicit results are

$$\begin{aligned}
&\delta\mathcal{Z}_{\mathrm{ZA}} = \frac{2}{\mu_{\mathrm{Z}}^2}\Sigma_{\mathrm{T}}^{\mathrm{AZ}}(0)\,, \qquad \delta\mathcal{Z}_{\mathrm{AZ}} = -\frac{2}{\mu_{\mathrm{Z}}^2}\Sigma_{\mathrm{T}}^{\mathrm{AZ}}(\mu_{\mathrm{Z}}^2)\,, \\
&\delta\mathcal{Z}_{\mathrm{W}} = -\Sigma_{\mathrm{T}}^{\prime\mathrm{W}}(\mu_{\mathrm{W}}^2)\,, \qquad \delta\mathcal{Z}_{\mathrm{ZZ}} = -\Sigma_{\mathrm{T}}^{\prime\mathrm{ZZ}}(\mu_{\mathrm{Z}}^2)\,, \qquad \delta\mathcal{Z}_{\mathrm{AA}} = -\Sigma_{\mathrm{T}}^{\prime\mathrm{AA}}(0)\,,
\end{aligned} \tag{1.48}$$

where we used the abbreviation $\Sigma_{\mathrm{T}}^{\prime}(x) = \partial\Sigma_{\mathrm{T}}/\partial p^2|_{p^2=x}$. $\delta\mathcal{Z}_{\mathrm{W}}$ applies to W^+ and W^- fields because the sign of its imaginary part is fixed by the conditions in Eq. (1.47) and does not change when going from W^+ to W^-.

The renormalization of the complex weak mixing angle is applied via

$$c_{\mathrm{W},0} = c_{\mathrm{W}} + \delta c_{\mathrm{W}}\,, \qquad s_{\mathrm{W},0} = s_{\mathrm{W}} + \delta s_{\mathrm{W}}\,. \tag{1.49}$$

From its definition in Eq. (1.41) it can be easily derived that

$$\frac{\delta s_{\mathrm{W}}}{s_{\mathrm{W}}} = -\frac{c_{\mathrm{W}}^2}{s_{\mathrm{W}}^2}\frac{\delta c_{\mathrm{W}}}{c_{\mathrm{W}}} = -\frac{c_{\mathrm{W}}^2}{2s_{\mathrm{W}}^2}\left(\frac{\delta\mu_{\mathrm{W}}^2}{\mu_{\mathrm{W}}^2} - \frac{\delta\mu_{\mathrm{Z}}^2}{\mu_{\mathrm{Z}}^2}\right)\,. \tag{1.50}$$

For the renormalization of the fermion fields we use

$$f_0^\sigma = (1 + \frac{1}{2}\delta\mathcal{Z}_{f,\sigma})f^\sigma\,, \qquad \sigma = \mathrm{L},\mathrm{R}\,, \tag{1.51}$$

where the explicit renormalization constants read

$$\delta\mathcal{Z}_{f,\sigma} = -\Sigma^{f,\sigma}(m_f^2) - m_f^2\left[\Sigma^{\prime f,\mathrm{R}}(m_f^2) + \Sigma^{\prime f,\mathrm{L}}(m_f^2) + 2\Sigma^{\prime f,\mathrm{S}}(m_f^2)\right]\,, \quad \sigma = \mathrm{L},\mathrm{R}\,. \tag{1.52}$$

Therein the calculation of the self-energies is applied with the complex weak mixing and complex vector-boson masses from Eqs. (1.41) and (1.40) so that $\delta\mathcal{Z}_{f,\sigma}$ becomes complex itself. In

Eq. (1.52) the superscripts R, L and S describe the right-handed, left-handed and scalar parts of the self-energies. Note, that even in the limit $m_f^2 \to 0$ the second term in Eq. (1.52) leads to finite contributions due to terms $\propto 1/m_f^2$ in $\Sigma'^{f,\sigma}(m_f^2)$.

For the renormalization of the electric charge we start with

$$e_0 = e + \delta e = e\left(1 + \delta\mathcal{Z}_e\right). \tag{1.53}$$

The renormalization constant can be derived from the eeγ-vertex in the Thomson limit (subscript $\alpha(0)$). In CMS it reads

$$\delta\mathcal{Z}_e\big|_{\alpha(0)} = \frac{\delta e}{e}\Big|_{\alpha(0)} = \frac{1}{2}\Sigma_{\mathrm{T}}^{\prime\mathrm{AA}}(0) - \frac{s_{\mathrm{W}}}{c_{\mathrm{W}}}\frac{\Sigma_{\mathrm{T}}^{\mathrm{AZ}}(0)}{\mu_{\mathrm{Z}}^2}. \tag{1.54}$$

The masses and couplings are treated as complex quantities in the loop integrals and so $\delta\mathcal{Z}_e$ also becomes complex. Assuming that the bare value of the electric charge e_0 is real the imaginary part has to vanish and therefore the imaginary part of $\delta\mathcal{Z}_e$ is directly related to the imaginary part of the self-energies. While the dominant contributions to Wγ and Zγ production arise from regions of the phase space where the vector bosons are on their mass-shell the Thomson limit describes the energy region with $p^2 \to 0$. In order to consider the running of α from this limit to the EW scale $p^2 = M_{\mathrm{W}}^2$ we have to deal with logarithms of the fermion masses inducing large corrections proportional to $\alpha\ln(m_f^2/\hat{s})$ (for more details see Ref. [76]). Following Ref. [76, 78] we use the G_{F}-scheme where α can be derived from the experimental measured G_μ by

$$\alpha_{G_\mu} = \frac{\sqrt{2}}{\pi}G_\mu M_{\mathrm{W}}^2\left(1 - \frac{M_{\mathrm{W}}^2}{M_{\mathrm{Z}}^2}\right) = \alpha\,(0)\,(1 + \Delta r)\,, \tag{1.55}$$

where we introduce (for details see Ref. [79])

$$\begin{aligned}\Delta r =& \Sigma_{\mathrm{T}}^{\prime\mathrm{AA}}(0) - \frac{c_{\mathrm{W}}^2}{s_{\mathrm{W}}^2}\left(\frac{\Sigma_{\mathrm{T}}^{\mathrm{ZZ}}(\mu_{\mathrm{Z}}^2)}{\mu_{\mathrm{Z}}^2} - \frac{\Sigma_{\mathrm{T}}^{\mathrm{W}}(\mu_{\mathrm{W}}^2)}{\mu_{\mathrm{W}}^2}\right) + \frac{\Sigma_{\mathrm{T}}^{\mathrm{W}}(0) - \Sigma_{\mathrm{T}}^{\mathrm{W}}(\mu_{\mathrm{W}}^2)}{\mu_{\mathrm{W}}^2} \\ &+ 2\frac{c_{\mathrm{W}}}{s_{\mathrm{W}}}\frac{\Sigma_{\mathrm{T}}^{\prime\mathrm{AZ}}(0)}{\mu_{\mathrm{Z}}^2} + \frac{\alpha}{4\pi s_{\mathrm{W}}^2}\left(6 + \frac{7 - 4s_{\mathrm{W}}^2}{2s_{\mathrm{W}}^2}\ln c_{\mathrm{W}}^2\right) \\ =& \Delta\alpha - \frac{c_{\mathrm{W}}^2}{s_{\mathrm{W}}^2}\Delta\rho + \Delta r_{\mathrm{rem}}\,,\end{aligned} \tag{1.56}$$

where $\Delta\alpha$ contains the corrections proportional to $\alpha\ln(m_f^2/\hat{s})$, $\Delta\rho$ denotes the corrections to the ρ-parameter which contains corrections $\propto m_t^2$ from a large mass splitting in the top–bottom isospin doublet. All other terms are represented by the remainder Δr_{rem}. In our calculation we then use the modified renormalization constant

$$\delta\mathcal{Z}_e\big|_{\alpha(0)} \longrightarrow \delta\mathcal{Z}_e\big|_{G_{\mathrm{F}}} = \delta\mathcal{Z}_e\big|_{\alpha(0)} - \frac{1}{2}\Delta r\,, \tag{1.57}$$

which considers the effect of the running α from the Thomson limit to the EW scale.

In this thesis we assume external leptons and quarks as massless stable particles so that we do not have to renormalize their masses. Since Wγ and Zγ production are purely EW processes at LO we do not discuss the renormalization of the strong coupling constant α_s.

1.3 The parton model

The empiric fact that quarks and gluons can never appear as asymptotic states (colour confinement) allows scattering experiments only between colourless external bound states of the

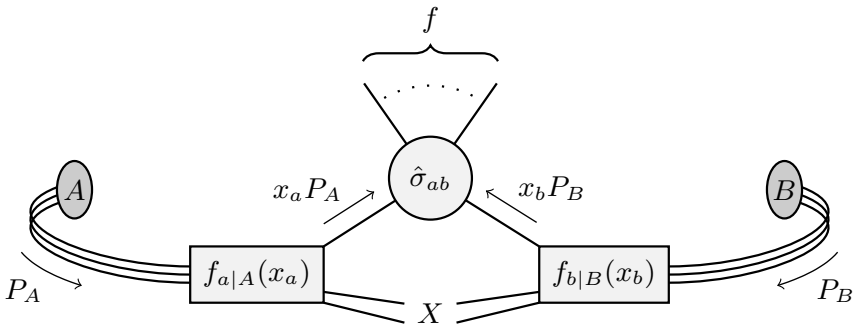

Figure 1.1: A schematic representation of the hadronic scattering process defined in (1.58), where f denotes the FS configuration of interest and X captures any additional activity from the hadron remnants. Image taken from Ref. [82].

strong interaction. The description of the structure of these bound states, called hadrons, is not possible within perturbation theory and the knowledge about their constituents results from experimental measurements. However, a theoretical description is provided by the so-called parton model [80, 81], where hadrons are assumed to be strongly coupled, composite objects. Their point-like constituents are called partons and can by identified with quarks and gluons. Theoretical predictions about scattering processes with external hadrons then also require the precise description of the hard scattering process which defines the perturbatively accessible interaction between the hadron constituents (quarks and gluons).

1.3.1 Hadronic cross section

In high-energy collisions the masses of the hadrons and the partons can be neglected and the parton model allows to factorise the hadronic cross section into process-independent non-perturbative contributions capturing the structure of the hadrons and a partonic cross section of the hard scattering process which can be calculated with purely perturbative methods. In order to describe the calculation of the hadronic cross section we start with the following generic process

$$A\left(p_A\right) + B\left(p_B\right) \to f + X\,, \tag{1.58}$$

where the two incoming hadrons A and B with momenta p_A and p_B are moving fast along the beam axis so that their transverse momenta are zero. f denotes the final-state (FS) particles of the hard scattering process and X represents the remnants of the two initial-state (IS) hadrons. The hadronic scattering process is illustrated in Fig. 1.1.

The momenta of the incoming partons a and b are related to the hadron momenta via

$$p_a = x_a p_A\,, \qquad p_b = x_b p_B\,, \tag{1.59}$$

where x_a, x_b describe the momentum factions $x_{a/b}\,\epsilon\,[0,1]$. At leading-order (LO) the hadronic cross section is defined as

$$\mathrm{d}\sigma_{AB\to f}(p_A, p_B) = \sum_{a,b} \int_0^1 \mathrm{d}x_a \int_0^1 \mathrm{d}x_b \Big[f^{(0)}_{a|A}(x_a) f^{(0)}_{b|B}(x_b)\, \mathrm{d}\hat{\sigma}^0_{ab\to f}(p_a, p_b) \Big]\,, \tag{1.60}$$

where $\hat{\sigma}^0_{ab\to f}$ denotes the Born-level partonic cross section of the process $ab \to f$ which is free of any IR singularities. $f^{(0)}_{a|A}$ and $f^{(0)}_{b|B}$ represent the non-perturbative parton distribution functions (PDFs) describing the number density for finding a parton a/b with the momentum

fraction x_a/x_b of the corresponding hadron. The PDFs are universal meaning that they are completely independent of the actual scattering process. They can be extracted e.g. from lepton–nucleon deep-inelastic scattering (DIS) experiments and then can be used to calculate theoretical predictions of proton–proton collisions at the LHC. In Eq. (1.60) the integration over x_a/x_b is done over the range $[0,1]$ and the sum $\sum_{a,b}$ considers all possible pairs $\{a,b\}$ of IS partons.

1.3.2 Labratory and partonic centre-of-mass frame

Since we choose the beam axis along the x_3-direction the four-momenta of the IS hadrons can be parametrized in the centre-of-mass frame of the hadrons via

$$p_A^\mu = \frac{\sqrt{s}}{2}(1,0,0,+1)\,, \qquad p_B^\mu = \frac{\sqrt{s}}{2}(1,0,0,-1)\,, \tag{1.61}$$

where $s = (p_A + p_B)^2$ denotes the squared hadronic centre-of-mass energy. With the partonic momenta defined in Eq. (1.59) it follows

$$p_a^\mu = x_a\frac{\sqrt{s}}{2}(1,0,0,+1)\,, \qquad p_b^\mu = x_b\frac{\sqrt{s}}{2}(1,0,0,-1)\,. \tag{1.62}$$

The centre-of-mass frame of the hadrons is also called laboratory (lab) frame and the momenta in this frame are used for the event selection and the histogram binning. However, usually the partonic cross section is calculated in the centre-of-mass frame of the partons. In order to transform the momenta between both frameworks, the lab frame and the partonic centre-of-mass frame we define the boost parameter

$$\beta_{ab} = \frac{k_a^3 + k_b^3}{k_a^0 + k_b^0}\,, \tag{1.63}$$

where $k_{a/b}$ describe the momenta of the partons a and b in the lab frame and the superscript "0" and "3" indicate the zeroth and third component. The momenta k_i^μ of the FS particles then can be transformed from the lab frame to the centre-of-mass frame of the partons via

$$\begin{aligned}
\hat{k}_i^0 &= \gamma_{ab}\left(k_i^0 - \beta_{ab}\,k_i^3\right)\,,\\
\hat{k}_i^1 &= k_i^1\,,\\
\hat{k}_i^2 &= k_i^2\,,\\
\hat{k}_i^3 &= \gamma_{ab}\left(k_i^3 - \beta_{ab}\,k_i^0\right)\,,
\end{aligned} \tag{1.64}$$

where the centre-of-mass momenta are labeled by a hat and $\gamma_{ab} = \sqrt{1-\beta_{ab}^2}$. For the momenta of the IS partons we find

$$\hat{p}_a^\mu = \frac{\sqrt{\hat{s}}}{2}(1,0,0,+1)\,, \qquad \hat{p}_b^\mu = \frac{\sqrt{\hat{s}}}{2}(1,0,0,-1)\,, \tag{1.65}$$

where the partonic centre-of-mass energy is defined by $\hat{s} = x_a x_b s \equiv \tau s$.

1.3.3 Partonic cross section

On the experimental side the differential partonic cross section $\mathrm{d}\hat{\sigma}^0_{ab\to f}$ introduced in Eq. (1.60) can be formulated as a purely phenomenological quantity with

$$\frac{\mathrm{d}\hat{\sigma}_{ab\to f}}{\mathrm{d}\mathcal{O}_j} = \frac{1}{\mathcal{L}_{\text{in}}}\frac{\mathrm{d}n_f(\mathcal{O}_j)}{\mathrm{d}\mathcal{O}_j}\,, \tag{1.66}$$

where $\mathcal{L}_{\text{in}}$ represents the luminosity of the incoming particles and the quantity $\mathcal{O}_j$ describes an experimentally well-defined observable derived from the momenta of the FS particles in the lab frame. n_f denotes the number of events per time which is directly related to the integrated cross section via

$$n_f = \mathcal{L}_{\text{in}} \int \mathrm{d}\mathcal{O}_j \left[\frac{\mathrm{d}\hat{\sigma}_{ab\to f}}{\mathrm{d}\mathcal{O}_j} \right] \equiv \mathcal{L}_{\text{in}}\, \hat{\sigma}_{ab\to f}\,. \tag{1.67}$$

On the theoretical side the unpolarized integrated partonic cross section can be expressed as

$$\hat{\sigma}_{ab\to f}(p_a, p_b) = \frac{1}{2\hat{s}} \int \mathrm{d}\Phi_{(n)}(p_a, p_b; k_1, \ldots, k_n) \overline{|\mathcal{M}_{ab\to f}(\hat{p}_a, \hat{p}_b; \hat{k}_1, \ldots, \hat{k}_n)|^2}\, F^{(n)}(\{\mathcal{O}_j\})\,, \tag{1.68}$$

where $\hat{s} = (p_a + p_b)^2$ denotes the squared partonic centre-of-mass energy. The function $F^{(n)}$ symbolizes the application of the event selection cuts acting on a set of well-defined observables $\{\mathcal{O}_j\}$. It equals one if an event passes the cuts and equals zero otherwise. The phase space integration (based on the parton momenta in the lab frame) is described by $\Phi_{(n)}$ and is usually performed by Monte Carlo methods (for technical details see Chapter A). In Eq. (1.68) $\overline{|\mathcal{M}_{ab\to f}|^2}$ represents the scattering amplitudes,

$$\overline{|\mathcal{M}_{ab\to f}|^2} = \frac{1}{n(c_a)n(c_b)n(\sigma_a)n(\sigma_b)} \sum_{c_a,c_b} \sum_{c_f} \sum_{\sigma_a,\sigma_b} \sum_{\sigma_f} |\mathcal{M}_{ab\to f}|^2\,, \tag{1.69}$$

averaged over colours ($c_{a/b}$) and helicities ($\sigma_{a/b}$) of the IS partons and summed over colours and polarizations of the FS particles. In case that the final state contains m identical particles the r.h.s. of Eq. (1.69) has to be multiplied by $(1/m!)$.

1.3.4 Parton model for NLO calculations

The naive parton model described so far proceeds on the assumption that all IS partons are considered to be massless. However, in calculations beyond LO this would lead to IR singularities originating from collinear splittings of IS partons so that the hadronic cross section defined in Eq. (1.60) with an NLO partonic cross section including IR singularities is not IR-safe. The cancellation of the IR singularities as specified by the KLN theorem [83, 84] requires an inclusive treatment of all external states. Since in the naive parton model the case where IS hadrons cause collinear splittings in the initial state is not captured a fully inclusive treatment is not possible. Accordingly this would result in an incomplete cancellation of singularities with collinear origin.

The singular structure of IS collinear divergences turns out to be universal, meaning that they are independent of the specific scattering process. Therefore they can be attributed to the partonic structure of the hadrons by a redefinition of the PDFs. This procedure is similar to the renormalization discussed in Section 1.2. The PDFs $f^0_{a|A}$ introduced in Eq. (1.60) then are considered to be bare distributions and the collinear singularities are absorbed by a redefinition $f^0_{a|A}(x_a) \to f^{\text{F.S.}}_{a|A}(x_a, \mu^2_{\text{F}})$. In order to illustrate the shape of PDFs we show in Fig. 1.2 the distributions $x f_{a|P}(x, \mu^2_{\text{F}})$ for the factorization scale $\mu_{\text{F}} = M_{\text{Z}}$ provided by the NNPDF2.3QED NLO set [85].

The hadronic cross section then can be generalized to

$$\mathrm{d}\sigma_{AB\to f}(p_A, p_B) = \sum_{a,b} \int_0^1 \mathrm{d}x_a \int_0^1 \mathrm{d}x_b \Big[f^{\text{F.S.}}_{a|A}(x_a, \mu^2_{\text{F}}) f^{\text{F.S.}}_{b|B}(x_b, \mu^2_{\text{F}})\, \mathrm{d}\hat{\sigma}_{ab\to f}(p_a, p_b, \mu^2_{\text{F}}) \Big]\,, \tag{1.70}$$

where "F.S." indicates the factorization scheme and μ^2_{F} is the factorization scale. The IR-safe partonic cross section is denoted by $\hat{\sigma}_{ab\to f}$. It can be derived from the "bare" partonic cross section via

$$\hat{\sigma}_{ab\to f}(p_a, p_b, \mu^2_{\text{F}}) = \sigma_{ab\to f}(p_a, p_b) + \sigma^{\text{C}}_{ab\to f}(p_a, p_b, \mu^2_{\text{F}})\,. \tag{1.71}$$

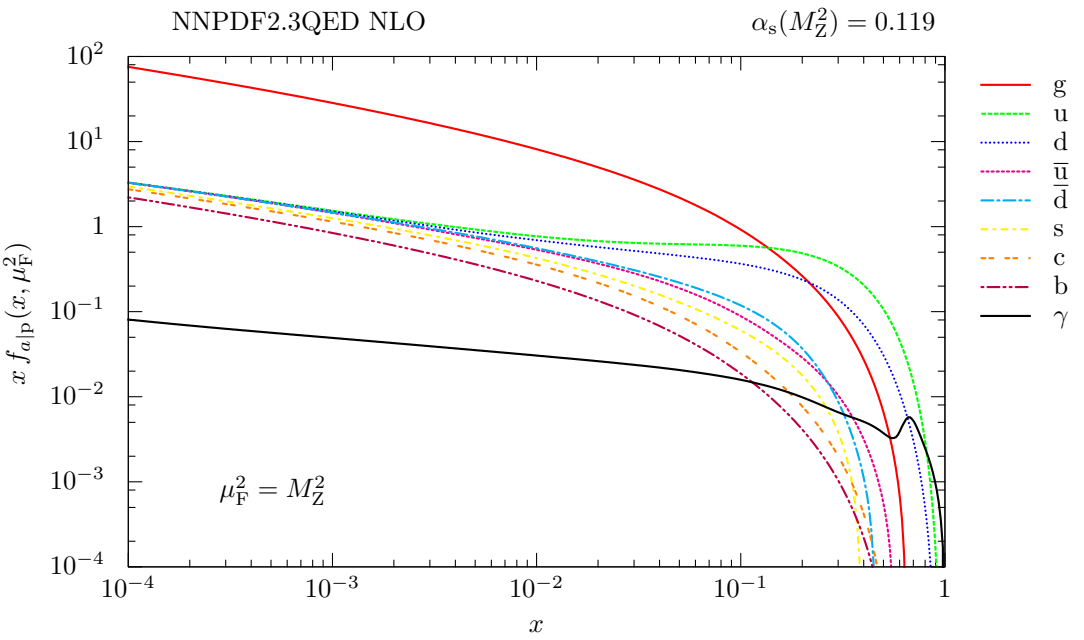

Figure 1.2: The momentum distribution of the parton inside the proton as described by the NNPDF2.3QED NLO PDF set. Image taken from Ref. [82].

Therein the long-distance contributions $\sigma^{\mathrm{C}}_{ab\to f}(p_a, p_b, \mu_F^2)$ caused by IS singularities were removed from the "bare" partonic cross section and absorbed into the redefinition of the PDFs.

The redefinition of the PDFs (f_q and f_γ) is then given by

$$\begin{aligned} f_{q|P}(x) \to\ & f_{q|P}\left(x, \mu_F^2\right) - \frac{\alpha Q_q^2}{2\pi} \int_x^1 \frac{\mathrm{d}z}{z} f_{q|P}^{\mathrm{F.S.}}\left(\frac{x}{z}, \mu_F^2\right) \\ & \times \left\{ \ln\left(\frac{\mu_F^2}{m_q^2}\right) \left[P_{ff}(z)\right]_+ - \left[P_{ff}(z)\left(2\ln(1-z)+1\right)\right]_+ + C_{ff}^{\mathrm{F.S.}}(z) \right\} \\ & - 3\frac{\alpha Q_q^2}{2\pi} \int_x^1 \frac{\mathrm{d}z}{z} f_{\gamma|P}\left(\frac{x}{z}, \mu_F^2\right) \left\{ \ln\left(\frac{\mu_F^2}{m_q^2}\right) P_{f\gamma}(z) + C_{f\gamma}^{\mathrm{F.S.}} \right\}, \end{aligned} \tag{1.72}$$

for quarks and the analogous redefinition for antiquarks. The redefinition of the photon-PDF reads

$$\begin{aligned} f_{\gamma|P}(x) \to\ & f_{\gamma|P}\left(x, \mu_F^2\right) - \frac{\alpha Q_q^2}{2\pi} \sum_{a=q,\bar{q}} \int_x^1 \frac{\mathrm{d}z}{z} f_{a|P}^{\mathrm{F.S.}}\left(\frac{x}{z}, \mu_F^2\right) \\ & \times \left\{ \ln\left(\frac{\mu_F^2}{m_q^2}\right) P_{\gamma f}(z) - P_{\gamma f}(z)\left(2\ln(1-z)+1\right) + C_{\gamma f}^{\mathrm{F.S.}}(z) \right\}. \end{aligned} \tag{1.73}$$

Therein x is the energy fraction carried by the parton coming from a proton, m_q and Q_q are the mass and the charge of the quarks, respectively. The splitting functions are defined as

$$P_{ff}(z) = \frac{1+z^2}{1-z}, \qquad P_{f\gamma}(z) = z^2 + (1-z)^2, \qquad P_{\gamma f} = \frac{1+(1-z)^2}{z}, \tag{1.74}$$

and $[\ldots]_+$ denotes the usual (+)-distribution prescription

$$\int_0^1 \mathrm{d}x\, [f(x)]_+ g(x) = \int_0^1 \mathrm{d}x\, f(x)[g(x) - g(1)], \tag{1.75}$$

with $g(x)$ representing a smooth test function. The coefficients $C_{ff}^{\text{F.S.}}$, $C_{f\gamma}^{\text{F.S.}}$ and $C_{\gamma f}^{\text{F.S.}}$ define the factorization scheme. In this work we consistently use the NNPDF2.3QED [85]. Actually the $\mathcal{O}(\alpha)$-corrected NLO PDF set NNPDF23 is only of LO with respect to QED corrections, i.e. they do not uniquely define a factorization scheme, but they should be most adequately used in a DIS-like factorization scheme for QED corrections (see Ref. [86] for arguments), so that

$$\begin{aligned} C_{ff}^{\text{DIS}} &= \left[P_{ff}(z) \left(\ln \frac{1-z}{z} - \frac{3}{4} \right) + \frac{9+5z}{4} \right]_+ , \\ C_{f\gamma}^{\text{DIS}} &= P_{f\gamma}(z) \ln \frac{1-z}{z} - 8z^2 + 8z - 1 , \\ C_{\gamma f}^{\text{DIS}} &= -C_{ff}^{\text{DIS}} . \end{aligned} \tag{1.76}$$

Chapter 2

Gauge-boson production in association with a photon at NLO

2.1 Process definitions at LO

The production of a leptonically decaying gauge boson in association with a photon includes four types of processes. For the W^+ production the corresponding partonic LO process is

$$u_i\,\bar{d}_j \to l^+\nu_l\,\gamma\,, \tag{2.1}$$

and for the charge conjugated process of W^- production we find

$$\bar{u}_i\,d_j \to l^-\bar{\nu}_l\,\gamma\,. \tag{2.2}$$

Therein u_i, $\bar{u}_i$, d_j and $\bar{d}_j$ indicate up-type quarks and antiquarks and down-type quarks and antiquarks of the first two generations ($i,j = 1,2$). The charged lepton as well as the corresponding neutrino/antineutrino are labeled as l and $\nu_l/\bar{\nu}_l$, where $l = \mathrm{e},\mu$. The LO Feynman diagrams for process (2.1) are shown in Fig. 2.1.

The production of a Z boson in association with a photon includes two types of processes.

$$q_i\,\bar{q}_i \to l^+l^-\,\gamma\,, \tag{2.3}$$

$$q_i\,\bar{q}_i \to \bar{\nu}_l\nu_l\,\gamma\,. \tag{2.4}$$

While in process (2.3) the final state contains two charged leptons as decay products of an intermediate Z boson or photon in process (2.4) the Z boson decays in two neutrinos. $q_i/\bar{q}_i$ indicate quarks and antiquarks of the five light quarks $q_i = u,d,s,c,b$. The corresponding LO Feynman diagrams are shown in Figs. 2.2 and 2.3. While for the process defined in Eq. (2.3) we assume $l = \mathrm{e},\mu$ for the process defined in Eq. (2.4) the final state includes three families of neutrinos $\nu_l = \nu_\mathrm{e},\nu_\mu,\nu_\tau$.

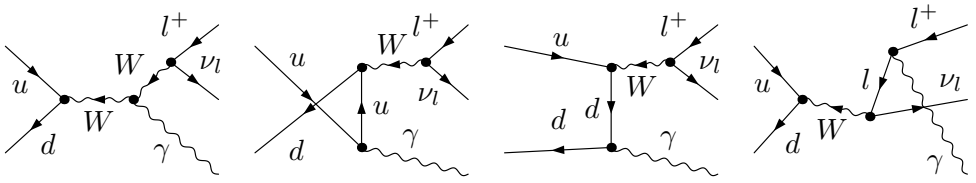

Figure 2.1: LO Feynman diagrams for the partonic process (2.1).

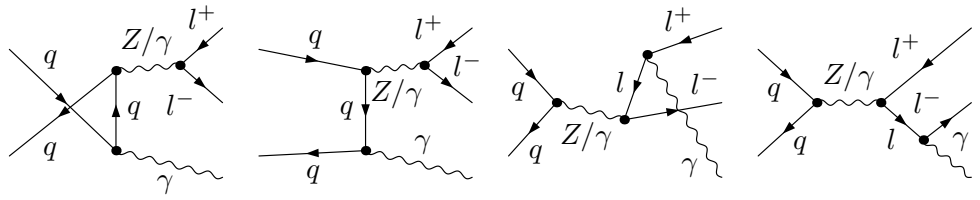

Figure 2.2: LO Feynman diagrams for the partonic process (2.3).

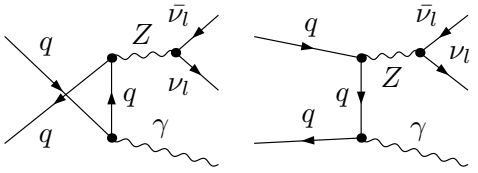

Figure 2.3: LO Feynman diagrams for the partonic process (2.4).

2.2 Virtual corrections

We compute the virtual QCD one-loop contributions to order $\mathcal{O}(\alpha^3\alpha_S)$ and the virtual EW one-loop diagrams to order $\mathcal{O}(\alpha^4)$. Technical details about the calculation of the emerging one-loop integrals will be discussed in App. B. The QCD corrections to the partonic processes defined in (2.1)–(2.4) include contributions from self-energy, vertex and box (4-point) diagrams only. For Wγ production as well as for the neutrino process (2.4) there are 10 QCD one-loop diagrams. The Zγ production process with two charged leptons in the final state includes 26 QCD one-loop diagrams. The virtual EW one-loop diagrams additionally involve pentagon diagrams. The structural diagrams for self-energies, vertices and boxes of the EW NLO corrections for processes (2.1) and (2.3) are given in Figs. 2.4–2.6 and Figs. 2.8–2.10, respectively the pentagons are shown explicitly in Figs. 2.7 and 2.11.

For the Wγ production processes there are about 280 virtual EW one-loop diagrams. The Zγ production where the final state contains two charged lepton comprises roughly twice as much diagrams because for almost all internal Z bosons the identical diagram with an internal photon exists. Due to the uncharged final state of process (2.4) the number of virtual diagrams is much lower than for process (2.3). The number of virtual one-loop diagrams for all processes are summarized in Table 2.1.

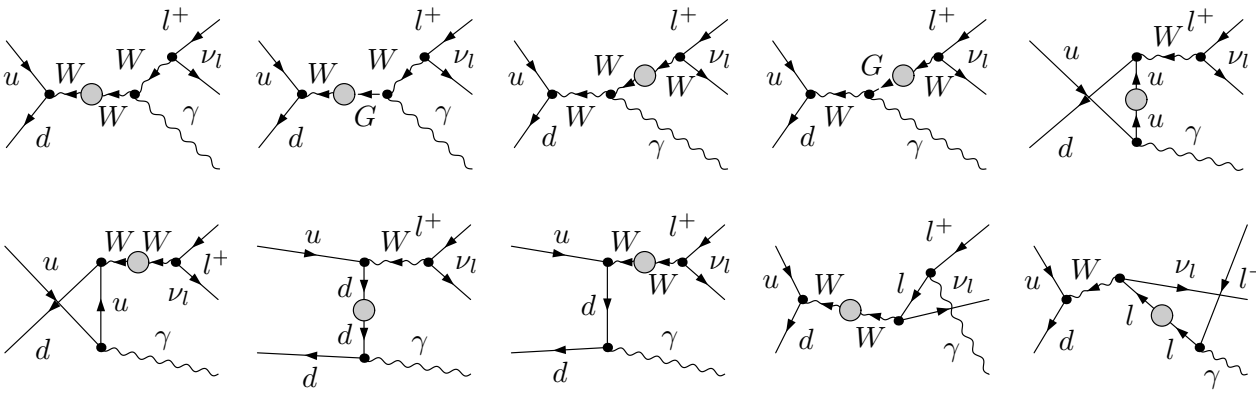

Figure 2.4: Self-energy corrections to the partonic process (2.1).

Process	Self-energy	Vertex	Box	Pentagon	Total
Wγ QCD	2	6	2		10
Wγ EW	124	90	50	16	280
Z$\gamma(l^+l^-)$ QCD	4	20	4		28
Z$\gamma(l^+l^-)$ EW	220	216	81	19	536
Z$\gamma(\bar{\nu}\nu)$ QCD	2	8	2		12
Z$\gamma(\bar{\nu}\nu)$ EW	60	94	37	6	197

Table 2.1: Number of virtual one-loop Feynman diagrams for the partonic processes defined in (2.1)–(2.4). We show the total number of virtual diagrams as well as the number of self-energy, vertex, box and pentagon diagrams separately. Therein triangles with an effective $g\mathrm{Z}\gamma$ and $g\gamma\gamma$ (which only appears for Z$\gamma(l^+l^-)$) vertex are included in the QCD vertex corrections of Zγ production. Wγ indicates the $\mathrm{W}^+\gamma$ production or the charged conjugated $\mathrm{W}^-\gamma$ production separatly.

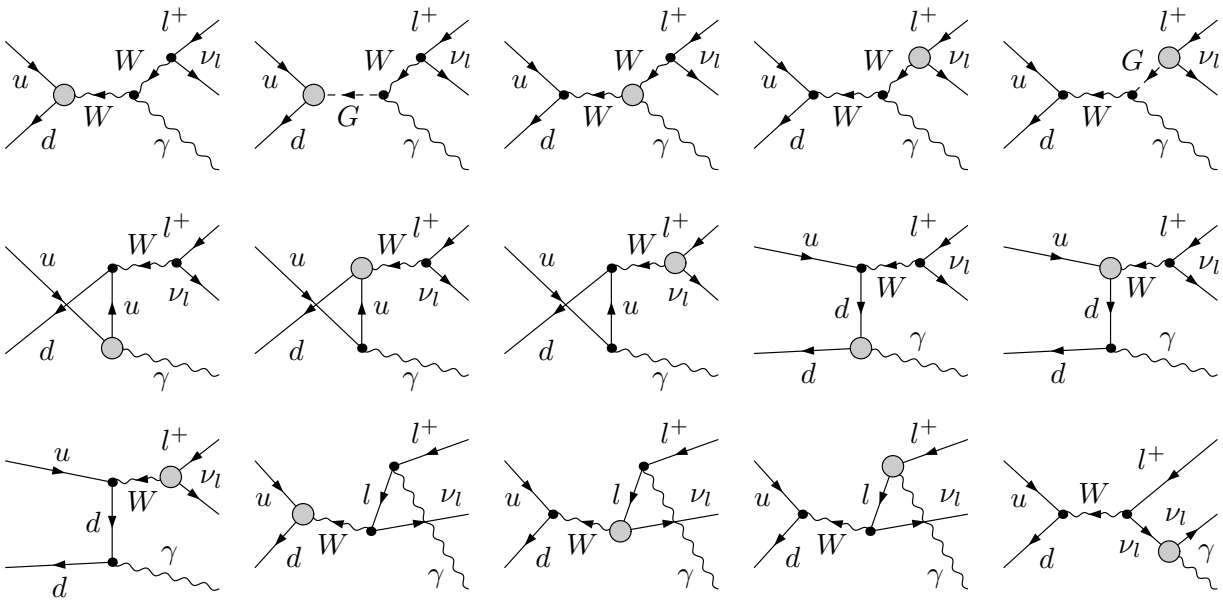

Figure 2.5: Vertex corrections to the partonic process (2.1).

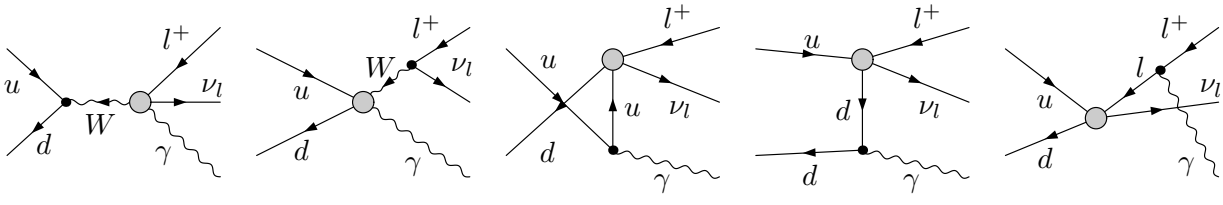

Figure 2.6: Box corrections to the partonic process (2.1).

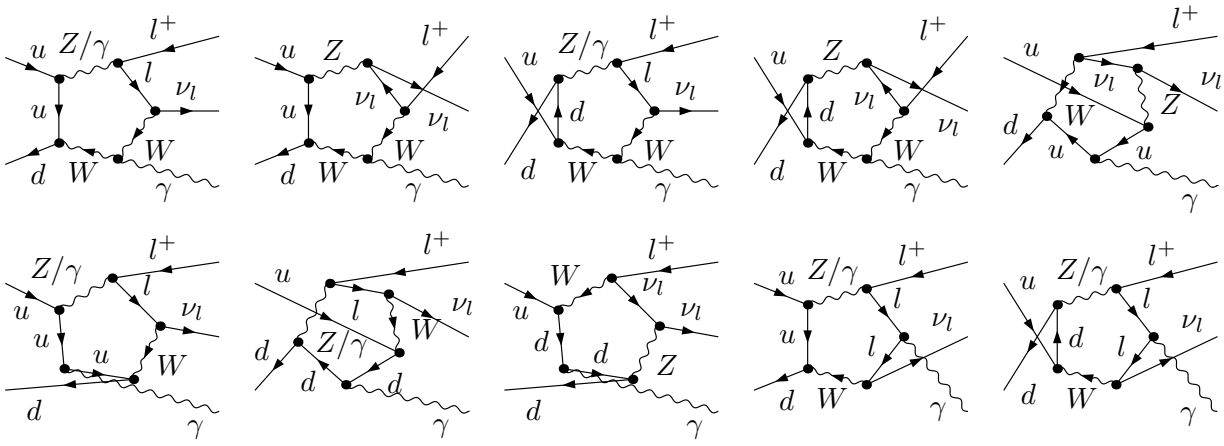

Figure 2.7: Explicit pentagon diagrams for the partonic process (2.1).

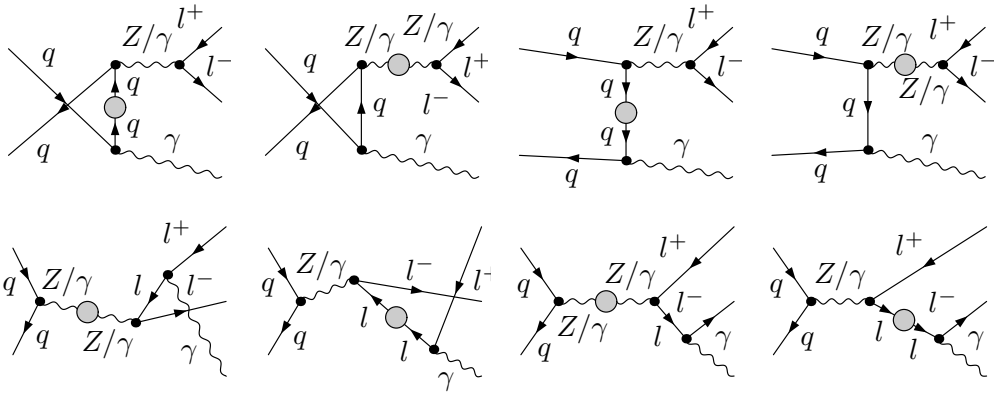

Figure 2.8: Self-energy corrections to the partonic process $q\,\bar{q} \to l^+ l^-\,\gamma$.

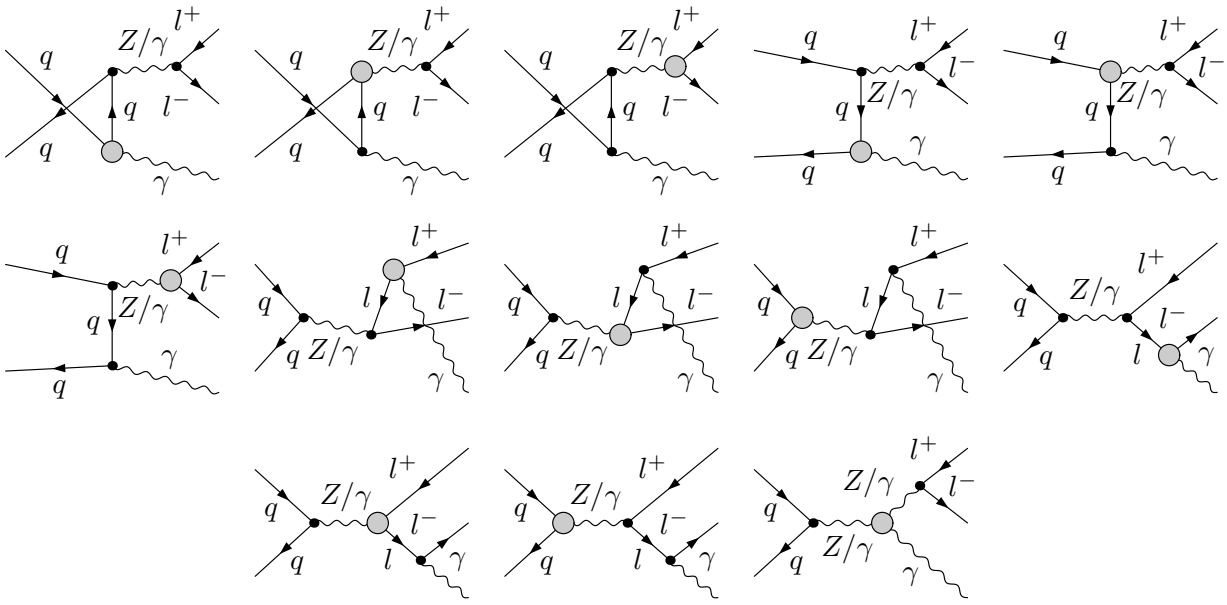

Figure 2.9: Vertex corrections to the partonic process $q\,\bar{q} \to l^+ l^-\,\gamma$.

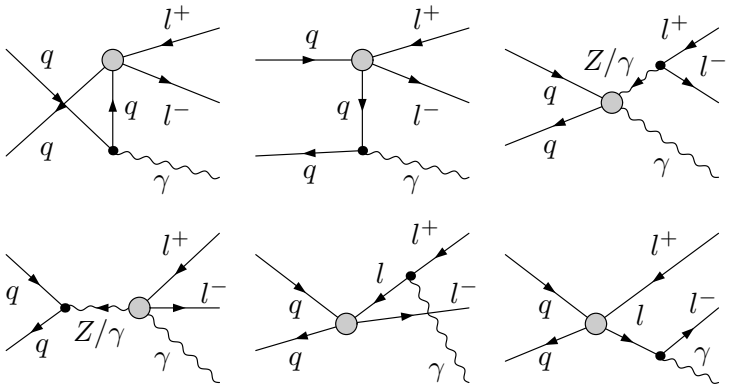

Figure 2.10: Box corrections to the partonic process $q\,\bar{q} \to l^+l^-\,\gamma$.

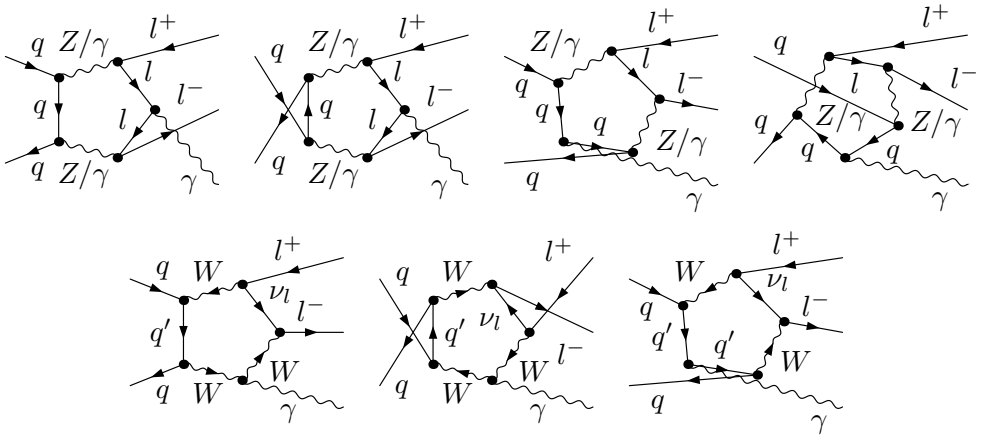

Figure 2.11: Explicit pentagon diagrams for the partonic process $q\,\bar{q} \to l^+l^-\,\gamma$.

2.3 Photon–photon-induced contribution

The partonic process defined in (2.3) implies the final state $l^+l^-\,\gamma$ which also can be produced by

$$\gamma\,\gamma \to l^+l^-\,\gamma\,, \tag{2.5}$$

which is a pure QED-process and does not include any intermediate vector boson. The Feynman diagrams for this process are shown in Fig. 2.12. Due to the two photons in the IS the partonic cross section will be convoluted two times with the small photon-PDFs and these contributions are expected to be small. For this reason we will give results for its contribution separately and do not consider NLO EW corrections to this LO process. Since this process only contains charged leptons as intermediate particle there are no QCD corrections.

2.4 Real corrections

In general, real corrections are induced by the radiation of an additional photon or QCD parton. For Wγ and Zγ production they can be divided in three sub-contributions: quark–antiquark-induced EW, photon-induced and QCD corrections.

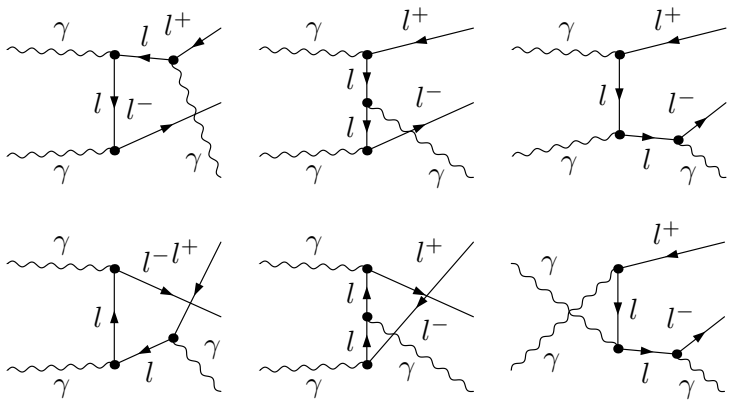

Figure 2.12: $\gamma\gamma$-induced LO diagrams for the process (2.5).

2.4.1 Real quark–antiquark-induced EW corrections

The quark–antiquark-induced EW corrections are given by the following partonic processes

$$u_i\,\bar{d}_j \to l^+\nu_l\,\gamma\,\gamma\,, \tag{2.6}$$

$$q_i\,\bar{q}_i \to l^+l^-\,\gamma\,\gamma\,, \tag{2.7}$$

$$q_i\,\bar{q}_i \to \bar{\nu}_l\nu_l\,\gamma\,\gamma\,. \tag{2.8}$$

The corresponding Feynman diagrams for the processes (2.6) and (2.7) are shown in Figs. 2.13 and 2.14. While the production of two charged leptons in 2.7 involves photon emission from IS and FS radiation the photons in the neutrino production process (2.8) result from IS radiation only (corresponding to the first six diagrams in Fig. 2.14).

Contributions from the partonic processes (2.6)–(2.8) contain singularities from soft photons and collinear fermion–photon configurations. The soft divergences completely cancel against corresponding contributions from virtual corrections. In contrast, the cancellation between collinear divergences of real and virtual corrections is only partial. As discussed in Section 1.3 remaining collinear singularities from photon radiation off IS partons are absorbed into the PDFs by a redefinition.

The cancellation of singularities due to photon radiation off FS leptons depends on the event reconstruction procedure. Hence, two cases should be considered. The first case describes a FS electron which can not be separated from collinear photons at the LHC because a collinear electron–photon system will be detected as only one shower in the electromagnetic calorimeter. In order to simulate this circumstance the electron and the photon will be recombined in the collinear phase-space region which results in a complete cancellation of the IR singularities (as specified by the KLN theorem [83, 84]). This case is called the collinear-safe (CS) case. The second scenario describes a FS muon. While the photon again will be absorbed in the electromagnetic calorimeter the muon leads to a signal in the muon chamber. Since muon and photon can be separated also if they are collinear they should not be recombined in the calculation. This scenario with a separation of "bare" muons and photons is called the non-collinear-safe case (NCS). Here, the KLN theorem can not be applied and the subtraction procedure has to be extended. As we will point out in detail in Sections 3.2.3 –3.2.5 this leads to additional logarithms of the lepton mass which remain in the cross section. The technical details about the formalism we use to treat the soft and collinear singularities are outlined in Section 3.2.

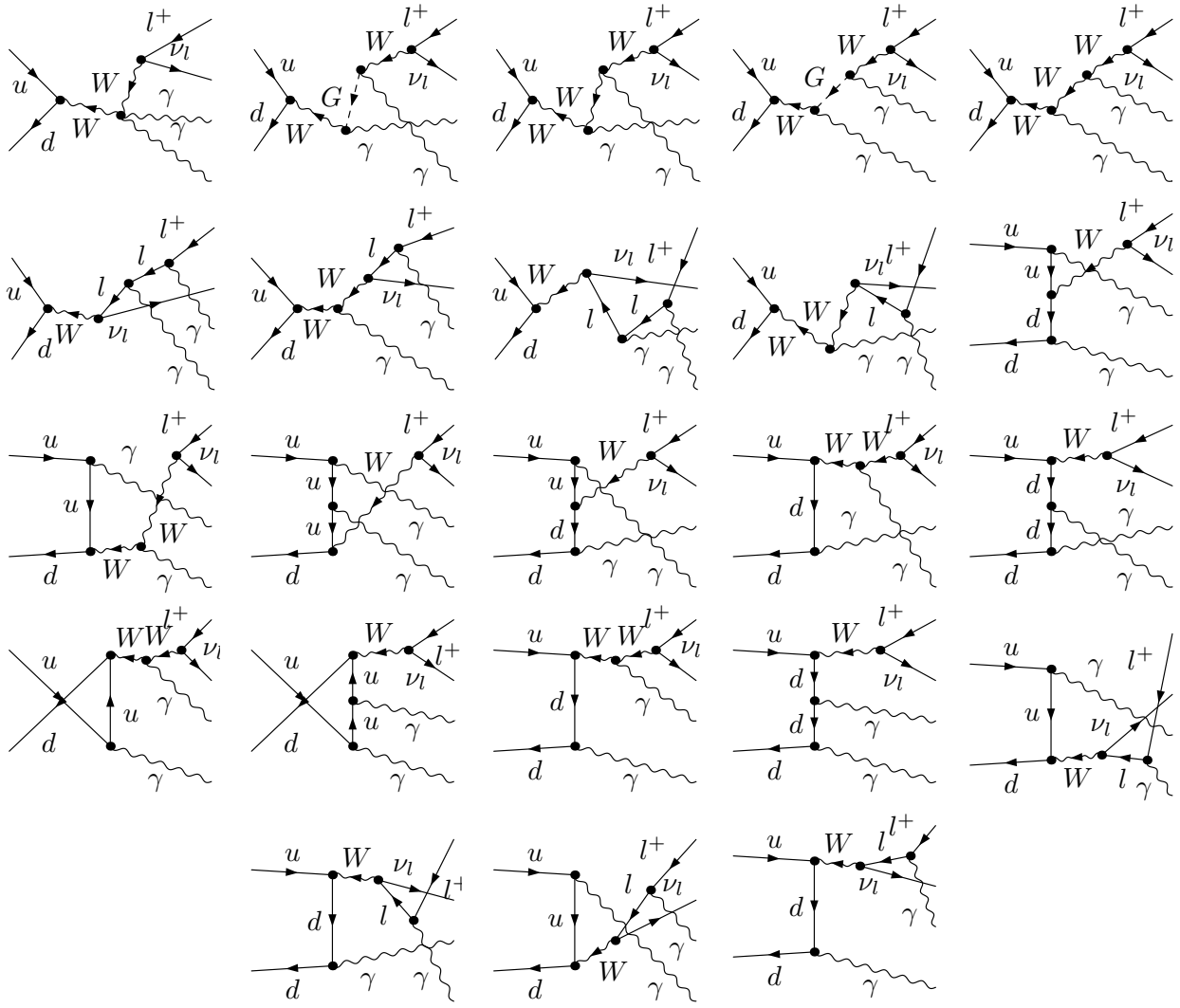

Figure 2.13: Feynman diagrams of the quark–antiquark-induced real EW corrections for the partonic process $u\,\bar{d} \to l^+\nu_l\,\gamma$.

2.4.2 Real QCD corrections

The real QCD corrections at NLO include quark–antiquark induced and gluon-induced contributions. The corresponding channels for $W^+\gamma$ production are given by

$$\begin{aligned} u_i\,\bar{d}_j &\to l^+\nu_l\,\gamma\,g\,, \\ u_i\,g &\to l^+\nu_l\,\gamma\,d_j\,, \\ \bar{d}_j\,g &\to l^+\nu_l\,\gamma\,\bar{u}_i \end{aligned} \tag{2.9}$$

and the Feynman diagrams for the quark–antiquark induced partonic process are shown in Fig. 2.15. The gluon-induced diagrams can be derived via crossing. The partonic processes for $Z\gamma$ production with two charged leptons in the final state are

$$\begin{aligned} q_i\,\bar{q}_i &\to l^+l^-\,\gamma\,g\,, \\ q_i\,g &\to l^+l^-\,\gamma\,q_i\,, \\ \bar{q}_i\,g &\to l^+l^-\,\gamma\,\bar{q}_i\,. \end{aligned} \tag{2.10}$$

With the Feynman diagrams for the partonic process $q\,\bar{q} \to\to l^+l^-\,\gamma$ shown in Fig. 2.16 gluon-induced diagrams are again related by crossing symmetries. The partonic channels for $Z\gamma$ with

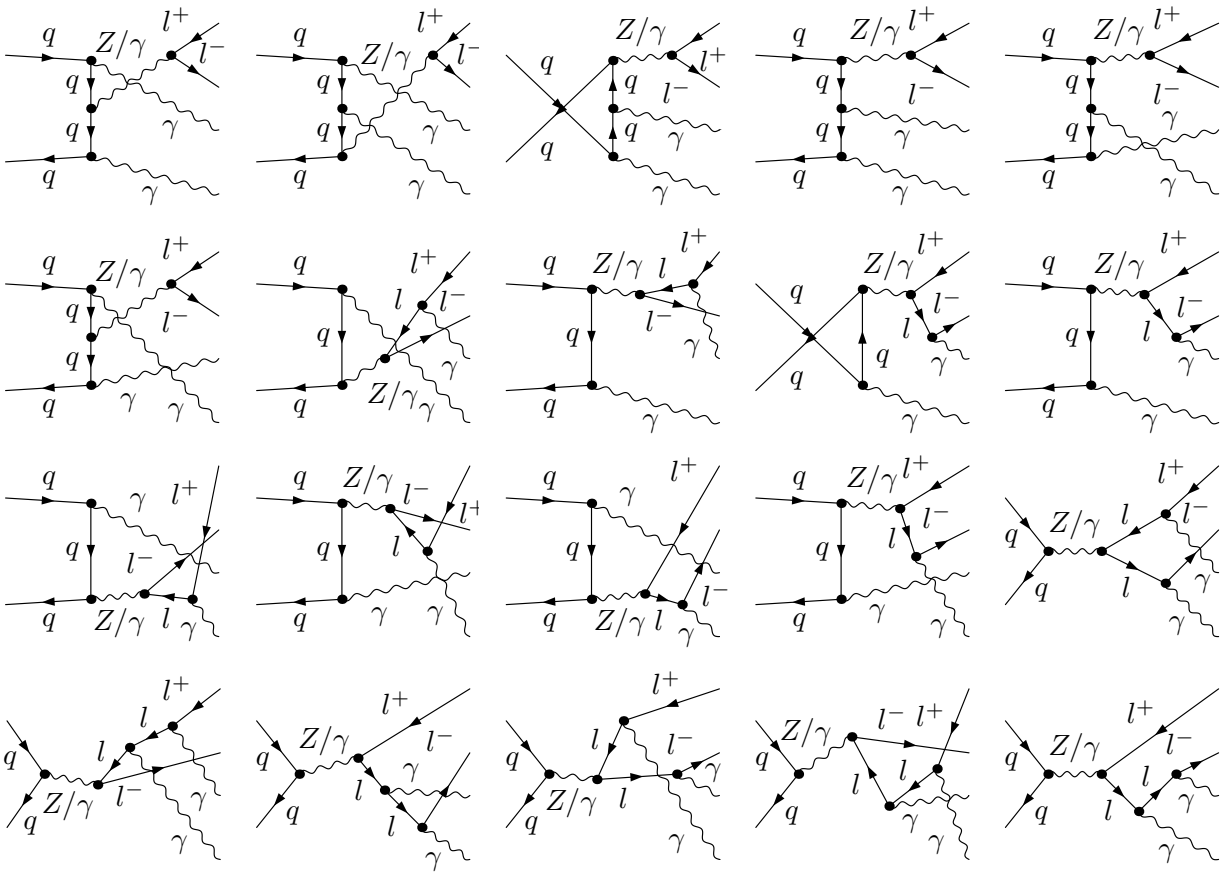

Figure 2.14: Feynman diagrams of the quark–antiquark-induced real EW corrections for the partonic process $q\,\bar{q} \to l^+ l^-\,\gamma$.

two neutrinos in the final state read

$$\begin{aligned} q_i\,\bar{q}_i &\to \bar{\nu}_l \nu_l\,\gamma\,g\,, \\ q_i\,g &\to \bar{\nu}_l \nu_l\,\gamma\,q_i\,, \\ \bar{q}_i\,g &\to \bar{\nu}_l \nu_l\,\gamma\,\bar{q}_i\,. \end{aligned} \tag{2.11}$$

The Feynman diagrams for the first partonic process in (2.11) results from the diagrams with intermediate Z bosons in Fig. 2.16 by replacing charged leptons with neutrinos. Since photons do not couple to neutrinos the corresponding diagrams in Fig. 2.16 do not exist for the neutrino process. Finally, Zγ production with two neutrinos contains half as much diagrams as the process with two charged leptons in final state. The diagrams for the gluon-induced can be derived via crossing symmetries.

For the treatment of IR singularities and its extraction from the real amplitudes the dipole-subtraction formalism à la Catani–Seymour [87, 88] is applied. All channels of the partonic processes given in Eqn. (2.9), (2.10) and (2.11) have the similarity that the final state contains a photon and a jet which potentially can become collinear. Experimentally there is no way to distinguish if a collinear photon is a result of the partonic process or generated during the hadronization process. Therefore a well-defined procedure for the handling of photons and jets is necessary. In this thesis we apply two methods for this aspect, namely, the method of democratic clustering in combination with a quark-to-photon fragmentation function and the Frixione isolation scheme. Both methods will be discussed in detail in Section 3.5.

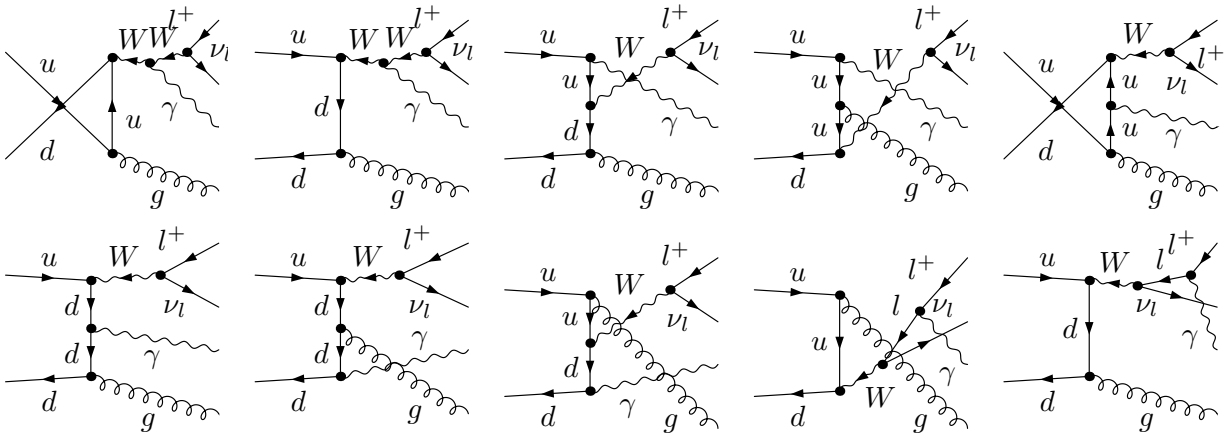

Figure 2.15: Feynman diagrams of the quark–antiquark-induced real QCD corrections for the partonic process $u\,\bar{d} \to l^+\nu_l\,\gamma$.

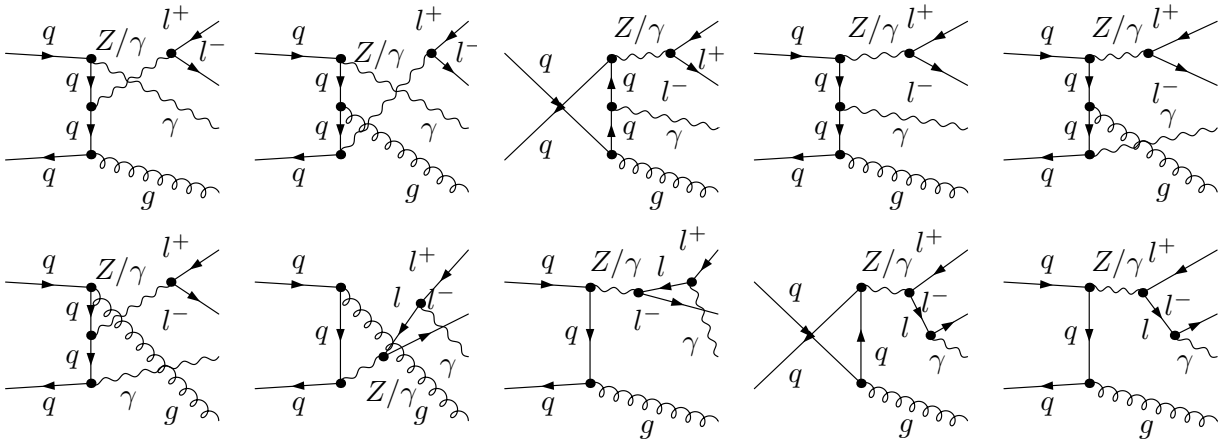

Figure 2.16: Feynman diagrams of the quark–antiquark-induced real QCD corrections for the partonic process $q\,\bar{q} \to l^+l^-\,\gamma$.

2.4.3 Real photon-induced EW corrections

The real photon-induced EW corrections include the following partonic channels for $\mathrm{W}^+\gamma$ production

$$\begin{aligned} u_i\,\gamma &\to l^+\nu_l\,\gamma\,d_j\,, \\ \bar{d}_j\,\gamma &\to l^+\nu_l\,\gamma\,\bar{u}_i\,. \end{aligned} \tag{2.12}$$

For $\mathrm{Z}\gamma$ production contributions from

$$\begin{aligned} q_i\,\gamma &\to l^+l^-\,\gamma\,q_i\,, \\ \bar{q}_i\,\gamma &\to l^+l^-\,\gamma\,\bar{q}_i\,. \end{aligned} \tag{2.13}$$

respectively

$$\begin{aligned} q_i\,\gamma &\to \bar{\nu}_l\nu_l\,\gamma\,q_i\,, \\ \bar{q}_i\,\gamma &\to \bar{\nu}_l\nu_l\,\gamma\,\bar{q}_i\,. \end{aligned} \tag{2.14}$$

have to be taken into account. All these channels can be derived from the quark–antiquark induced EW corrections by crossing one of the photons to the initial state and the quark or

antiquark to the final state. Since the FS signature for photon-induced corrections is the same as for the partonic processes of the real QCD corrections the identical treatment of collinear photon–jet configurations (mentioned in Section 2.4.2 and discussed in detail in Section 3.5) will be applied. The real matrix elements of the processes (2.12) and (2.14) include singularities from the splittings discussed in Section 3.2 and collinear splittings $\gamma \to f\bar{f}^*$ discussed in Sections 3.3. For process (2.13) we additionally have to consider the $f \to f\gamma^*$ splitting which leads to a photon entering the LO matrix element as IS particle. However, due to charge conservation a corresponding LO process with IS photons does not exist for Wγ production and due to the absence of a photon–neutrino coupling there is also no LO process with IS photons for $\mathrm{pp} \to \bar{\nu}\nu\gamma$. The $f \to f\gamma^*$ splitting is discussed in Section 3.4.

Chapter 3

Dipole subtraction in NLO calcuations

In this chapter we review the basic concept of the dipole subtraction formalism and summarize the most important formulae. Therefore, we briefly outline the basic concept of this formalism in Section 3.1. In Sections 3.2, 3.3 and 3.4 the different types of fermion–photon splittings and their explicit subtraction functions will be discussed. Section 3.5 is dedicated to the aspect of collinear photons and jets in the final state. Therein we present two different methods for the treatment of this issue.

3.1 General strategy

The calculation of real NLO corrections necessitates the computation of the phase-space integral $\int d\Phi_1 \left|\mathcal{M}_{\text{real}}\right|^2$. The real matrix element $\left|\mathcal{M}_{\text{real}}\right|^2$ in general contains soft and collinear singularities which complicate the numerical integration. This difficulty is approached by the dipole subtraction formalism. The basic idea is the introduction of a subtraction function $\left|\mathcal{M}_{\text{sub}}\right|^2$ with the same asymptotic behaviour in the soft and collinear regions of the phase space as the real matrix element. The generic procedure where the integral of the auxiliary function is subtracted and re-added back is given by

$$\int \mathrm{d}\Phi_1 \left|\mathcal{M}_{\text{real}}\right|^2 = \int \mathrm{d}\Phi_1 \left(\left|\mathcal{M}_{\text{real}}\right|^2 - \left|\mathcal{M}_{\text{sub}}\right|^2\right) + \int \mathrm{d}\Phi_1 \left|\mathcal{M}_{\text{sub}}\right|^2 \tag{3.1}$$

where Φ_1 indicates the $(N+1)$-particle phase space of the full real emission process. The subtraction term $\int \mathrm{d}\Phi_1 \left|\mathcal{M}_{\text{sub}}\right|^2$ has to fulfil two requirements:

1. It completely contains the singular behaviour of $\int \mathrm{d}\Phi_1 \left|\mathcal{M}_{\text{real}}\right|^2$ so that the first term on the r.h.s. of Eq. (3.1) is non-singular and can be integrated numerically easily.

2. It is possible to integrate out analytically the phase space of the radiated particle so that the phase-space integral can be factorized into a non-radiative part $\int \mathrm{d}\tilde{\Phi}_0$ and the part of the additional radiated particle $\int [\mathrm{d}\, k]$.

Therewith an analytical cancellation of singularities between the real and virtual corrections is possible.

If the subtraction function fulfils the upper conditions the phase-space integral in the second term on the r.h.s of Eq. (3.1) can be factorized in the following way

$$\int \mathrm{d}\Phi_1 = \int \mathrm{d}\tilde{\Phi}_0 \otimes \int [\mathrm{d}\, k]\,, \tag{3.2}$$

and so finally the integral of the real matrix elements transforms to

$$\int \mathrm{d}\Phi_1 \left|\mathcal{M}_{\text{real}}\right|^2 = \int \mathrm{d}\Phi_1 \Big(\left|\mathcal{M}_{\text{real}}\right|^2 - \left|\mathcal{M}_{\text{sub}}\right|^2 \Big) + \int \mathrm{d}\tilde{\Phi}_0 \otimes \Big(\int [\mathrm{d}\, k] |\mathcal{M}_{\text{sub}}|^2 \Big)\,, \tag{3.3}$$

where $\tilde{\Phi}_0$ denotes the (N)-particle phase space of the non-radiative process. In general, the subtraction function $|\mathcal{M}_{\text{sub}}|^2$ is constructed with a LO matrix element $|\mathcal{M}_0|^2$ and a process-independent auxiliary function $g_{ff'}^{(\text{sub})}$,

$$|\mathcal{M}_{\text{sub},ff'}|^2 \propto g_{ff'}^{(\text{sub})} \cdot |\mathcal{M}_0|^2 \,, \tag{3.4}$$

where the pair of indices ff' describes an arbitrary emitter–spectator combination. The emitter f is the charged particle which radiates the photon and the spectator is denoted by f'. In Eq. (3.3) the phase-space integrations $\int \mathrm{d}\Phi_1$ and $\int \mathrm{d}\tilde{\Phi}_0$ do not contain any singularities because the complete singular behaviour is included in $g_{ff'}^{(\text{sub})}$. After the analytic integration of $\int [\mathrm{d}\, k]$ the second term on the r.h.s of Eq. (3.3) can be combined with the virtual corrections. Thereby the corresponding virtual counterparts will compensate the singularities so that we end up with finite contributions only. Each of them can be easily integrated with numerical methods.

In the following section based on Ref. [89] we provide an overview about the subtraction procedure for photon radiation off fermions which is needed for the calculation of the quark–antiquark-induced real EW corrections defined in Eqs. (2.6)–(2.8). We will also summarize the extension concerning photon radiation off FS fermions to processes with non-collinear-safe observables worked out in detail in Ref. [90]. Since we will need additional subtraction functions for the calculation of the photon-induced EW corrections we provide an overview about the most important formulae for $\gamma \to ff^*$ splittings and $f \to f\gamma^*$ splittings in Sections 3.3 and 3.4. This overview follows Sections 3 and 5 of Ref. [90].

3.2 Photon radiation off fermions

The subtraction function $|\mathcal{M}_{\text{sub}}|^2$ can be constructed out of the squared Born-level matrix element $|\mathcal{M}_0|^2$ and the generic dipole function $g_{ff'}^{(\text{sub})}$,

$$|\mathcal{M}_{\text{sub}}(\Phi_1)|^2 = -\sum_{f \neq f'} Q_f \sigma_f Q_{f'} \sigma_{f'} e^2 g_{ff'}^{(\text{sub})}\left(p_f, p_{f'}, k\right) \left|\mathcal{M}_0\left(\tilde{\Phi}_{0,ff'}\right)\right|^2 \,, \tag{3.5}$$

where p_f, $p_{f'}$, and k are the emitter, the spectator, and the photon momenta, respectively. Q_f and $Q_{f'}$ describe the charges of emitter and spectator and the sign factors $\sigma_{f/f'}$ indicate the charge flows taking the values $+1(-1)$ for incoming (outgoing) fermions or outgoing (incoming) antifermions. Here, the projection of the $(N+1)$-particle phase space Φ_1 to the (N)-particle phase space is denoted as $\tilde{\Phi}_{0,ff'}$ where the additional indices ff' describe a specific combination of emitter f and spectator f'. For each combination ff' in general a different mapping is necessary. If we denote the momenta of Φ_1 by p_f, $p_{f'}$, k and $\{k_n\}$ (all remaining momenta) and the momenta of $\tilde{\Phi}_{0,ff'}$ by $\tilde{p}_f$, $\tilde{p}_{f'}$ and $\{\tilde{k}_n\}$ the transition between the two phase spaces obeys

$$\tilde{p}_f \underset{k\to 0}{\longrightarrow} p_f \,, \qquad \tilde{p}_{f'} \underset{k\to 0}{\longrightarrow} p_{f'} \,, \qquad \{\tilde{k}_n\} \underset{k\to 0}{\longrightarrow} \{k_n\} \tag{3.6}$$

in the soft limit and

$$\tilde{p}_i \underset{p_i k\to 0}{\longrightarrow} p_i + k \,, \qquad \tilde{p}_a \underset{p_a k\to 0}{\longrightarrow} x_a p_a \,, \qquad \tilde{p}_{f'} \underset{p_f k\to 0}{\longrightarrow} p_{f'} \,, \qquad \{\tilde{k}_n\} \underset{p_f k\to 0}{\longrightarrow} \{k_n\} \tag{3.7}$$

in the collinear limit. Therein x_a is the energy fraction of the IS fermion after photon emission

$$x_a = \frac{p_a^0 - k^0}{p_a^0} \,. \tag{3.8}$$

Here and in the following sections we follow the common convention to use indices a, b only for IS fermions and indices i, j only for FS fermions. As indicated in Eq. (3.7) IS emitter and

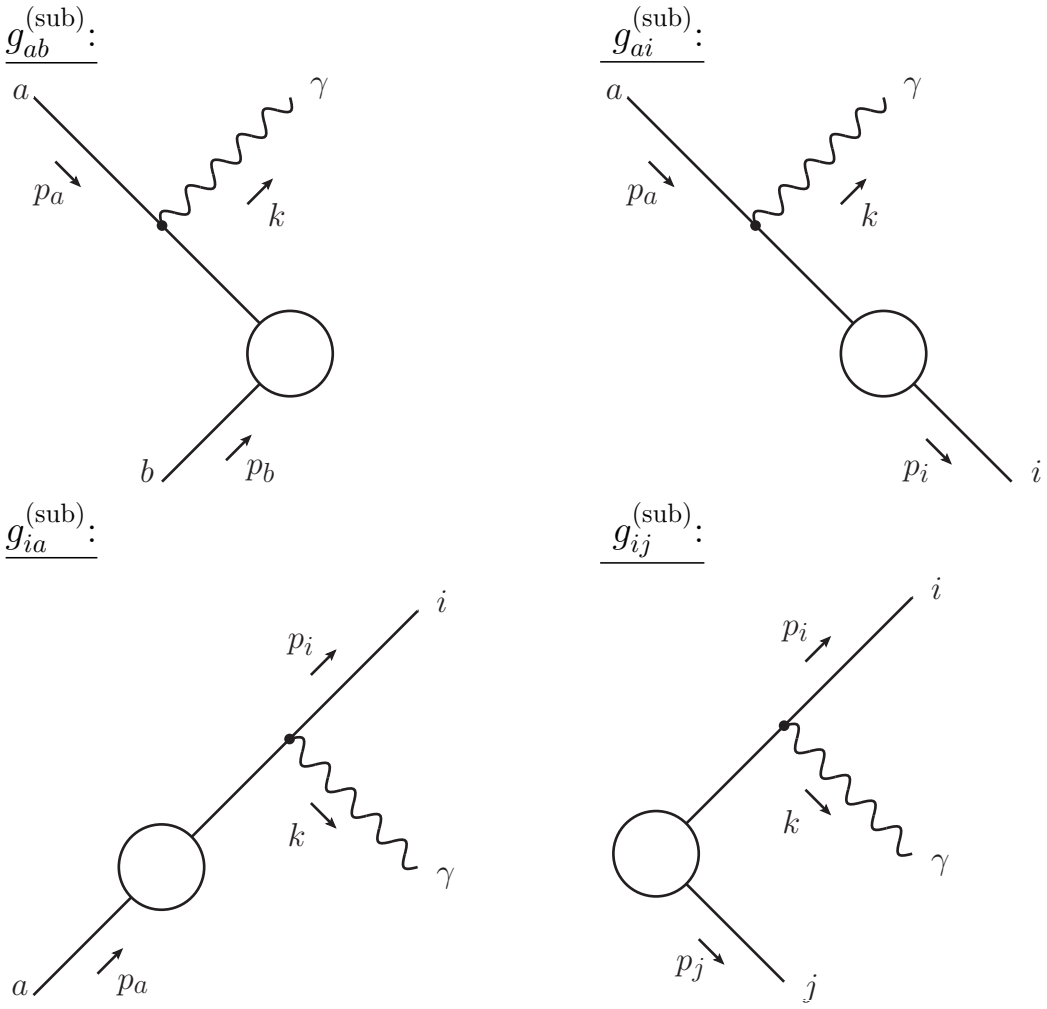

Figure 3.1: Effective diagrams for photon radiation off fermions.

FS emitter result in different phase-space transitions. The different cases of emitter–spectator combinations are also illustrated in Fig. 3.1. In this thesis we only take into account light fermions which means that we neglect their masses whenever it is possible. In the following sections we summarize the most important formulae for all emitter–spectator combinations.

3.2.1 Initial-state emitter and initial-state spectator

For an IS emitter a and an IS spectator b the schematic diagram is shown in the upper left part of Fig. 3.1. In this section we strictly follow the conventions and ideas in Ref. [89].

Introducing the abbreviations

$$x_{ab} = \frac{p_a p_b - p_a k - p_b k}{p_a p_b}\,, \qquad y_{ab} = \frac{p_a k}{p_a p_b}\,, \tag{3.9}$$

the dipole functions $g_{ab,\tau}^{(\mathrm{sub})}$ are defined as

$$\begin{aligned} g_{ab,+}^{(\mathrm{sub})} &= \frac{1}{(p_a k) x_{ab}} \left[\frac{2}{1-x_{ab}} - 1 - x_{ab}\right], \\ g_{ab,-}^{(\mathrm{sub})} &= 0\,. \end{aligned} \tag{3.10}$$

In the singular limits ($k \to 0$) and ($p_a k \to 0$) we find the following asymptotic behaviour

$$x_{ab} \underset{k\to 0}{\longrightarrow} 1\,, \qquad y_{ab} \underset{k\to 0}{\longrightarrow} 0\,, \qquad x_{ab} \underset{p_a k\to 0}{\longrightarrow} x_a\,, \qquad y_{ab} \underset{p_a k\to 0}{\longrightarrow} 0\,. \tag{3.11}$$

The corresponding integrated counterpart where the phase space of the additional radiated particle was integrated out analytically is given by

$$\begin{aligned}\int \mathrm{d}\Phi_1 \left|\mathcal{M}_{\mathrm{sub},ab}(\Phi_1)\right|^2 &= -\frac{\alpha}{2\pi} Q_a \sigma_a Q_b \sigma_b \\ &\times \Bigg\{ \int_0^1 \mathrm{d}x\, \mathcal{G}^{(\mathrm{sub})}_{ab,\tau}(s,x) \Bigg[\frac{1}{x} \int \mathrm{d}\tilde{\Phi}_{0,ab}(s,x) \left|\mathcal{M}_0\left(\tilde{p}_a(x), \tilde{p}_b, \{\tilde{k}_n(x)\}\right)\right|^2 \\ &\qquad - \int \mathrm{d}\tilde{\Phi}_{0,ab}(s,1) \left|\mathcal{M}_0\left(\tilde{p}_a(1), \tilde{p}_b, \{\tilde{k}_n(1)\}\right)\right|^2 \Bigg] \\ &\quad + G^{(\mathrm{sub})}_{ab,\tau}(s) \int \mathrm{d}\tilde{\Phi}_{0,ab}(s,1) \left|\mathcal{M}_0\left(\tilde{p}_a(1), \tilde{p}_b, \{\tilde{k}_n(1)\}\right)\right|^2 \Bigg\}, \end{aligned} \tag{3.12}$$

where we introduced the fine-structure constant $\alpha = e^2/(4\pi)$ and the momenta entering into the matrix element are related to the momenta in the upper left part Fig. 3.1 with $\tilde{p}_a(x) = x p_a$ and $\tilde{p}_b = p_b$. Therein we also indicate that the remaining momenta $\{\tilde{k}_n(x)\}$ of the phase space $\tilde{\Phi}_{0,ab}(s,x)$ implicitly depend on x. The distributions $\mathcal{G}^{(\mathrm{sub})}_{ab,\tau}(s,x)$ and the endpoint parts $G^{(\mathrm{sub})}_{ab,\tau}(s)$ read

$$\mathcal{G}^{(\mathrm{sub})}_{ab,+}(s,x) = P_{ff}(x) \left[\ln\left(\frac{s}{m_a^2}\right) - 1\right], \qquad \mathcal{G}^{(\mathrm{sub})}_{ab,-}(s,x) = 1 - x\,, \tag{3.13}$$

$$G^{(\mathrm{sub})}_{ab,+}(s) = \mathcal{L}(s, m_a^2) - \frac{\pi^2}{3} + \frac{3}{2}\,, \qquad G^{(\mathrm{sub})}_{ab,-}(s) = \frac{1}{2}\,, \tag{3.14}$$

with

$$\mathcal{L}(P^2, m^2) = \ln\left(\frac{m^2}{P^2}\right) \ln\left(\frac{m_\gamma^2}{P^2}\right) + \ln\left(\frac{m_\gamma^2}{P^2}\right) - \frac{1}{2}\ln^2\left(\frac{m^2}{P^2}\right) + \frac{1}{2}\ln\left(\frac{m^2}{P^2}\right) \tag{3.15}$$

and the Altarelli–Parisi splitting function $P_{ff}(z)$

$$P_{ff}\,(z) = \frac{1+z^2}{1-z}\,. \tag{3.16}$$

Since the mass singularities for vanishing photon and fermion masses are completely factorized into $\mathcal{G}^{(\mathrm{sub})}_{ab,+}$ and $G^{(\mathrm{sub})}_{ab,+}$ and the CM energy s is fixed the convolution with x and the phase-space integration in Eq. (3.12) can be done numerically.

3.2.2 Initial-state emitter and final-state spectator

As pointed out in Ref. [89] the cases IS emitter / FS spectator and FS emitter / IS spectator always appear in combination. Since, the treatment of IS emitters and FS emitters strongly differs in its complexity we first discuss the case of an IS emitter and a FS spectator in this section and the reverse case in the following section, separately. The corresponding effective diagram for an IS emitter a and a FS spectator i is shown on the upper right side of Fig. 3.1.

The dipoles are given by

$$\begin{aligned} g^{(\mathrm{sub})}_{ai,+}(p_a, p_i, k) &= \frac{1}{(p_a k) x_{ia}} \left[\frac{2}{2 - x_{ia} - z_{ia}} - 1 - x_{ia}\right], \\ g^{(\mathrm{sub})}_{ai,-}(p_a, p_i, k) &= 0\,, \end{aligned} \tag{3.17}$$

where we introduced the variables

$$x_{ia} = \frac{p_a p_i + p_a k - p_i k}{p_a p_i + p_a k}\,, \qquad z_{ia} = \frac{p_a p_i}{p_a p_i + p_a k} \tag{3.18}$$

with the asymptotic limits

$$x_{ia} \underset{k\to 0}{\longrightarrow} 1\,, \qquad z_{ia} \underset{k\to 0}{\longrightarrow} 1\,, \qquad x_{ia} \underset{p_a k\to 0}{\longrightarrow} x_a\,, \qquad z_{ia} \underset{p_a k\to 0}{\longrightarrow} 1\,. \tag{3.19}$$

Therein z_i is the energy fractions of the FS fermion after the emission of the photon

$$z_i = \frac{p_i^0}{p_i^0 + k^0} \tag{3.20}$$

and x_a is defined in Eq. (3.8). The numerical evaluable integrated counterpart reads

$$\begin{aligned}
\int \mathrm{d}\Phi_1 \left|\mathcal{M}_{\mathrm{sub},ai}(\Phi_1)\right|^2 &= -\frac{\alpha}{2\pi} Q_a \sigma_a Q_i \sigma_i \\
&\times \Bigg\{ \int_0^1 \mathrm{d}x \Bigg[\int \mathrm{d}\tilde{\Phi}_{0,ia}(P_{ia}^2, x) \frac{1}{x} \mathcal{G}_{ai,\tau}^{(\mathrm{sub})}(P_{ia}^2, x) \left|\mathcal{M}_0\left(\tilde{p}_a(x), \tilde{p}_i(x), \{\tilde{k}_n(x)\}\right)\right|^2 \\
&\qquad - \int \mathrm{d}\tilde{\Phi}_{0,ia}(P_{ia}^2, 1) \mathcal{G}_{ai,\tau}^{(\mathrm{sub})}(P_{ia}^2, x) \left|\mathcal{M}_0\left(\tilde{p}_a(1), \tilde{p}_i(1), \{\tilde{k}_n(1)\}\right)\right|^2 \Bigg] \\
&\quad + \int \mathrm{d}\tilde{\Phi}_{0,ab}(P_{ia}^2, 1) G_{ab,\tau}^{(\mathrm{sub})}(P_{ia}^2) \left|\mathcal{M}_0\left(\tilde{p}_a(1), \tilde{p}_i(1), \{\tilde{k}_n(1)\}\right)\right|^2 \Bigg\}\,,
\end{aligned} \tag{3.21}$$

where we use

$$\tilde{p}_a(x) = x p_a\,, \qquad \tilde{p}_i(x) = x p_a - P_{ia} \qquad \text{and} \qquad P_{ia} = p_i + k - p_a = \tilde{p}_i - \tilde{p}_a\,, \tag{3.22}$$

to connect the momenta $\tilde{p}_i$ and $\tilde{p}_a$ of the phase space $\tilde{\Phi}_{0,ia}(P_{ia}^2, x)$ with the momenta p_i, p_a and k in the upper right part of Fig. 3.1. With $P_{ff}(x)$ from Eq. (3.16) the explicit distributions read

$$\begin{aligned}
\mathcal{G}_{ai,+}^{(\mathrm{sub})}(P_{ia}^2, x) &= P_{ff}(x) \left[\ln\left(\frac{|P_{ia}^2|}{m_a^2 x}\right) - 1\right] - \frac{2}{1-x}\ln(2-x) + (1+x)\ln(1-x)\,, \\
\mathcal{G}_{ai,-}^{(\mathrm{sub})}(P_{ia}^2, x) &= 1 - x
\end{aligned} \tag{3.23}$$

and the endpoint parts are

$$\begin{aligned}
G_{ai,+}^{(\mathrm{sub})}(P_{ia}^2) &= \mathcal{L}(\left|P_{ia}^2\right|, m_a^2) - \frac{\pi^2}{6} + \frac{3}{2}\,, \\
G_{ai,-}^{(\mathrm{sub})}(P_{ia}^2) &= \frac{1}{2}\,,
\end{aligned} \tag{3.24}$$

where $\mathcal{L}$ defined in Eq. (3.15). The fermion mass singularities appear in the distribution $\mathcal{G}_{ai,+}^{(\mathrm{sub})}(P_{ia}^2, x)$ as well as in the endpoint part $G_{ai,+}^{(\mathrm{sub})}(P_{ia}^2)$.

3.2.3 Non-collinear-safe photon radiation of final-state fermions

In order to simulate the experimental setup at the LHC as close as possible we have to consider two different scenarios for the approach of photon emission off FS fermions. These two scenarios are called the CS and NCS case and their experimental motivation was given in Section 2.4.1. In this and the following two sections we follow Ref. [90] and focus on the NCS case because it is the more general one and it effectively also covers the CS case.

Since in the NCS case the FS fermion and the photon will not be recombined it is suitable to define the energy fraction z_f of the fermion f produced together with a photon in a fixed collinear cone as

$$z_f = \frac{p_f^0}{p_f^0 + k_\gamma^0}\,, \tag{3.25}$$

where p_f^0 and k_γ^0 are the energies of the fermion and photon, respectively. Starting from Eq. (3.3) the information on z_f and its analogous variables $z_{ff'}$ in the individual dipole contributions should be kept explicitly during the whole subtraction procedure. Technically this means, that the FS momenta that enter the LO matrix element of the dipole contributions and are used for the event-selection have to be transformed to an $(N+1)$-particle phase space with the following relations

$$p_f = z_{ff'}\tilde{p}_f^{(ff')}\,, \qquad k = (1-z_{ff'})\tilde{p}_f^{(ff')}\,, \qquad p_{f'} = \tilde{p}_{f'}^{(ff')}\,, \qquad \{k_n\} = \{\tilde{k}_n\}\,, \tag{3.26}$$

where the momentum $\tilde{p}_f^{(ff')}$ of the emitter fermion is split into the momenta p_f and k of the collinear fermion and photon. $z_{ff'}$ indicates the splitting for each individual dipole contribution with emitter f and spectator f' which pass into z_f in the collinear limit.

Afterwards the first term in Eq. (3.3) can be written as

$$\begin{aligned}\int \mathrm{d}\Phi_1 \Bigg[& |\mathcal{M}_{\mathrm{real}}|^2 \Theta_{\mathrm{cut}}(p_f, k, p_{f'}, \{k_n\}) \\ & - \sum_{f\neq f'} |\mathcal{M}_{\mathrm{sub},ff'}|^2 \Theta_{\mathrm{cut}}\left(z_{ff'}\tilde{p}_f^{(ff')}, (1-z_{ff'})\tilde{p}_f^{(ff')}, \tilde{p}_{f'}^{(ff')}, \{\tilde{k}_n\}\right)\Bigg]\,,\end{aligned} \tag{3.27}$$

where the application of the event-selection cuts is formalized by introducing the step function $\Theta_{\mathrm{cut}}\left(p_f, k, p_{f'}, \{\tilde{k}_n\}\right)$ acting on the momenta given in Eq. (3.26). The sum runs over all possible emitter–spectator pairs with $f \neq f'$. The remaining additional particles in the final state are indicated by $\{\tilde{k}_n\}$. The subtraction function $|\mathcal{M}_{\mathrm{sub},ff'}|^2$ was introduced in Eq. (3.4).

During the analytic integration of the re-added counterpart the dependence on z_f also has to be kept explicit. Since these steps as well as the final result for the integrated dipole contribution strongly differs between the IS spectator and the FS spectator case we discuss the technical details and the final formulae in the following two sections, separately. From Eq. (3.27) it follows directly that the subtraction functions $|\mathcal{M}_{\mathrm{sub},ia}|^2$ for the CS and NCS case are identical so that we can strictly follow Ref. [89]. There is only one difference between both cases namely the momenta on which the event-selection cuts will be applied. The CS scenario is already included in the NCS case assuming $z_{ff'} = 1$ so that Eq. (3.26) simplifies to

$$p_f \to \tilde{p}_f^{(ff')}\,, \qquad k \to 0\,, \qquad p_{f'} \to \tilde{p}_{f'}^{(ff')}\,. \tag{3.28}$$

For the re-added counterparts we will find additional mass-singular terms $\alpha \ln m_f$ in the NCS case which result from an incomplete cancellation of singularities during the subtraction procedure.

3.2.4 Final-state emitter and initial-state spectator

For a FS emitter i and an IS spectator a the schematic diagram is shown in the lower left part of Fig. 3.1. Using the abbreviations in Eq. (3.18), the asymptotic behaviour for the soft limits introduced in Eq. (3.19) as well as the collinear limits

$$x_{ia} \underset{p_i k\to 0}{\longrightarrow} 1\,, \qquad z_{ia} \underset{p_i k\to 0}{\longrightarrow} z_i \tag{3.29}$$

the dipoles functions are given by

$$g_{ia,+}^{(\mathrm{sub})}(p_i,p_a,k) = \frac{1}{(p_ik)x_{ia}}\left[\frac{2}{2-x_{ia}-z_{ia}} - 1 - z_{ia}\right],$$
$$g_{ia,-}^{(\mathrm{sub})}(p_i,p_a,k) = 0\,. \tag{3.30}$$

The corresponding counterpart after analytic integration reads

$$\begin{aligned}\int \mathrm{d}\Phi_1 |\mathcal{M}_{\mathrm{sub},ia}(\Phi_1)|^2 \;=\; & -\frac{\alpha}{2\pi}Q_i\sigma_i Q_a\sigma_a \int_0^1 \mathrm{d}x \int \mathrm{d}\tilde{\Phi}_{0,ia}(P_{ia}^2,x) \int_0^1 \mathrm{d}z \\ & \times \Theta_{\mathrm{cut}}\left(p_i = z\tilde{p}_i(x), k = (1-z)\tilde{p}_i(x), \{\tilde{k}_n(x)\}\right) \\ & \times \frac{1}{x}\Big\{ G_{ia}^{(\mathrm{sub})}(P_{ia}^2)\,\delta(1-x)\,\delta(1-z) + \Big[\mathcal{G}_{ia}^{(\mathrm{sub})}(P_{ia}^2,x)\Big]_+ \delta(1-z) \\ & \quad + \Big[\bar{\mathcal{G}}_{ia}^{(\mathrm{sub})}(P_{ia}^2,z)\Big]_+ \delta(1-x) + \Big[\bar{g}_{ia}^{(\mathrm{sub})}(x,z)\Big]_+^{(x,z)} \Big\} \Big|\mathcal{M}_0(\tilde{p}_i(x),\tilde{p}_a(x),\{\tilde{k}_n(x)\})\Big|^2, \end{aligned} \tag{3.31}$$

where $\tilde{p}_i$, $\tilde{p}_a$ and P_{ia}^2 are introduced in Eq. (3.22) which connects the momenta of the phase space $\tilde{\Phi}_{0,ia}(P_{ia}^2,x)$ with the momenta p_i, p_a and k in the lower left part of Fig. 3.1. Eq. (3.31) also includes the CS scenario where the Θ-function has a much simpler structure. After performing the z-integration only the z-independent terms in line 3 will contribute and the terms in line 4 will vanish. $[\ldots]_+$ indicate the usual (+)-distribution defined in Eq. (1.75) The subtraction procedure is constructed in such a way that for the NCS case in comparison to the CS scenario we find additional terms (see line 4 of Eq. (3.31)) which can be simply added. These terms include a (+)-distribution acting on z and a double (+)-distribution defined as

$$\int_0^1 \mathrm{d}x \int_0^1 \mathrm{d}y \Big[f(x,y)\Big]_+^{(x,y)} g(x,y) = \int_0^1 \mathrm{d}x\, f(x,y)[g(x,y) - g(1,y) - g(x,1) + g(1,1)]\,, \tag{3.32}$$

where $g(x)$ and $g(x,y)$ denote smooth test functions. The endpoint part $G_{ia}^{(\mathrm{sub})}(P_{ia}^2)$ and the distribution $\mathcal{G}_{ia}^{(\mathrm{sub})}(P_{ia}^2,x)$ appearing in line 3 of Eq. (3.31) are given by

$$\begin{aligned} G_{ia}^{(\mathrm{sub})}(P_{ia}^2) &= \mathcal{L}(|P_{ia}^2|,m_i^2) - \frac{\pi^2}{2} + \frac{3}{2}\,, \\ \mathcal{G}_{ia}^{(\mathrm{sub})}(P_{ia}^2,x) &= \frac{1}{1-x}\left[2\ln\left(\frac{2-x}{1-x} - \frac{3}{2}\right)\right], \end{aligned} \tag{3.33}$$

where $\mathcal{L}(P^2,m^2)$ is defined in Eq. (3.15). The z-dependent functions from line 4 read

$$\begin{aligned} \bar{g}_{ia}^{(\mathrm{sub})}(x,z) &= \frac{1}{1-x}\left(\frac{2}{2-x-z} - 1 - z\right), \\ \bar{\mathcal{G}}_{ia}^{(\mathrm{sub})}(P_{ia}^2,z) &= P_{ff}(z)\left[\ln\left(\frac{-P_{ia}^2 z}{m_i^2}\right) - 1\right] - \frac{2\ln(2-z)}{1-z} + (1+z)\ln(1-z) + (1-z)\,, \end{aligned} \tag{3.34}$$

where the splitting function $P_{ff}(z)$ was already defined in Eq. (3.16). The remaining fermion-mass dependence originating from the incomplete cancellation of collinear singularities is included in the function $\bar{\mathcal{G}}_{ia}^{(\mathrm{sub})}(P_{ia}^2,z)$. For a meaningful theoretical prediction the value of this fermion mass has to be chosen as the physical value of the FS particle.

3.2.5 Final-state emitter and final-state spectator

The effective diagram for the case of a FS emitter i and a FS spectator j is shown in the lower right part of Fig. 3.1. Introducing the abbreviations

$$y_{ij} = \frac{p_ik}{p_ip_j + p_ik + p_jk}\,, \qquad z_{ij} = \frac{p_ip_j}{p_ip_j + p_jk}\,, \tag{3.35}$$

leads to the dipole functions

$$g_{ij,+}^{(\mathrm{sub})}(p_i,p_j,k) = \frac{1}{(p_ik)(1-y_{ij})}\left[\frac{2}{1-z_{ij}(1-y_{ij})} - 1 - z_{ij}\right],$$
$$g_{ij,-}^{(\mathrm{sub})}(p_i,p_j,k) = 0\,. \tag{3.36}$$

With z_i from Eq. (3.20) it can be easily checked that the soft and collinear limits are

$$y_{ij} \underset{k\to 0}{\longrightarrow} 0\,, \qquad z_{ij} \underset{k\to 0}{\longrightarrow} 1\,, \qquad y_{ij} \underset{p_ik\to 0}{\longrightarrow} 0\,, \qquad z_{ij} \underset{p_ik\to 0}{\longrightarrow} z_i\,. \tag{3.37}$$

Analytic integration over the phase space of the additional radiated particle ends up in the following expression for the re-added counterpart

$$\begin{aligned}\int \mathrm{d}\Phi_1 |\mathcal{M}_{\mathrm{sub},ij}(\Phi_1)|^2 \;=\; &-\frac{\alpha}{2\pi} Q_i\sigma_i Q_j\sigma_j \int \mathrm{d}\tilde{\Phi}_{0,ij} \int_0^1 \mathrm{d}z \\ &\times \left\{ G_{ij,\tau}^{(\mathrm{sub})}(P_{ij}^2)\delta(1-z) + \left[\bar{\mathcal{G}}_{ij,\tau}^{(\mathrm{sub})}(P_{ij}^2,z)\right]_+ \right\} \\ &\times \left|\mathcal{M}_0(\tilde{p}_i,\tilde{p}_j,\{\tilde{k}_n\})\right|^2 \Theta_{\mathrm{cut}}\left(p_i = z\tilde{p}_i, k = (1-z)\tilde{p}_i, p_j, \{\tilde{k}_n\}\right)\,, \end{aligned} \tag{3.38}$$

where the phase space $\tilde{\Phi}_{0,ij}$ is generated by the momenta $\tilde{p}_i$, $\tilde{p}_j$ and $\{\tilde{k}_n\}$. p_i, k, p_j and $\{k_n\}$ can be derived by the transformation relation given in Eq. (3.26). The invariant P_{ij}^2 is independent of z and can be calculated via $P_{ij}^2 = (\tilde{p}_i + \tilde{p}_j)^2$. The Θ-function again formalizes the application of the event-selection cuts based on the momenta of the $(N+1)$-particle phase space. The first term of Eq. (3.38) includes the z-independent distribution $G_{ij,\tau}^{(\mathrm{sub})}(P_{ij}^2)$ given by

$$G_{ij}^{(\mathrm{sub})}(P_{ij}^2) = \mathcal{L}(|P_{ia}^2|, m_i^2) - \frac{\pi^2}{3} + \frac{3}{2}\,, \tag{3.39}$$

where $\mathcal{L}$ was defined in Eq. (3.15). The additional z-dependent term which is only non-zero in the NCS scenario includes the function

$$\bar{\mathcal{G}}_{ij}^{(\mathrm{sub})}(P_{ij}^2,z) = P_{ff}(z)\left[\ln\left(\frac{P_{ij}^2 z}{m_i^2}\right) - 1\right] + (1+z)\ln(1-z) + (1-z)\,, \tag{3.40}$$

with the splitting function defined in Eq. (3.16).

3.3 Collinear singularities of $\gamma \to f\bar{f}^*$ splittings

The photon-induced contributions of Wγ and Zγ production defined in Eqn. (2.12)–(2.14) include collinear singularities from $\gamma \to f\bar{f}^*$ splittings. Following Section 3 of Ref. [90] we assume a generic process defined by

$$\gamma(k) + a(p_a) \to f(p_f) + X\,, \tag{3.41}$$

where a is the massles incoming particle and f is an outgoing light fermion. The momenta of the particles are illustrated in the left part of Fig. 3.2 and are also given in parenthesis. The asymptotic behaviour of the squared matrix element can be expressed by

$$\left|\mathcal{M}_{\gamma a\to fX}(k,p_a,p_f)\right|^2 \underset{p_fk\to 0}{\sim} Q_f^2 e^2 h^{\gamma f}(k,p_f)\left|\mathcal{M}_{\bar{f}a\to X}(p_{\bar{f}} = xk, p_a)\right|^2\,, \tag{3.42}$$

where $Q_f e$ indicates the electric charge of the fermion f and x is the energy fraction of the fermion $\bar{f}$ in relation to the energy of the incoming photon γ. The matrix element $\mathcal{M}_{\bar{f}a\to X}$

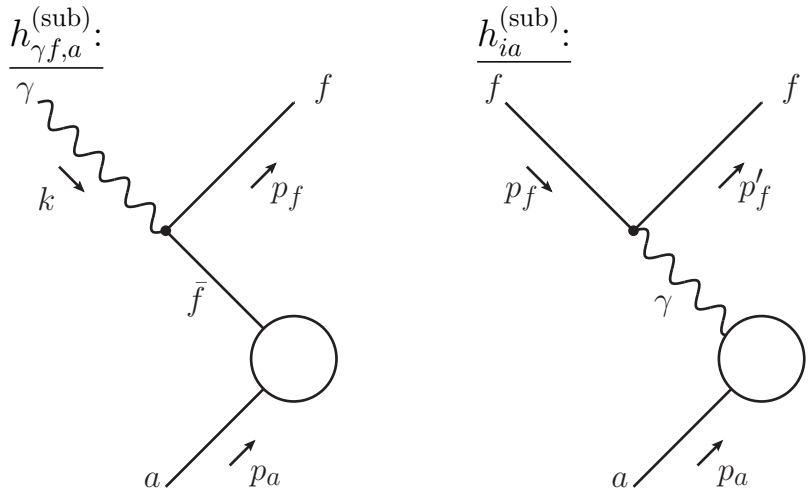

Figure 3.2: Effective diagrams for the collinear $\gamma \to f\bar{f}^*$ splitting (left) and the collinear $f \to f\gamma^*$ splitting (right) with IS spectator.

belongs to the LO processes which are defined for Wγ and Zγ production in Eqn. (2.1)–(2.4). The collinear divergence in the squared matrix element $|\mathcal{M}_{\gamma a\to fX}(k, p_a, p_f)|^2$ appears if the angle Θ_f between f and γ becomes small. The complete singular behaviour is included in one single dipole function $h^{\gamma f}(k, p_f)$ with one arbitrary chosen spectator. Since we have used the case with IS spectator a in our calculation we discuss the corresponding dipole functions in the following.

3.3.1 Initial-state spectator

The corresponding effective diagram for the case with an IS spectator is shown in the left part of Fig. 3.2. Using the splitting function $P_{f\gamma}(x)$ defined in Eq. (1.74) and the abbreviation

$$x_{f,\gamma a} = \frac{p_a k - p_f k - p_a p_f}{p_a k} \tag{3.43}$$

the dipole function $h^{\gamma f,a}$ is given by

$$h^{\gamma f,a} = \frac{1}{x_{f,\gamma a}(kp_f)} \left(P_{f\gamma}(x_{f,\gamma a}) + \frac{x_{f,\gamma a} m_f^2}{kp_f} \right) . \tag{3.44}$$

As worked out in detail in Ref. [90] the expression for the re-added counterpart after analytic integration then reads

$$\sigma^{(\mathrm{sub})}_{a\gamma\to fX}(k, p_a) = N_{c,f} \frac{Q_f^2 \alpha}{2\pi} \int_0^1 dx\, \mathcal{H}^{\gamma f,a}(s, x)\, \sigma_{\bar{f}a\to X}(p_{\bar{f}} = xk, p_a) \,, \tag{3.45}$$

where the function $\mathcal{H}^{\gamma f,a}(s, x)$ is defined as

$$\mathcal{H}^{\gamma f,a}(s, x) = P_{f\gamma}(x) \ln \left(\frac{s(1-x)^2}{m_f^2} \right) + 2x(1-x) \,. \tag{3.46}$$

3.4 Collinear singularities of $f \to f\gamma^*$ splittings

As mentioned in Section 2.3 the process $pp \to l^+l^-\gamma$ includes a LO contribution with two IS photons. Since this contribution exists the collinear splitting $f \to f\gamma^*$ (where the photon enters the LO process) has to be considered for the photon-induced real EW corrections.

Following Section 5 of Ref. [90] we suppose a generic process defined by

$$f(p_f) + a(p_a) \to f(p_{f'}) + X\,. \tag{3.47}$$

Therein a denotes a massless incoming particle and f represents the light fermion which radiates a photon. The corresponding momenta are given in parenthesis in Eq. (3.47) and are illustrated in the right part of Fig. 3.2. For our purposes we use the average over the azimuthal angle ϕ'_f of the $f \to f\gamma$ plane around the collinear axis so that the spin correlation drops out and the asymptotic behaviour of the squared matrix element is given by

$$\langle \left|\mathcal{M}_{\gamma a\to fX}(k, p_a, p_f)\right|^2 \rangle_{\phi'_f} \underset{p_f p'_f \to 0}{\sim} N_{c,f}\, Q_f^2 e^2 h^{ff}(p_f, p'_f) \left|\mathcal{M}_{\gamma a\to X}(\tilde{k}, p_a)\right|^2 . \tag{3.48}$$

Technical details about the spin correlation and the averaging process of ϕ'_f are discussed in Ref. [90]. At this point we use the same arguments as already outlined in Section 3.3. Since the collinear divergence $p_f p'_f \to 0$ can be treated with one specific choice for the spectator we choose the IS particle a and discuss the related formulae in the following Section.

3.4.1 Initial-state spectator

The case with an IS spectator is illustrated in the right part of Fig. 3.2. Since we define the the abbreviations

$$x_{f,fa} = \frac{p_a p_f - p_f p'_f - p_a p'_f}{p_a p_f}\,, \qquad y_{f,fa} = \frac{p_f p'_f}{p_a p_f}\,, \tag{3.49}$$

in analogy to Eq. (3.9) with the replacements $p_b \to p_f$, $k \to p'_f$ and use the splitting function $P_{\gamma f}(x)$ from Eq. (1.74) the dipole function h^{ff} in Eq. (3.48) reads

$$h^{ff,a} = \frac{1}{s\, x_{f,fa} y_{f,fa}} \left(P_{f\gamma}(x_{f,fa}) + \frac{2x_{f,fa}(1 - x_{f,fa}) m_f^2}{s\, y_{f,fa}(1 - x_{f,fa} - y_{f,fa})} \right) , \tag{3.50}$$

with the energy squared defined as $s = (p_f + p_a)^2$. The part of the re-added cross section is given by

$$\sigma^{(\mathrm{sub})}_{fa\to fX}(p_f, p_a) = \frac{Q_f^2 \alpha}{2\pi} \int_0^1 dx\, \mathcal{H}^{ff,a}(s, x)\, \sigma_{\gamma a\to X}(\tilde{k} = x p_f, p_a)\,, \tag{3.51}$$

where the distribution $\mathcal{H}^{ff,a}$ reads

$$\mathcal{H}^{ff,a}(s, x) = P_{\gamma f}(x) \ln\left(\frac{s(1-x)^2}{x^2 m_f^2} \right) - \frac{2 - 2x}{x}\,. \tag{3.52}$$

3.5 Collinear photon-jet configurations

The partonic processes for real QCD corrections and photon-induced corrections defined in Sections 2.4.2 and 2.4.3 include photons and quarks in the final state which can become potentially collinear. Such a situation where a photon is radiated collinear to a FS quark leads to additional divergences which only would cancel if photon and quarks are treated in the same

way. However, this would imply that the recombination of photons with QCD partons has to be included in the jet algorithm and only a combined cross section of W/Z + γ production and W/Z + jet production would give rise to IR-finite results. Technically, there are two methods describing a well-defined procedure for the separation of the two upper process classes:

1. a combination of democratic clustering and the use of the quark-to-photon fragmentation function as it was introduced in Refs. [55, 56];

2. the Frixione isolation scheme introduced in Ref. [57].

Both concepts will be used in our calculations and we will discuss the technical details of them in the following sections.

3.5.1 Quark-to-photon fragmentation function and democratic clustering of photons and jets

The concept of democratic clustering treats photons and jets on equal footing. If a photon and a jet become collinear they are clustered to one pseudo-particle. Technically the momenta of photon and jet are clustered if the rapidity–azimuthal-angle separation

$$R_{\gamma\text{jet}} = \sqrt{(y_\gamma + y_{\text{jet}})^2 + (\phi_\gamma - \phi_{\text{jet}})^2} \tag{3.53}$$

with the rapidity

$$y = \frac{1}{2} \ln \left[(E + p_{\text{L}}) \,/\, (E - p_{\text{L}}) \right] \tag{3.54}$$

is lower than a certain limit R_0. The parameter R_0 is called cone size. Using the energy fraction of the photon

$$z_\gamma = \frac{E_\gamma}{E_\gamma + E_{\text{jet}}} \,, \tag{3.55}$$

a collinear photon–jet system is defined as a photon if z_γ is larger than the cut value z_{cut}, otherwise the photon–jet system is defined as a jet. Since in this thesis we focus on Wγ and Zγ production the event will be discarded if a photon–jet system is defined as a jet. The complementary strategy was applied for W + jet production in Ref. [91] and for Z + jet production in Refs. [92, 93].

The asymptotic behaviour of singularity originating from the collinear photon–quark configuration is given by the following subtraction term

$$|\mathcal{M}_{\text{sub}}(\Phi_1)|^2 = Q_i^2 e^2 g_{il}^{(\text{sub})}(p_i, p_l, k) \left| \mathcal{M}_0^{\text{W/Z+jet}} \left(\tilde{p}_i, \tilde{p}_l, \{\tilde{k}_n\} \right) \right|^2 . \tag{3.56}$$

Therein we use the dipole subtraction function for the case of a FS emitter and a FS spectator from Eq. (3.36). As FS spectator we choose the charged lepton so that we have to do the replacements $y_{ij} \to y_{il}$ and $z_{ij} \to z_{il}$. In the collinear limit $(p_i k) \to 0$ these values behave as $y_{il} \to 0$, $z_{il} \to z_i$ and $z_{\gamma l} = 1 - z_{il} \to z_\gamma$, where z_i is the energy fraction of the quark in the quark–photon system in the collinear limit

$$z_i = \frac{E_i}{E_i + E_\gamma} = 1 - z_\gamma \,, \tag{3.57}$$

and z_γ is the corresponding energy fraction of the photon. In Eq. (3.56) the momenta $\tilde{p}_i$, $\tilde{p}_l$ and $\{\tilde{k}_n\}$ represent the projected phase space $\tilde{\Phi}_{0,il}$. Since we choose a FS spectator no boost has to be applied and the momenta $\{\tilde{k}_n\}$ equal the momenta $\{k_n\}$ of the $(N+1)$-particle phase space.

Process	gluon-induced	photon-induced
W^+jet	$u_i\, g \to l^+\nu_l\, d_j$ $\bar{d}_j\, g \to l^+\nu_l\, \bar{u}_i$	$u_i\, \gamma \to l^+\nu_l\, d_j$ $\bar{d}_j\, \gamma \to l^+\nu_l\, \bar{u}_i$
Zjet (l^+l^-)	$q_i\, g \to l^+l^-\, q_i$ $\bar{q}_i\, g \to l^+l^-\, \bar{q}_i$	$q_i\, \gamma \to l^+l^-\, q_i$ $\bar{q}_i\, \gamma \to l^+l^-\, \bar{q}_i$
Zjet ($\bar{\nu}\nu$)	$q_i\, g \to \bar{\nu}_l\nu_l\, q_i$ $\bar{q}_i\, g \to \bar{\nu}_l\nu_l\, \bar{q}_i$	$q_i\, \gamma \to \bar{\nu}_l\nu_l\, q_i$ $\bar{q}_i\, \gamma \to \bar{\nu}_l\nu_l\, \bar{q}_i$

Table 3.1: Gluon-induced and photon-induced partonic LO processes for W^+ + jet and Z + jet production.

$|\mathcal{M}_0^{\mathrm{W/Z+jet}}|^2$ denotes the matrix element squared of the corresponding partonic LO processes for W/Z + jet production. These processes are listed in Table 3.1.

The subtraction procedure then works analogously as described in Section 3.2.3 for the NCS case. Since we want to cut on $z_{\gamma l}$ we make its dependence explicit by using Eq. (3.57)

$$\int \mathrm{d}\Phi_1 \left[|\mathcal{M}_{\mathrm{real}}|^2 \Theta_{\mathrm{cut}}(p_i, k, p_l, \{k_n\}) - |\mathcal{M}_{\mathrm{sub}}|^2 \Theta_{\mathrm{cut}} \left((1-z_{\gamma l})\tilde{p}_i, z_{\gamma l}\tilde{p}_i, \tilde{p}_l, \{\tilde{k}_n\} \right) \right], \tag{3.58}$$

where the application of the event-selection cuts is again formalized by a step function Θ_{cut} acting on the $(N+1)$-particle phase space. Following Refs. [90, 94] for the analytic integration the contribution of the re-added counterpart to the partonic cross section reads

$$\begin{aligned} \mathrm{d}\hat{\sigma}_{\mathrm{sub}}(z_{\mathrm{cut}}, m_i) &= \frac{1}{\hat{s}} \int \mathrm{d}\Phi_1 |\mathcal{M}_{\mathrm{sub},ij}(\Phi_1)|^2 \\ &= \frac{\alpha Q_i^2}{4\pi\hat{s}}\, \mathrm{d}\tilde{\Phi}_0 \int_{z_{\mathrm{cut}}}^1 \mathrm{d}z_\gamma\, \bar{\mathcal{G}}_{il}^{(\mathrm{sub})}(P_{il}^2, 1-z_\gamma) \\ &\quad \times \left| \mathcal{M}_0^{\mathrm{W/Z+jet}}(\tilde{p}_i, \tilde{p}_l, \{\tilde{k}_n\}) \right|^2 \Theta_{\mathrm{cut}} \left(p_i = (1-z_\gamma)\tilde{p}_i, k = z_\gamma \tilde{p}_i, \tilde{p}_l, \{\tilde{k}_n\} \right), \end{aligned} \tag{3.59}$$

where z_{cut} is defined as the lower limit of z_γ and $\hat{s}$ indicates the centre-of-mass energy squared of the partonic process. Due to the application of the cut $z_\gamma > z_{\mathrm{cut}}$ the limit $z_\gamma \to 0$ is excluded and Eq. (3.59) does not include any endpoint contribution covering this soft-singular divergence. The distribution $\bar{\mathcal{G}}_{il}^{(\mathrm{sub})}$ is given by Eq. (3.40) with the substitutions $z \to z_i = 1 - z_\gamma$ and $j \to l$.

While the upper subtraction procedure only isolates the singularity but does not remove it, additional contributions to the total cross section have to be considered. These extra terms are motivated by the scenario where only a quark is produced in the hard scattering and the collinear photon is the product of the hadronization process. This effect can be described by using the non-perturbative quark-to-photon fragmentation function which is defined in Refs. [55, 56] and was experimentally measured by ALEPH [95]. The additional contribution to the cross section reads

$$\mathrm{d}\hat{\sigma}_{\mathrm{frag}}(z_{\mathrm{cut}}) = \mathrm{d}\hat{\sigma}_0 \int_{z_{\mathrm{cut}}}^1 \mathrm{d}z_\gamma\, D_{q\to\gamma}^{\mathrm{bare}}(z_\gamma)\,, \tag{3.60}$$

where $\mathrm{d}\hat{\sigma}_0$ denotes the partonic LO cross section for the process without photon radiation. The fragmentation function $D_{q\to\gamma}^{\mathrm{bare}}(z_\gamma)$ describes the probability density for a FS quark which fragments into a jet containing a photon with energy fraction z_γ. The singular contribution regularized by the infinitesimal quark mass m_i can be split off with the following equation [94]

$$D_{q\to\gamma}^{\mathrm{bare,MR}}(z_\gamma) = \frac{\alpha Q_i^2}{2\pi} P_{ff}(1-z_\gamma) \left(\ln\frac{m_i^2}{\mu_{\mathrm{F}}^2} + 2\ln z_\gamma + 1 \right) + D_{q\to\gamma}^{\overline{\mathrm{MS}}}(z_\gamma, \mu_{\mathrm{F}})\,. \tag{3.61}$$

Therein we introduced the factorization scale μ_F which separates the perturbative from the non-perturbative region. The label "MR" indicates the mass regularization. The additional collinear singularity in Eq. (3.61) now exactly compensates the singularities in the re-added counterpart which is included in $\bar{\mathcal{G}}_{il}^{(\mathrm{sub})}$. It was worked out in Ref. [94] that the finite non-perturbative contribution $D_{q\to\gamma}^{\overline{\mathrm{MS}}}$ is equivalent to the standard $\overline{\mathrm{MS}}$ scheme of dimensional regularization. We implemented the parametrization used by the ALEPH collaboration [95]

$$D_{q\to\gamma}^{\mathrm{ALEPH},\overline{\mathrm{MS}}}(z_\gamma,\mu_\mathrm{F}) = \frac{\alpha Q_i^2}{2\pi}\left(P_{ff}(1-z_\gamma)\ln\frac{\mu_\mathrm{F}^2}{(1-z_\gamma)^2\mu_0^2}+C\right), \tag{3.62}$$

with the parameters set to

$$\mu_0 = 0.14\,\mathrm{GeV} \text{ and } C = -13.26 \tag{3.63}$$

and constrained by $C = -1+\ln(2\mu_0^2/M_\mathrm{Z}^2)$. Summing up the contributions for the cross section from Eq. (3.59) and Eq. (3.60) with $D_{q\to\gamma}^{\overline{\mathrm{MS}}}$ defined in Eq. (3.61) leads to (see Eq. (4.63) in Ref. [94])

$$\begin{aligned}
&\mathrm{d}\hat{\sigma}_\mathrm{sub}(z_\mathrm{cut},m_i)+\mathrm{d}\hat{\sigma}_\mathrm{frag}(z_\mathrm{cut},m_i)\\
&\quad= \frac{\alpha Q_i^2}{4\pi\hat{s}}\,\mathrm{d}\tilde{\Phi}_0\left|\mathcal{M}_0^{\mathrm{W/Z+jet}}(\tilde{\Phi}_0)\right|^2\int_0^{1-z_\mathrm{cut}}\mathrm{d}z_i\left(D_{q\to\gamma}^{\mathrm{bare,MR}}(1-z_i)+\bar{\mathcal{G}}_{il}^{(\mathrm{sub})}(P_{il}^2,z_i)\right)\\
&\quad= \frac{\alpha Q_i^2}{4\pi\hat{s}}\,\mathrm{d}\tilde{\Phi}_0\left|\mathcal{M}_0^{\mathrm{W/Z+jet}}(\tilde{\Phi}_0)\right|^2\left\{\left(1+C+\frac{z_\mathrm{cut}}{2}\right)(1-z_\mathrm{cut})\right.\\
&\qquad-\left(\frac{1}{2}(1-z_\mathrm{cut})(3-z_\mathrm{cut})+2\ln(z_\mathrm{cut})\right)\ln\left(\frac{z_\mathrm{cut}}{1-z_\mathrm{cut}}\frac{P_{il}^2}{\mu_0^2}\right)\\
&\qquad\left.+2\,\mathrm{Li}_2(1-z_\mathrm{cut})+\frac{3}{2}\ln(z_\mathrm{cut})\right\},
\end{aligned} \tag{3.64}$$

which is finite and only depends on the value z_cut.

3.5.2 Frixione isolation scheme

An alternative to the concept of democratic clustering in combination with the quark-to-photon fragmentation function is the Frixione isolation scheme introduced in Ref. [57]. Here, we employ an additional cut condition which ensures that specific phase-space regions containing potential IR singularities of the photon–jet system are excluded. Events will be discarded if the rapidity–azimuthal-angle difference $R_{\gamma\mathrm{jet}}$ (defined in Eq. (3.53)) is smaller than the cone size R_0 and the condition

$$p_{\mathrm{T,jet}} < \varepsilon\, p_{\mathrm{T},\gamma}\left(\frac{1-\cos(R_{\gamma\mathrm{jet}})}{1-\cos(R_0)}\right) \tag{3.65}$$

does not hold. Therein $p_{\mathrm{T,jet}}$ and $p_{\mathrm{T},\gamma}$ indicate the transverse momenta of the jet and the photon. The parameter ε controls the allowed range of the hadronic energy fraction in the cone around the photon. This single condition treats singular configurations of photon and jets in the following way:

- If the photon and the jet become collinear, i.e. $R_{\gamma\mathrm{jet}}\to 0$, relation (3.65) is violated and the event is discarded.
- If the photon becomes soft or collinear to the beam axis, i.e. $p_{\mathrm{T},\gamma}\to 0$, relation (3.65) is violated and the event is discarded.

- If the jet becomes soft or collinear to the beam axis, i.e. $p_{\mathrm{T,jet}} \to 0$, relation (3.65) is respected and the event is not discarded. This guarantees that IR singularities related to gluons cancel between real and virtual corrections.

In order to compensate IR singularities from virtual QCD corrections (as predicted by the KLN theorem [83, 84]) Eq. (3.65) ensures that soft or collinear jets are treated inclusively while soft and collinear photons are excluded.

Since we want to compare the results achieved with quark-to-photon fragmentation function and Frixione isolation scheme, the parameters of both methods have to matched. Rearranging Eq. (3.65) results in

$$\frac{p_{\mathrm{T},\gamma}}{p_{\mathrm{T},\gamma} + p_{\mathrm{T,jet}}} > \frac{1}{1 + \varepsilon \frac{1-\cos\left(R_{\gamma\mathrm{jet}}\right)}{1-\cos(R_0)}} \tag{3.66}$$

and leads to a relation which is comparable with the definition of the photon energy fraction in Eq. (3.55). Assuming the same value for the cone size R_0 we find

$$z_{\mathrm{cut}} \approx \frac{1}{1+\varepsilon} \tag{3.67}$$

as a matching condition. We will used this relation in Chapter 4 to produce comparable results for both schemes.

Chapter 4

Numerical results for $\mathrm{V}+\gamma$ production

In this chapter we present results on total cross sections and distributions in various setups. First, in Section 4.1 we define the NLO cross section with contributions from QCD and EW corrections. In Section 4.2 we discuss the relevant input parameters and in Section 4.3 we outline the event selection and the application of the phase-space cuts. In Sections 4.4–4.7 we present results for a full NLO calculation to the processes defined in Eqs. (2.1)–(2.4). Each section includes results for the total cross section and a set of distributions for several kinematic observables depending on the explicit process. The results presented in this chapter are published in Refs. [69] and [70].

4.1 General setup

NLO corrections to $\mathrm{W}+\gamma$ and $\mathrm{Z}+\gamma$ production can be divided in EW and QCD corrections of the orders $\mathcal{O}(\alpha)$ and $\mathcal{O}(\alpha_s)$, respectively. We denote the LO cross section calculated with LO PDFs by σ^{LO}. The NLO-QCD-corrected cross section is obtained as

$$\begin{aligned}\sigma^{\mathrm{NLO\,QCD}} &= \sigma^{0} + \Delta\sigma^{\mathrm{NLO\,QCD}}\,,\\ \Delta\sigma^{\mathrm{NLO\,QCD}} &= \sigma^{\alpha_s}_{\mathrm{real}} + \sigma^{\alpha_s}_{\mathrm{virt}} + \sigma^{\alpha_s}_{\mathrm{col}} + \sigma^{\alpha_s}_{\mathrm{frag}}\,,\end{aligned} \tag{4.1}$$

where all contributions, including the LO cross section σ^0, are calculated with NLO PDFs. The real and the virtual corrections are given by $\sigma^{\alpha_s}_{\mathrm{real}}$ and $\sigma^{\alpha_s}_{\mathrm{virt}}$, respectively, the contribution $\sigma^{\alpha_s}_{\mathrm{col}}$ originates from the redefinition of the PDFs (see Section 1.3), and $\sigma^{\alpha_s}_{\mathrm{frag}}$ represents the contribution from fragmentation of a quark into a photon. All individual parts in the NLO QCD contribution $\Delta\sigma^{\mathrm{NLO\,QCD}}$ are IR divergent and only their sum is IR finite. The separation between $\mathrm{W/Z}+\gamma$ and $\mathrm{W/Z}+\mathrm{jet}$ production is evident at LO. Since the final states of the processes defined in Eqs. (2.9)–(2.11) and Eqs. (2.12)–(2.14) also appear in the real NLO corrections to $\mathrm{W/Z}+\mathrm{jet}$ production these processes require special care. The technical details of this aspect are discussed in Section 3.5.

Analogously to the QCD corrections, the EW corrections are given by

$$\begin{aligned}\Delta\sigma^{\mathrm{NLO\,EW}}_{q\bar{q}} &= \sigma^{\alpha}_{q\bar{q},\mathrm{real}} + \sigma^{\alpha}_{q\bar{q},\mathrm{virt}} + \sigma^{\alpha}_{q\bar{q},\mathrm{col}}\,,\\ \Delta\sigma^{\mathrm{NLO\,EW}}_{q\gamma} &= \sigma^{\alpha}_{q\gamma,\mathrm{real}} + \sigma^{\alpha}_{q\gamma,\mathrm{col}} + \sigma^{\alpha}_{q\gamma,\mathrm{frag}}\,,\\ \Delta\sigma_{\gamma\gamma} &= \sigma^{0}_{\gamma\gamma}\,,\end{aligned} \tag{4.2}$$

where the quark–antiquark-induced EW corrections $\Delta\sigma^{\mathrm{NLO\,EW}}_{q\bar{q}}$ and the photon-induced corrections $\Delta\sigma^{\mathrm{NLO\,EW}}_{q\gamma}$ are finite, while their individual contributions are IR divergent. Additionally, for the $\mathrm{Z}\gamma$ production process where the final state contains two charged leptons $\Delta\sigma_{\gamma\gamma}$ describes the LO contribution from photon–photon-induced diagrams.

Unlike the quark–antiquark- and the quark–gluon-induced channels in the QCD corrections, $\Delta\sigma^{\text{NLO EW}}_{q\bar{q}}$ and $\Delta\sigma^{\text{NLO EW}}_{q\gamma}$ can (in principle) be distinguished by their final states. Analogously to the QCD case, in Eq. (4.2) $\sigma^{\alpha}_{ij,\text{real}}$ and $\sigma^{\alpha}_{q\bar{q},\text{virt}}$ denote the real and the virtual corrections, respectively, and $ij = q\bar{q}, q\gamma$. Terms originating from the PDF redefinition furnish $\sigma^{\alpha}_{ij,\text{col}}$, and the fragmentation contribution is described by $\sigma^{\alpha}_{q\gamma,\text{frag}}$. Note that no fragmentation contribution is required in the $q\bar{q}$ channel at NLO EW, because there is no jet in the final state in this order.

We choose to combine QCD and EW corrections using the naive product for QCD and quark–antiquark EW corrections and we further linearly add contributions from photon-induced and (if present) photon–photon-induced processes

$$\begin{aligned}\sigma^{\text{NLO}} &= \sigma^{\text{LO}}\left[(1+\delta_{\text{QCD}})\,(1+\delta_{\text{EW},q\bar{q}}) + \delta_{\text{EW},q\gamma}\Big(+\delta_{\gamma\gamma}\Big)\right] \\ &= \sigma^{\text{NLO QCD}}\,(1+\delta_{\text{EW},q\bar{q}}) + \Delta\sigma^{\text{NLO EW}}_{q\gamma}\Big(+\Delta\sigma_{\gamma\gamma}\Big)\,,\end{aligned} \tag{4.3}$$

where the relative QCD, EW and photon–photon-induced corrections are defined by

$$\begin{aligned}\delta_{\text{QCD}} &= \frac{\sigma^{\text{NLO QCD}} - \sigma^{\text{LO}}}{\sigma^{\text{LO}}}\,, & \delta_{\text{EW},q\bar{q}} &= \frac{\Delta\sigma^{\text{NLO EW}}_{q\bar{q}}}{\sigma^{0}}\,, \\ \delta_{\text{EW},q\gamma} &= \frac{\Delta\sigma^{\text{NLO EW}}_{q\gamma}}{\sigma^{\text{LO}}}\,, & \delta_{\gamma\gamma} &= \frac{\Delta\sigma_{\gamma\gamma}}{\sigma^{\text{LO}}}\,,\end{aligned} \tag{4.4}$$

respectively. While the relative QCD corrections are normalized to the LO cross section σ^{LO}, calculated with LO PDFs, the quark–antiquark-induced EW corrections are normalized to the LO cross section σ^{0}, calculated with NLO PDFs. By this definition, $K_{\text{QCD}} = 1 + \delta_{\text{QCD}}$ is the standard QCD factor, and the relative quark–antiquark-induced EW corrections $\delta_{\text{EW},q\bar{q}}$ are practically independent of the PDF set.

In order to ensure the accuracy of our results a second independent calculation was performed by Stefan Dittmaier and Markus Hecht. In this calculation the virtual amplitudes are generated by `FEYNARTS` 1 [96] and algebraically reduced with an in-house `MATHEMATICA` package, automatically transferring the results into a `FORTRAN` code. For the numerical evaluation of integrated and differential cross sections the amplitudes are implemented into a `FORTRAN` program using the `VEGAS` algorithm for a proper numerical integration. In case of $\text{W/Z} + \gamma$ production sharp resonances appear, demanding additional phase-space mappings. Therefore, analytical Breit–Wigner mappings are introduced in the phase-space parametrization, allowing for a stable numerical integration by flattening the integrand.

4.2 Input parameters

The relevant SM input parameters are

$$\begin{array}{lll} G_\mu = 1.1663787\times10^{-5}\,\text{GeV}^{-2}, & \alpha(0) = 1/137.035999074\,, & \alpha_{\text{s}}(M_{\text{Z}}) = 0.119\,, \\ M_{\text{H}} = 125\,\text{GeV}, & m_\mu = 105.6583715\,\text{MeV}, & m_{\text{t}} = 173.07\,\text{GeV}, \\ M_{\text{W}}^{\text{OS}} = 80.385\,\text{GeV}, & \Gamma_{\text{W}}^{\text{OS}} = 2.085\,\text{GeV}, & \\ M_{\text{Z}}^{\text{OS}} = 91.1876\,\text{GeV}, & \Gamma_{\text{Z}}^{\text{OS}} = 2.4952\,\text{GeV}, & \\ |V_{\text{us}}| = |V_{\text{cd}}| = 0.225\,, & |V_{\text{ud}}| = |V_{\text{cs}}| = \sqrt{1-|V_{\text{us}}|^2}\,. & \end{array} \tag{4.5}$$

All parameters but $\alpha_{\text{s}}(M_{\text{Z}})$ in (4.5) are extracted from Ref. [97]. $\alpha_{\text{s}}(M_{\text{Z}})$ is provided by the PDF set. The masses of all quarks but the top quark are set to zero. CKM mixing between the first two quark generations is taken into account in all partonic cross sections, but mixing to the third generation is not included, since it is negligible. For $\text{W}\gamma$ production this implies that there is no contribution from bottom quarks in the initial state. Since the $b\bar{b}$ channel for $\text{Z}\gamma$ production

contributes only about 3% to the LO cross section, we omit the corresponding virtual EW corrections which we expect to be in the sub per-mille level and therefore negligible. Bottom quarks in the initial state are taken into account for QCD and photon-induced corrections but are neglected for the quark–antiquark-induced EW corrections. Additionally, the CKM matrix drops out in the flavour sum of closed fermion loops, thus, the CKM matrix factorizes from all amplitudes, so that only one generic amplitude has to be evaluated when convoluting the squared matrix elements with the PDFs.

Owing to the presence of an on-shell external photon, we always take one electromagnetic coupling constant α at zero momentum transfer, $\alpha = \alpha(0)$. For the other couplings, e.g. of the W boson to fermions, we determine the electromagnetic coupling constant in the G_μ scheme, where α is defined in terms of the Fermi constant (see Eq. (1.55)). Using this mixed scheme the squared LO amplitude is proportional to $\alpha(0)\alpha_{G_\mu}^2$. In the relative EW corrections we set the additional coupling factor α to α_{G_μ}, because this coupling is adequate for the most pronounced EW corrections which are caused by soft/collinear weak gauge-boson exchange at high energies (EW Sudakov logarithms, etc.).

We apply the complex-mass scheme [75–77] to describe the W-boson and Z-boson resonance by introducing complex vector-boson masses (see Eq. (1.42)) with constant widths. However, at LEP and the Tevatron the on-shell (OS) masses of the vector bosons were measured, which correspond to running widths. The OS masses M_W^OS, M_Z^OS and widths $\Gamma_\mathrm{W}^\mathrm{OS}$, $\Gamma_\mathrm{Z}^\mathrm{OS}$ have to be converted to the pole values using the relations [98]

$$M_\mathrm{V} = M_\mathrm{V}^\mathrm{OS}/\sqrt{1+(\Gamma_\mathrm{V}^\mathrm{OS}/M_\mathrm{V}^\mathrm{OS})^2}\,, \qquad \Gamma_\mathrm{V} = \Gamma_\mathrm{V}^\mathrm{OS}/\sqrt{1+(\Gamma_\mathrm{V}^\mathrm{OS}/M_\mathrm{V}^\mathrm{OS})^2} \qquad (\mathrm{V}=\mathrm{W},\ \mathrm{Z})\,, \quad (4.6)$$

leading to

$$\begin{aligned} M_\mathrm{W} &= 80.3580\ldots\ \mathrm{GeV}, \qquad \Gamma_\mathrm{W} = 2.0843\ldots\ \mathrm{GeV}, \\ M_\mathrm{Z} &= 91.1535\ldots\ \mathrm{GeV}, \qquad \Gamma_\mathrm{Z} = 2.4943\ldots\ \mathrm{GeV}. \end{aligned} \quad (4.7)$$

Calculating the hadronic cross section, we use the $\mathcal{O}(\alpha)$-corrected NLO PDF set NNPDF23QED, which includes the two-loop running of α_s for five active flavours ($n_f = 5$).

The factorization and the renormalization scales $\mu_\mathrm{F}, \mu_\mathrm{R}$ are set equal throughout our calculation. Following Refs. [99, 100], we choose the scales as

$$\mu_\mathrm{F}^2 = \mu_\mathrm{R}^2 = \frac{1}{2}\left(M_\mathrm{V}^2 + p_{\mathrm{T},\mathrm{V}}^2 + p_{\mathrm{T},\gamma_1}^2 + p_{\mathrm{T},\gamma_2/\mathrm{jet}}^2\right) \qquad (\mathrm{V}=\mathrm{W},\ \mathrm{Z})\,, \quad (4.8)$$

where $p_{\mathrm{T,V}}$ is the transverse momentum of the massive vector boson defined by

$$p_{\mathrm{T},\mathrm{V}} = |\mathbf{p}_{\mathrm{T},l/\nu} + \mathbf{p}_{\mathrm{T},l/\nu}|\,, \quad (4.9)$$

and $p_{\mathrm{T},a} = |\mathbf{p}_{\mathrm{T},a}|$ denotes the absolute value of the transverse three-momentum $\mathbf{p}_{\mathrm{T},a}$ of particle a. The photons γ_1 and γ_2 are assigned so that $p_{\mathrm{T},\gamma_1} > p_{\mathrm{T},\gamma_2}$. In LO the transverse momenta $p_{\mathrm{T},\gamma_2/\mathrm{jet}}$ are zero.

The QCD scale uncertainty of Wγ and Zγ production has already been investigated in various publications such as in Refs. [32, 33]. Varying the scale by a factor of two the scale dependence is found to be of the order of 10% at NLO in Ref. [33], where the scale is defined similarly as in our calculation. Imposing a jet veto significantly reduces the scale dependence as found in both calculations [32, 33] using slightly different jet definitions. Meanwhile NNLO QCD corrections have been calculated and found to be 19% [101] and 6% [45] for Wγ and Zγ production, respectively. Consequently, a meaningful estimate of the residual scale dependence should be performed including the NNLO QCD corrections.

4.3 Phase-space cuts and event selection

The processes of Wγ and Zγ production require the recombination of final-state (FS) photons with FS partons and, where appropriate, of FS photons with charged leptons in regimes of phase space where photon and parton/lepton are collinear. Furthermore, we impose several cuts to account for the detector acceptance. The phase-space cuts and the event selection are inspired by the recent ATLAS and CMS papers [16–18] analysing $V\gamma$ final states.

Recombination

To decide whether a photon and a FS particle need to be recombined we use the Euclidean distance in the y–ϕ plane, $R_{ij} = \sqrt{(y_i - y_j)^2 + \phi_{ij}^2}$, where $y = \frac{1}{2}\ln\left[(E + p_\mathrm{L}) / (E - p_\mathrm{L})\right]$ denotes the rapidity. In this equation E is the energy and p_L the longitudinal momentum of the respective particle with respect to the beam axis. The value ϕ_{ij} denotes the angle between the particles i and j in the plane perpendicular to the beams. The recombination proceeds as follows:

1. If we consider "bare" muons, a photon and a charged (anti)lepton are never recombined. Otherwise recombination is applied if $R_{l^\pm\gamma} < 0.1$, and the four-momenta of photon and lepton are added. If the separation in R between the photon and each of the two leptons is smaller than 0.1 at the same time, the photon is recombined with the lepton that has a smaller $R_{l\gamma}$ separation. In case of two photons in the final state, first the photon with the smaller $R_{l^\pm\gamma}$ is recombined.

2. Two photons are recombined if $R_{\gamma\gamma} < 0.1$.

3. Using the method of democratic clustering a photon and a jet are recombined if the distance between them becomes $R_{\gamma\mathrm{jet}} < R_0 = 0.5$. After recombination, the energy fraction $z_\gamma = E_\gamma / (E_\gamma + E_\mathrm{jet})$ of the photon inside the photon–jet system is determined. Using this value we decide if the event belongs to the process $\mathrm{W/Z} + \gamma$ or $\mathrm{W/Z} + \mathrm{jet}$. If z_γ is smaller than the cut value $z_\mathrm{cut} = 0.9$ the event is regarded as a part of the process $\mathrm{W/Z} + \mathrm{jet}$ and is therefore rejected.

The case where more than two particles are recombined is excluded by our basic cuts. Results are presented for "bare" muons and for photon recombination with leptons. The latter results hold for electrons as well as for muons, since the lepton-mass logarithms cancel as dictated by the KLN theorem [83, 84].

If alternatively the Frixione isolation scheme is applied, step 3 has to be replaced as follows:

3'. If $R_{\gamma\mathrm{jet}} < R_0 = 0.5$ the photon and the jet are recombined and the event is only accepted if it respects the criterion (3.65). Based on Eq. (3.67) we choose $\varepsilon = 0.11$ corresponding to $z_\mathrm{cut} = 0.9$.

Basic cuts

After recombination, we define $\mathrm{W} + \gamma$ events by the following cut procedure:

1. We demand a charged lepton with transverse momentum $p_{\mathrm{T},l} > 25\,\mathrm{GeV}$ and

2. missing transverse momentum $p_{\mathrm{T,miss}} > 25\,\mathrm{GeV}$, where $p_{\mathrm{T,miss}}$ is equal to the neutrino transverse momentum.

3. We demand at least one photon with transverse momentum $p_{\mathrm{T},\gamma} > 15\,\mathrm{GeV}$ that is isolated from the charged lepton with a distance of $R_{l\gamma} > 0.7$.

4. The charged lepton and the photon passing the cuts at step 1 and step 3 have to be central, i.e. their rapidities have to be in the range $|y| < 2.5$.

5. Only events with a transverse mass of the lepton pair $M_{\mathrm{T},l^+\nu} > 40\,\mathrm{GeV}$ are accepted, where

$$M_{\mathrm{T},l^+\nu} = \sqrt{2 p_{\mathrm{T},l^+}\, p_{\mathrm{T,miss}}\,(1 - \cos\left(\Delta\phi_{l^+,\mathrm{miss}}\right))} \tag{4.10}$$

and $\Delta\phi_{l,\mathrm{miss}}$ is the azimuthal-angle separation between the directions of the charged lepton and the missing transverse momentum.

For a $\mathrm{Z} + \gamma$ event where the final state contains two charged leptons the basic cuts are:

1. We demand two charged leptons with transverse momentum $p_{\mathrm{T},\,l} > 25\,\mathrm{GeV}$.

2. At least one photon with transverse momentum $p_{\mathrm{T},\gamma} > 15\,\mathrm{GeV}$ has to be isolated from the two charged leptons with a distance of $R_{l\gamma} > 0.7$.

3. The charged leptons and the photon have to be central, i.e. their rapidities have to be in the range $|y| < 2.5$.

4. Only events with an invariant mass of the charged lepton pair $M_{l^+l^-} > 40\,\mathrm{GeV}$ are accepted, where

$$M_{l^+l^-} = \sqrt{(p^0_{l^+} + p^0_{l^-})^2 - (\mathbf{p}_{l^+} + \mathbf{p}_{l^-})^2}\,. \tag{4.11}$$

A $\mathrm{Z} + \gamma$ event, where the Z boson decays in two neutrinos, is defined by the following cuts:

1. We demand a missing transverse momentum $p_{\mathrm{T,miss}} > 90\,\mathrm{GeV}$, where $p_{\mathrm{T,miss}}$ is defined as

$$p_{\mathrm{T,miss}} = \left|\mathbf{p}_{\mathrm{T},\nu_1} + \mathbf{p}_{\mathrm{T},\nu_2}\right|. \tag{4.12}$$

2. At least one photon has to be central with $|y_\gamma| < 2.5$ and has to possess transverse momentum $p_{\mathrm{T},\gamma} > 100\,\mathrm{GeV}$.

3. We demand the photon passing step 2 has to fulfil $\Delta\phi_{\mathrm{miss},\gamma} > 2.6$, with the azimuthal-angle difference

$$\Delta\phi_{\mathrm{miss},\gamma} = \mathrm{acos}\left(\frac{\mathbf{p}_{\mathrm{T},\gamma}\cdot\mathbf{p}_{\mathrm{T,miss}}}{p_{\mathrm{T},\gamma}\, p_{\mathrm{T,miss}}}\right). \tag{4.13}$$

For all processes we present results with and without applying a jet veto. Applying a jet veto means that all events including a FS jet with $p_{\mathrm{T,jet}} > 100\,\mathrm{GeV}$ are discarded. Experimentally a jet is required to lie in the rapidity range $|y| < 4.4$. However, in our calculation we do not restrict the rapidity range of the vetoed jets, since the impact on the cross section is very small and lies within the theoretical error.

4.4 Results for $\mathrm{p\ p} \to l^+\ \nu_l\ \gamma\ + X$

4.4.1 Results on total cross section

In Table 4.1 we present the LO cross sections σ^{LO} for different pp centre-of-mass energies $\sqrt{s}$ and the different types of relative corrections δ defined in Eq. (4.4). For the EW corrections resulting from the quark–antiquark channels we show results for CS and NCS observables.

$\sqrt{s}$/ TeV	7	8	14
σ^{LO}/ fb	846.40(12)	940.20(14)	1448.00(23)
$\delta^{\text{NCS}}_{\text{EW},q\bar{q}}$/%	−3.14	−3.14	−3.12
$\delta^{\text{CS}}_{\text{EW},q\bar{q}}$/%	−1.94	−1.94	−1.95
$\delta^{\text{frag}}_{\text{EW},q\gamma}$/%	1.28	1.35	1.62
$\delta^{\text{veto, frag}}_{\text{EW},q\gamma}$/%	0.90	0.94	1.05
$\delta^{\text{Frix}}_{\text{EW},q\gamma}$/%	1.29	1.36	1.63
$\delta^{\text{veto, Frix}}_{\text{EW},q\gamma}$/%	0.91	0.95	1.06
$\delta^{\text{frag}}_{\text{QCD}}$/%	121.90(13)	128.00(14)	153.90(15)
$\delta^{\text{veto, frag}}_{\text{QCD}}$/%	112.00(17)	116.80(17)	135.90(19)
$\delta^{\text{Frix}}_{\text{QCD}}$/%	123.50(23)	129.90(21)	156.40(25)
$\delta^{\text{veto, Frix}}_{\text{QCD}}$/%	113.70(23)	118.70(21)	138.70(25)

Table 4.1: Integrated cross sections and relative corrections for $W^+\gamma$ production at different LHC energies. The EW corrections to the quark–antiquark annihilation channels are provided with (CS) and without (NCS) lepton–photon recombination. EW corrections from the photon-induced channels and QCD corrections are shown with a jet veto (veto) as well as without a jet veto using democratic clustering and fragmentation function (frag) or the Frixione isolation criterion (Frix) to separate photons and jets. The numbers in parentheses denote the integration error in the last digits. This error is negligible for the relative EW corrections at the given accuracy.

Results for the EW corrections originating from photon-induced channels and for the QCD corrections are listed with and without a jet veto. Furthermore, we present results obtained by applying democratic clustering in combination with a quark-to-photon fragmentation function and the Frixione isolation scheme indicated by "frag" and "Frix", respectively. The different relative corrections depend only weakly on the collider energy. By far the largest effect ($\sim$ 120−150%) comes from the QCD corrections, even in case of a jet veto. About two thirds of the relative QCD corrections are due to gluon-induced channels. The results obtained with the fragmentation function and the Frixione isolation scheme differ by $2-3\%$ and $0-1\%$ in case of the QCD and the photon-induced EW corrections, respectively. The EW corrections to the quark–antiquark channels are about -2% and -3% for the CS and the NCS case, respectively. The photon-induced corrections contribute between 0.7% and 1.3% with and without a jet veto. Summing up, the total EW corrections to the integrated cross section are small and not significant for the most-recent experimental cross-section measurements. However, larger corrections show up in differential distributions, as demonstrated in the next sections.

4.4.2 Results on transverse-momentum distributions

In the following we present the distributions including EW and QCD corrections for various observables in separate plots for a centre-of-mass energy of 14 TeV. For each distribution we also show the relative EW corrections of the $q\bar{q}$ for the CS and the NCS case and $q\gamma$ channels as well as the QCD corrections with and without a jet veto. Since the difference between the quark-to-photon fragmentation function and the Frixione isolation scheme is of the order of 2%, we only present results obtained with the fragmentation function in the following. Note that diminishing the cut on the energy fraction of the photon inside a jet to $z_{\text{cut}} = 0.7$ doubles the difference between the two methods.

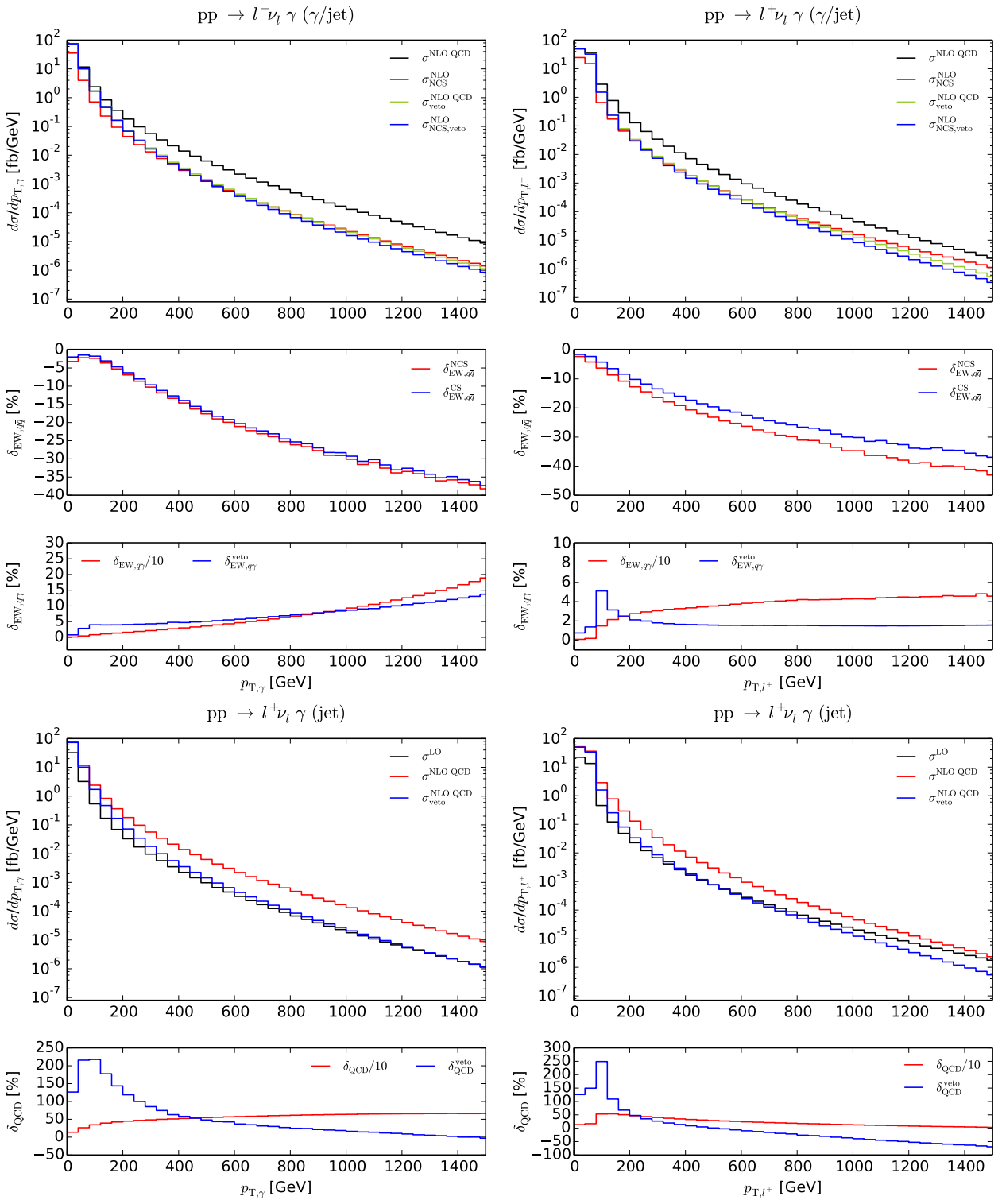

Figure 4.1: Distributions in the transverse momentum p_T of the photon (left) and the charged lepton (right), including EW (top) and QCD corrections (bottom). For all corrections absolute (upper box) and relative corrections (lower boxes) are shown.

In Fig. 4.1 we show results for transverse-momentum distributions. Focusing on the $p_{\mathrm{T},\gamma}$ distribution of the photon (within cuts) with the highest transverse momentum we can see (Fig. 4.1, left, bottom) that the QCD corrections without a jet veto reach 650% for large transverse momenta (scaled down by a factor 10 in Fig. 4.1). This is due to the fact that new production channels occur ($q\,g \to l\,\nu\,\gamma\,q$) at NLO QCD causing large corrections (550% for large $p_{\mathrm{T},\gamma}$). However, these large corrections come from events with hard jets, meaning that they should better be considered as part of W + jet rather than W + γ production. For this reason we also present results for the case of a jet veto, where all events with jets with $p_{\mathrm{T,jet}} > 100\,\mathrm{GeV}$ are discarded. In this case the QCD corrections become small for large $p_{\mathrm{T},\gamma}$, since the jet veto suppresses the contribution of the real QCD corrections and especially of the gluon-induced channels.

Owing to the so-called EW Sudakov logarithms the EW corrections (Fig. 4.1, left, top) contribute with large negative corrections in the high-p_{T} range, though one order of magnitude smaller than the QCD corrections. The CS and the NCS cases hardly differ in the p_{T} distribution of the hardest photon, since the recombination of another photon collinearly emitted off the lepton only marginally effects the p_{T} of the hard photon.

The photon-induced corrections are positive and become surprisingly large for large transverse momenta, reaching the same order of magnitude as the QCD corrections. In fact in the discussion of the relative impact of the photon-induced corrections it would be more appropriate to normalize to the NLO QCD cross section, which is dominated by the new channels for hard jet emission at high scales. With this normalization the $q\gamma$ channels still contribute some tens of percent at high $p_{\mathrm{T},\gamma}$ with a rising tendency for growing $p_{\mathrm{T},\gamma}$, which can be understood by the increasing γ/g PDF ratio for high Bjorken-x (see Fig. 1.2) and the decrease in the strong coupling constant driven by the dynamical renormalization scale. Note, however, that the photon PDF at large Bjorken-x suffers from huge uncertainties of up to 100%, so that we have to conclude that the high-p_{T} tail of the $p_{\mathrm{T},\gamma}$ distribution in the TeV range is plagued by PDF uncertainties which are of the size of the $q\gamma$ contribution itself. Similarly to the huge QCD corrections, the large impact of the photon-induced corrections at high $p_{\mathrm{T},\gamma}$ is reduced to the level of 10−15% by a jet veto, showing that those large effects are caused by hard jet emission. The jet veto, thus, helps to suppress the impact of the $q\gamma$ contribution and the corresponding large uncertainties in the high-p_{T} regime. After applying the veto, in fact the quark–antiquark-induced EW corrections become the dominating corrections for large transverse momenta.

In case of the p_{T} distribution of the charged lepton (Fig. 4.1, right) the QCD corrections without jet veto are large in the small-p_{T} range and become small for large transverse momenta. In contrast the EW corrections become sizeable in the region of large transverse momenta. The corrections are roughly 5% smaller in the CS case than in the NCS case. Collinear photon emission reduces the lepton momentum, so that events with large p_{T,l^+} before the emission migrate to smaller p_{T,l^+}, leading to negative corrections on the falling distribution in p_{T,l^+}. Photon recombination damps this effect upon shifting the major part of these migrating events back to the p_{T,l^+} value before photon emission. For the case without jet veto the quark–antiquark and photon-induced EW corrections are of the same order of magnitude, but of opposite sign, and accidentally compensate each other to a large extent. In case of a jet veto the QCD corrections become large and negative for large p_{T,l^+}. The large negative corrections result from the quark–antiquark-induced channels, while the corrections due to the gluon-induced channels remain small also for a jet veto. This fits well to the fact that the photon-induced corrections become negligible everywhere.

4.4.3 Results on transverse-mass distributions

The transverse mass of the W boson is defined in Eq. (4.10) and the transverse three-body mass of the W-decay products and the photon by

$$M_{\mathrm{T},l^+\nu\gamma} = \sqrt{\left(\sqrt{M_{l^+\gamma}^2 + \left|\mathbf{p}_{\mathrm{T},l^+} + \mathbf{p}_{\mathrm{T},\gamma}\right|^2} + p_{\mathrm{T,miss}}\right)^2 - \left|\mathbf{p}_{\mathrm{T},l^+} + \mathbf{p}_{\mathrm{T},\gamma} + \mathbf{p}_{\mathrm{T,miss}}\right|^2}, \tag{4.14}$$

where $M_{l^+\gamma}$ is the invariant mass of the charged lepton and the photon, defined analogous to Eq. (4.11). The corresponding distributions are shown in Fig. 4.2. The smaller peak in the $M_{\mathrm{T},l^+\nu}$ distribution at 60 GeV appearing already at LO originates from events where the three-body invariant mass $M_{\mathrm{T},l^+\nu\gamma}$ lies in the resonance region and the photon is radiated by the charged FS lepton shifting the peak to smaller transverse masses. Since events with photons close to the FS lepton are discarded, a dip appears above the lower peak. As can be seen in Fig. 4.2, the QCD corrections are dominating the $M_{\mathrm{T},l^+\nu}$ distribution with and without a jet veto. At the W-mass peak, the EW corrections reach -4% with photon recombination and -8% in the NCS case, where the photon radiated collinear to the charged lepton carries away energy, shifting more events to regions of smaller transverse mass, where those events positively contribute to the EW corrections below the W-boson resonance. The photon-induced corrections are negligible with and without a jet veto. We note in passing that previous calculations [52, 54] of EW corrections to $\mathrm{W} + \gamma$ production, which treat the W boson in pole approximation, cannot predict the range in $M_{\mathrm{T},l^+\nu}$ exceeding M_{W} which forces the W boson to go off its mass shell, while our calculation covers resonant and non-resonant regions in NLO accuracy.

We turn to the $M_{\mathrm{T},l^+\nu\gamma}$ distribution analysed experimentally in Ref. [18]. While the QCD corrections are dominating the region of small transverse masses, the EW and photon-induced corrections are small and have opposite signs there. In the high-$M_{\mathrm{T},l^+\nu\gamma}$ region the situation is different. Here the QCD corrections reduce to 50% and in case of a jet veto almost tend to zero. In contrast, the EW and the photon-induced corrections without a jet veto are about 20%, but accidentally compensate each other partly. However, imposing a jet veto reduces the photon-induced corrections to 5%. As a result, the EW corrections are not compensated by the photonic corrections anymore, becoming the dominant contribution.

4.4.4 Results on rapidity and angular distributions

In Fig. 4.3 we show the rapidity distributions of the photon and the charged lepton. In both distributions the relative EW corrections are small and almost constant over the whole range, and thus essentially given by the corrections to the total cross section. The photon-induced contributions are of comparable magnitude, but have opposite sign so that they partially cancel the EW corrections. The QCD corrections amount to $100-180\%$ for the rapidity distribution of the photon and to $140-160\%$ for the one of the charged lepton and lead to sizeable shape distortions. EW corrections are completely swamped by QCD uncertainties in these observables.

In Fig. 4.4 we present the distributions in rapidity and the azimuthal-angle difference between the charged lepton and the photon. Note that the shape of the LO rapidity-difference distribution is highly sensitive to the chosen phase-space cuts. A potential dip at $\Delta y_{l^+\gamma} = 0$ indicating the radiation zero [33, 37, 102] is not present in the setup described in Section 4.3, but becomes visible for cuts $p_{\mathrm{T},\gamma} > 20\,\mathrm{GeV}$ or $p_{\mathrm{T,miss}} > 40\,\mathrm{GeV}$ (not shown explicitly). The kink around 40° in the $\Delta\phi_{l^+\gamma}$ distribution is a result of the isolation cut $R_{l^+\gamma} > 0.7$ which suppresses the phase-space region with small azimuthal angle between charged lepton and photon. The EW and photon-induced corrections in Fig. 4.4 are at the level of 5% and affect the shape

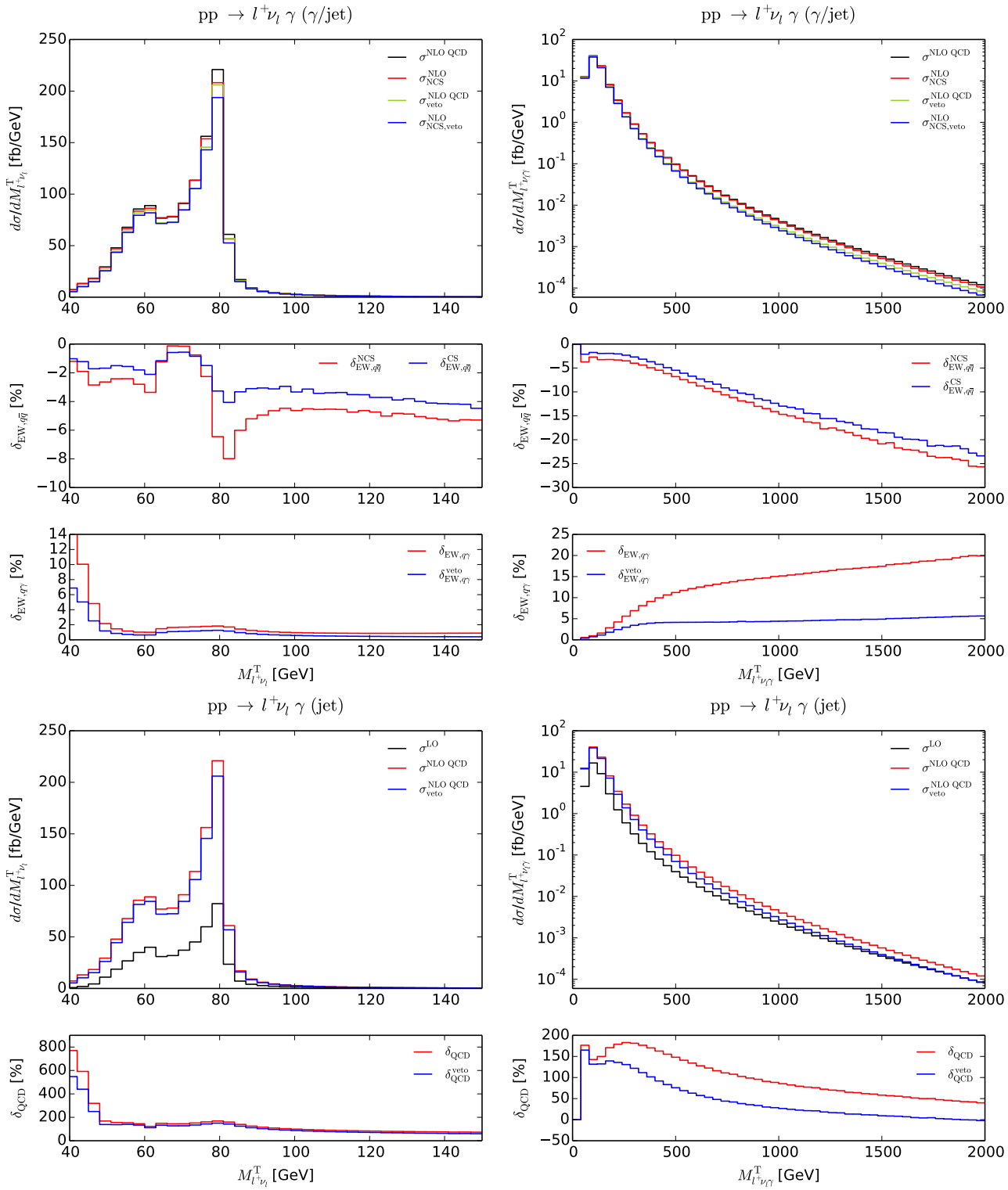

Figure 4.2: Distribution in the transverse mass $M_{\mathrm{T},l^+\nu}$ of the charged lepton and neutrino pair (left) and distribution in the transverse three-body mass $M_{\mathrm{T},l^+\nu\gamma}$ of the charged lepton, the neutrino, and the hardest photon (right), including EW (top) and QCD corrections (bottom). For all corrections absolute (upper box) and relative corrections (lower boxes) are shown.

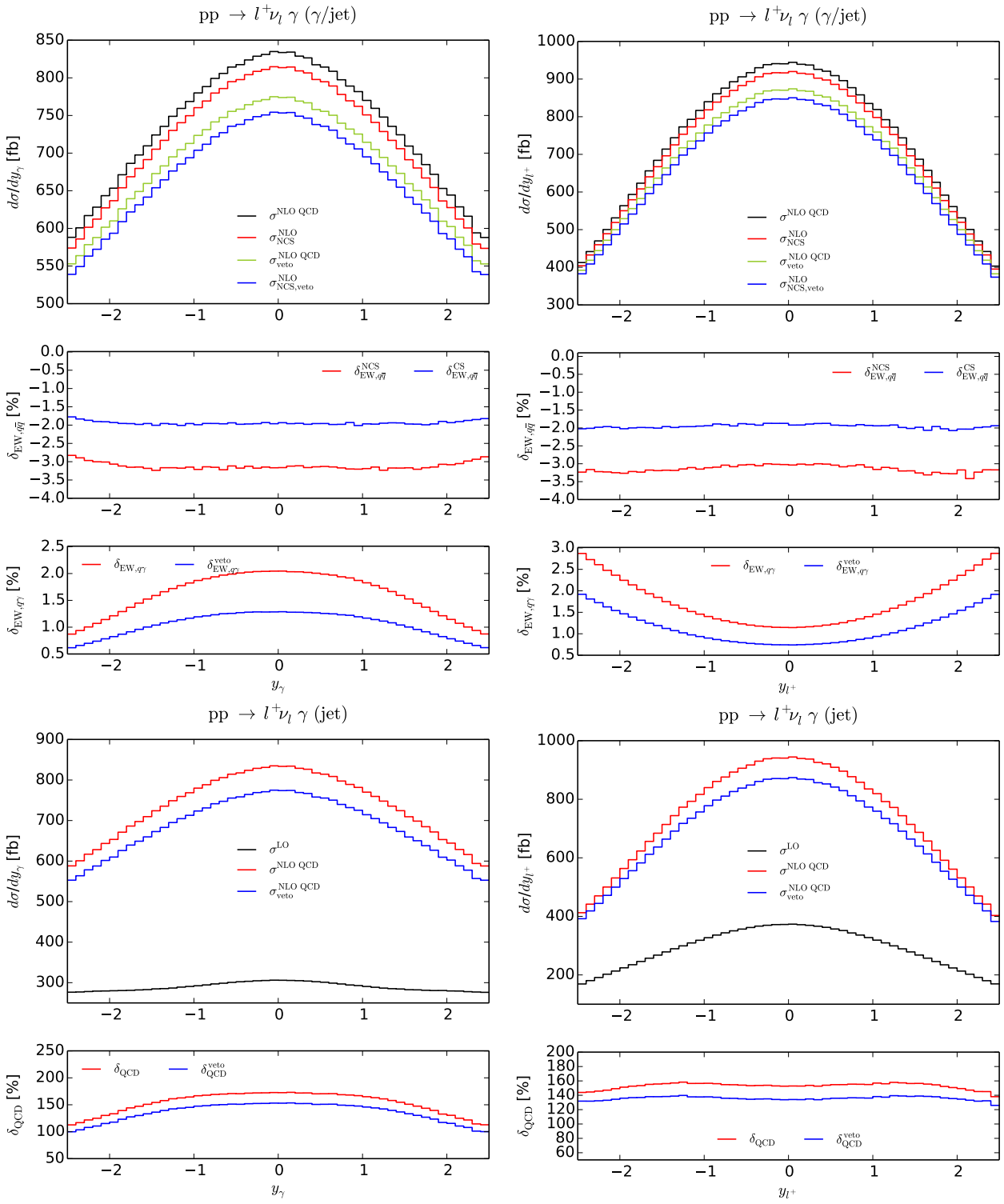

Figure 4.3: Distributions in the rapidity y_γ of the photon (left) and the rapidity y_{l^+} of the charged lepton (right), including EW (top) and QCD corrections (bottom). For all corrections absolute (upper box) and relative corrections (lower boxes) are shown.

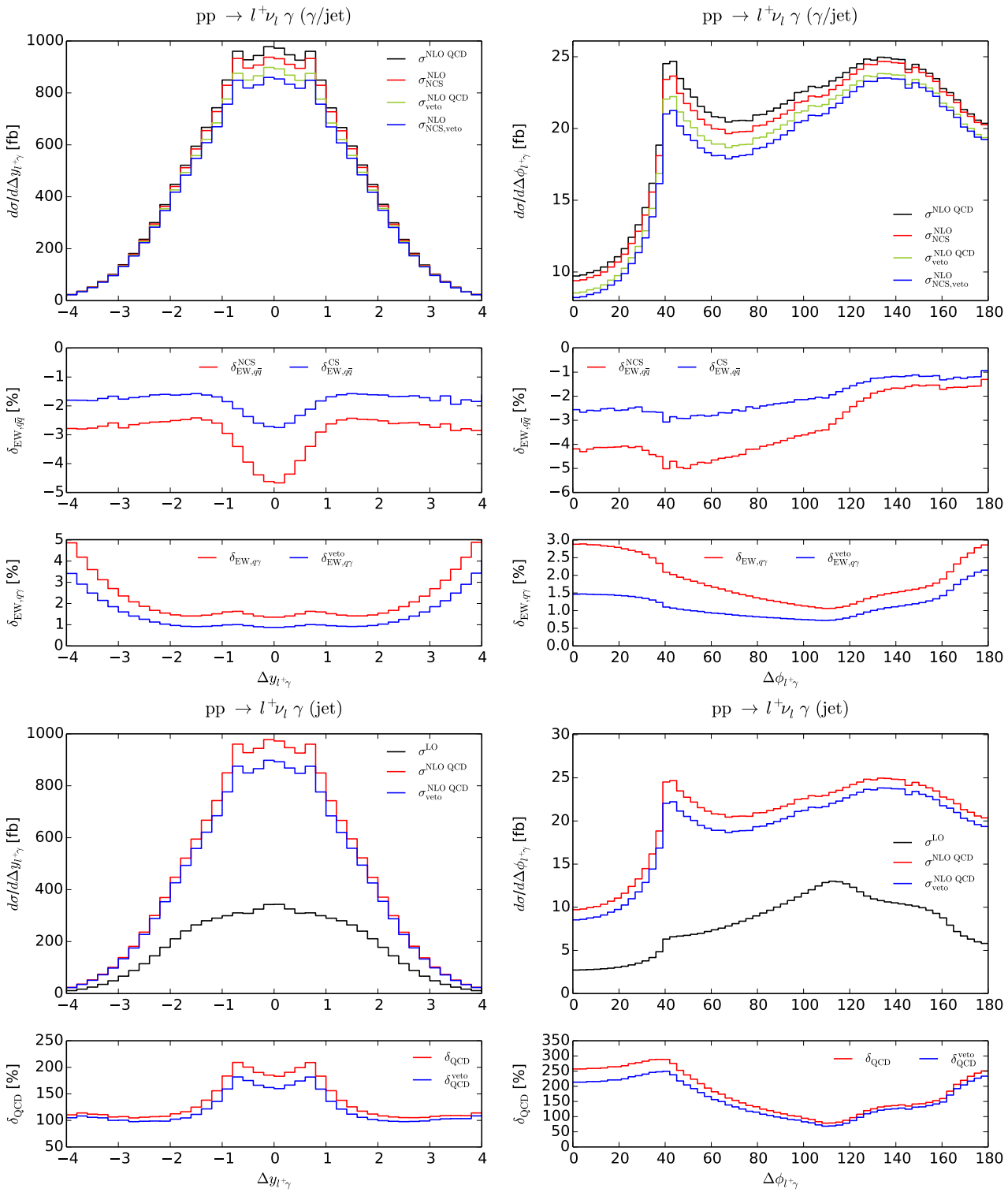

Figure 4.4: Distributions in the rapidity difference $\Delta y_{l^+\gamma}$ (left) and the azimuthal-angle difference $\Delta\phi_{l^+\gamma}$ (right) of the charged lepton and the photon, including EW (top) and QCD corrections (bottom). For all corrections absolute (upper box) and relative corrections (lower boxes) are shown.

$pp \to l^- \bar{\nu}_l \gamma + X$			
$\sqrt{s}$/ TeV	7	8	14
σ^{LO}/ fb	620.00(10)	707.50(12)	1200.00(21)
$\delta^{NCS}_{EW,q\bar{q}}$/%	−3.01	−3.01	−3.01
$\delta^{CS}_{EW,q\bar{q}}$/%	−1.85	−1.85	−1.86
$\delta^{frag}_{EW,q\gamma}$/%	1.34	1.39	1.56
$\delta^{veto,\,frag}_{EW,q\gamma}$/%	0.98	1.00	1.06
$\delta^{Frix}_{EW,q\gamma}$/%	1.35	1.40	1.57
$\delta^{veto,\,Frix}_{EW,q\gamma}$/%	1.00	1.02	1.07
δ^{frag}_{QCD}/%	139.80(14)	145.70(9)	167.00(11)
$\delta^{veto,\,frag}_{QCD}$/%	130.90(14)	135.50(9)	150.40(11)
δ^{Frix}_{QCD}/%	143.30(14)	149.30(9)	171.10(10)
$\delta^{veto,\,Frix}_{QCD}$/%	134.40(14)	139.00(9)	154.50(10)

Table 4.2: Integrated cross sections and relative corrections for $W^-\gamma$ production at different LHC energies. The EW corrections to the quark–antiquark annihilation channels are provided with (CS) and without (NCS) lepton–photon recombination. EW corrections from the photon-induced channels and QCD corrections are shown with a jet veto (veto) as well as without a jet veto using democratic clustering and fragmentation function (frag) or the Frixione isolation criterion (Frix) to separate photons and jets. The numbers in parentheses denote the integration error in the last digits. This error is negligible for the relative EW corrections at the given accuracy.

of the distributions at the level of a few per cent, whereas the QCD corrections cause large shape distortions and reach 200% in the $\Delta y_{l^+\gamma}$ and 300% in the $\Delta\phi_{l^+\gamma}$ distribution. The shape distortion in the $\Delta y_{l^+\gamma}$ distribution originates essentially from the gluon-induced corrections, which do not have a radiation zero. Especially in the rapidity-difference distribution, effects of anomalous couplings are expected to be visible as pointed out in Ref. [33]. Similarly to the rapidity distributions discussed before, the EW corrections are overwhelmed by QCD effects and the corresponding uncertainties here.

4.5 Results for p p $\to l^-\ \bar{\nu}_l\ \gamma\ + X$

4.5.1 Results on total cross section

Besides the $W^+\gamma$ production with the final state $l^+\nu_l\gamma$, the charge-conjugate process of $W^-\gamma$ production with the final state $l^-\bar{\nu}_l\gamma$ is also accessible at the LHC. In Table 4.2 we present the LO cross sections σ^{LO} for different pp centre-of-mass energies $\sqrt{s}$ for the charge-conjugate process of $W^-\gamma$ production. We use again the definitions of relative corrections δ from Eq. (4.4). Due to the different PDF factors the LO cross section for $W^-\gamma$ production is smaller than for $W^+\gamma$ production. The results on relative corrections look very similar to the ones for $W^+\gamma$ production, discussed in Section 4.4.1.

4.5.2 Results on transverse-momentum and transverse-mass distributions

In this section we discuss qualitative similarities and differences in the distributions for the two processes $W^+ + \gamma$ and $W^- + \gamma$ production. In Fig. 4.5 we present the p_T distribution of the charged lepton and the transverse-mass distribution of the W boson. In this plots we show results for $W^+ + \gamma$ and $W^- + \gamma$ production together and we focus on the NCS case without a jet veto.

The $p_{T,l}$ distribution (Fig. 4.5, left) shows characteristic differences between the two processes. While the shape of relative electroweak corrections for the quark–antiquark-induced channels is almost identical for both $W^+\gamma$ and $W^-\gamma$ production, for photon-induced corrections the shape of the relative corrections clearly differs. Whereas for $W^+\gamma$ production these corrections increase slightly from 20% at 200 GeV to 50% at 1500 GeV the growth for $W^-\gamma$ is much larger and reaches 120% at 1500 GeV. Also for the QCD corrections differences are visible. In the $W^+\gamma$ case the relative corrections show a maximum of about 500% around 100 GeV and decrease almost to zero at large transverse momenta. For $W^-\gamma$ on the other hand, we find a maximum of approximately 1000% near 200 GeV and a decline to 200% at 1500 GeV. While the shapes of the relative QCD corrections from the quark–antiquark-induced contributions for $W^+\gamma$ and $W^-\gamma$ look very similar those from gluon-induced contributions differ significantly. This difference can be understood as follows: For large $p_{T,l}$ the cross section receives a large contribution from the partonic processes $qg \to q'W\gamma$. As pointed out in Ref. [103], in the related process $qg \to q'W$ the W^+ and W^- bosons are primarily polarized left-handed with an increase of this polarization for higher $p_{T,W}$. The W^+ boson emits the left-handed neutrino preferentially parallel to its flight direction and the right-handed positron antiparallel. On average, this results in a larger transverse momentum of the neutrino and a smaller transverse momentum of the positron leading to an enhancement in the $p_{T,miss}$ distribution of the neutrino and a reduction in the p_T distribution of the positron. For the W^- boson the situation is vice versa. A left-handed electron is emitted forward and a right-handed anti-neutrino backward with respect to the W^- momentum so that the p_T distribution of the electron is enhanced and the $p_{T,miss}$ distribution is reduced (for a detailed explanation see Refs. [103, 104]). This behaviour also appears in the large photon- and gluon-induced corrections to $W + \gamma$ production and causes the observed differences between $W^+ + \gamma$ and $W^- + \gamma$ production.

In the distribution of the transverse mass of the W boson (Fig. 4.5, right) the situation is different. In the quark–antiquark-induced relative electroweak corrections there is no qualitative difference between the processes $W^+\gamma$ and $W^-\gamma$ visible. For the QCD and the photon-induced corrections the only difference between $W^+\gamma$ and $W^-\gamma$ is in the size of the maximum near 40 GeV. Apart from this, the shapes of the relative photon-induced and QCD corrections are quite similar for the two different processes.

We have also considered other differential distributions, but show only the two distributions with the largest and smallest discrepancies between the two processes in Fig. 4.5. The differences are mostly small where the cross sections are sizeable. Differences of the same size as for the $p_{T,l}$ distribution are, however, also found for the $p_{T,\gamma}$ distribution.

Figs. C.1– C.4 list further distributions for $W^- + \gamma$ production including the CS case and the corrections with the application of jet veto. The comparison between $W^+ + \gamma$ and $W^- + \gamma$ production for other observables can be found in Figs. C.5– C.7.

4.6 Dilepton + photon production: $p\ p \to l^+\ l^-\ \gamma + X$

In Table 4.3 we present the LO cross sections σ^{LO} for different pp centre-of-mass energies $\sqrt{s}$ and different types of relative corrections δ defined in (4.4) for $pp \to Z/\gamma^* + \gamma \to l^+l^- + \gamma + X$.

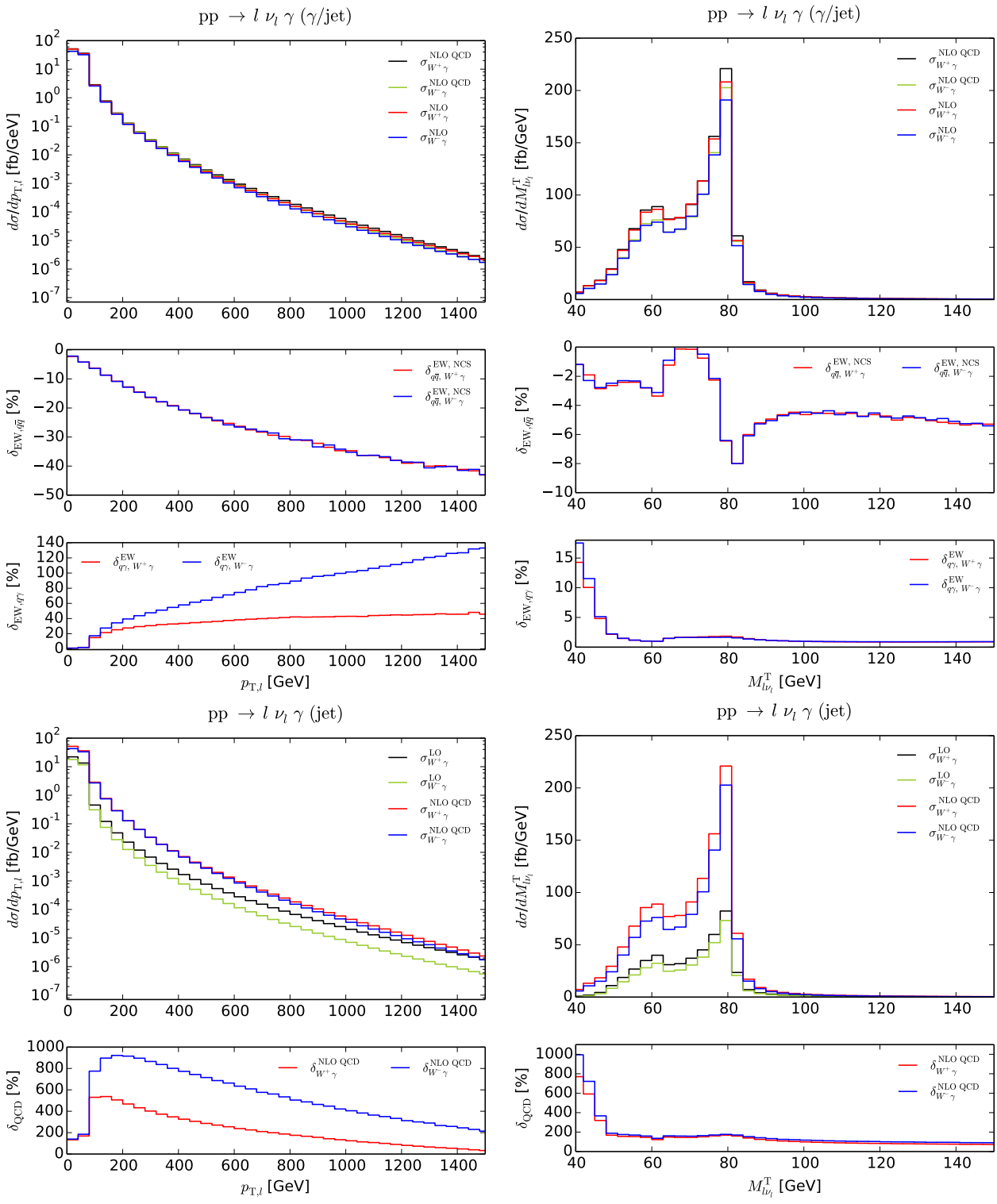

Figure 4.5: Comparison of $W^+\gamma$ and $W^-\gamma$ production in the transverse-momentum distribution of the charged lepton (left) and the transverse-mass distribution of the charged lepton and the neutrino (right), including EW (top) and QCD corrections (bottom). For all corrections absolute (upper box) and relative corrections (lower boxes) are shown.

$pp \to l^- l^+ \gamma + X$			
$\sqrt{s}$/ TeV	7	8	14
σ^{LO}/ fb	728.90(7)	818.40(8)	1317.00(14)
$\delta_{\gamma\gamma}$/%	0.27	0.26	0.22
$\delta^{NCS}_{EW,q\bar{q}}$/%	−5.50	−5.49(7)	−5.43
$\delta^{CS}_{EW,q\bar{q}}$/%	−3.46	−3.46(7)	−3.43
$\delta^{frag}_{EW,q\gamma}$/%	0.03	0.03	0.04
$\delta^{veto,\,frag}_{EW,q\gamma}$/%	0.01	0.02	0.02
$\delta^{Frix}_{EW,q\gamma}$/%	0.05	0.05	0.06
$\delta^{veto,\,Frix}_{EW,q\gamma}$/%	0.04	0.04	0.04
δ^{frag}_{QCD}/%	61.47(5)	62.78(5)	67.91(7)
$\delta^{veto,\,frag}_{QCD}$/%	58.67(5)	59.63(5)	63.17(7)
δ^{Frix}_{QCD}/%	60.57(5)	61.92(5)	67.18(7)
$\delta^{veto,\,Frix}_{QCD}$/%	57.77(5)	58.76(5)	62.44(7)

Table 4.3: Integrated cross sections and relative corrections for $pp \to l^+l^-\gamma + X$ at different LHC energies. The EW corrections to the quark–antiquark annihilation channels are provided with (CS) and without (NCS) lepton–photon recombination. Contributions from the photon-induced channels and QCD corrections are shown with a jet veto (veto) as well as without a jet veto using democratic clustering and fragmentation function (frag) or the Frixione isolation criterion (Frix) to separate photons and jets. The numbers in parentheses denote the integration errors in the last digits. This error is omitted if it is negligible at the given accuracy.

For the EW corrections resulting from the quark–antiquark-induced channels we show results for the CS and NCS scenarios. Results for the EW corrections originating from photon-induced channels and for the QCD corrections are listed with and without a jet veto. Furthermore, we present results obtained by applying democratic clustering in combination with a quark-to-photon fragmentation function and the Frixione isolation scheme indicated by "frag" and "Frix", respectively. The different relative corrections are not particularly sensitive to the collider energy. The largest variation ($\sim 60-68\%$) occurs in the QCD corrections. A jet veto allowing a maximal jet transverse momentum of 100 GeV does not diminish the QCD corrections considerably, since energy scales dominating the integrated cross section are much lower for our setup, which allows for photons (leptons) down to transverse-momentum values of 15 (25) GeV. The gluon-induced channels (not separately shown) contribute only about a tenth to the QCD corrections at an energy of 14 TeV and even less at lower collider energies. The results obtained with the fragmentation function and the Frixione isolation scheme differ by $0.5-1\%$ for the QCD corrections. The EW corrections to the quark–antiquark channels are about -3.4% and -5.5% for the CS and the NCS case, respectively. The quark–photon-induced corrections contribute less than 0.06% with and without a jet veto and, thus, are phenomenologically negligible. The photon–photon-induced channel contributes with $\sim 0.25\%$.

In summary, the quark–antiquark-induced EW corrections to the integrated cross sections are small compared to the NLO QCD corrections. Nevertheless, they might become relevant in future analyses, since they are of the order of several percent, i.e. larger than the residual scale uncertainty of the NNLO QCD corrections. The photon-induced EW corrections are at the per-mille level and not significant for experimental cross-section measurements. However, larger effects appear in differential distributions, as demonstrated in the following. Besides the

observables which will be discussed in detail in the following further distributions are listed in Figs. D.1– D.3.

4.6.1 Results on transverse-momentum distributions

In the following we present differential distributions including QCD and EW corrections to $pp \to Z/\gamma^* + \gamma \to l^+l^- + \gamma + X$ for a pp centre-of-mass energy of 14 TeV. For each distribution the relative EW corrections of the $q\bar{q}$, $q\gamma$, and $\gamma\gamma$ channels as well as the QCD corrections with and without a jet veto are shown. Since the difference between Frixione isolation and the quark-to-photon fragmentation function is of the order of 1% for the integrated cross section and distributions, and therefore not very significant, we only show results obtained with the quark-to-photon

In Fig. 4.6 we show results on the transverse-momentum distributions of the hardest photon (within cuts) and of the Z boson (defined in Eq. (4.9)). Both distributions receive large QCD corrections in the region of high transverse momenta. This is due to the fact that at NLO QCD new channels appear ($qg \to l^+l^-\gamma q$) causing large corrections, especially in the high-p_T tails. However, these large corrections originate from events with hard jets. These events should preferably be considered as part of Z + jet rather than Z + γ production. Therefore we additionally show distributions for the case of a jet veto discarding events with $p_{T,\text{jet}} > 100\,\text{GeV}$. The jet veto suppresses the large QCD corrections at high transverse momenta. The p_T distributions of the photon and the Z boson receive large negative EW corrections, which predominantly originate from so-called EW Sudakov logarithms. In case of the $p_{T,\gamma}$ distribution the CS and the NCS cases hardly differ, since the recombination of the second photon and a collinear lepton hardly influences the transverse momentum of the hardest photon. In contrast, the CS and the NCS cases differ in the $p_{T,Z}$ distribution. This is due to the fact that the transverse momentum of the Z boson is reconstructed from the momenta of the charged leptons which are sensitive to the recombination with a collinearly radiated photon. The quark–photon-induced corrections are below 10% in both distributions and almost vanish in case of a jet veto. The photon–photon-induced corrections grow up to 4% at $p_{T,Z} = 1\,\text{TeV}$. They are not affected by the jet veto, since there is no jet in the final state. In summary, the EW corrections are much smaller than the QCD corrections if no jet veto is applied, but sizeable. In case of a jet veto they even become the leading corrections in the high-transverse-momentum tails.

The transverse-momentum distributions of the two charged leptons are shown in Fig. 4.7. The QCD corrections turn out to be of the order of 150% at 100 GeV and decrease to 50% at 1 TeV if no jet veto is applied. In case of a jet veto the corrections are still large (100%) in the low p_T-range and drop to -50% at 1 TeV. The transverse-momentum distribution of each charged lepton receives large negative weak corrections originating from the Sudakov logarithms, reaching -15% at 1 TeV. The difference between the CS and the NCS EW corrections is roughly 6%. The collinear radiation of photons off FS charged leptons shifts the lepton transverse momentum to smaller values, causing negative corrections. Recombining the charged lepton with the collinear photon partly compensates this effect, which is why the CS corrections are smaller. The quark–photon-induced corrections are below 5% and almost vanish in case of a jet veto. The photon–photon-induced correction grows up to more than 10% at 1 TeV. Note, however, that at large Bjorken-x the photon-PDF carries large uncertainties of the order of 100%. We see that in the high-p_T tail the EW corrections are of the same order of magnitude as the QCD corrections with and without a jet veto. The transverse-momentum distributions of the two charged leptons and the corresponding corrections do not differ significantly.

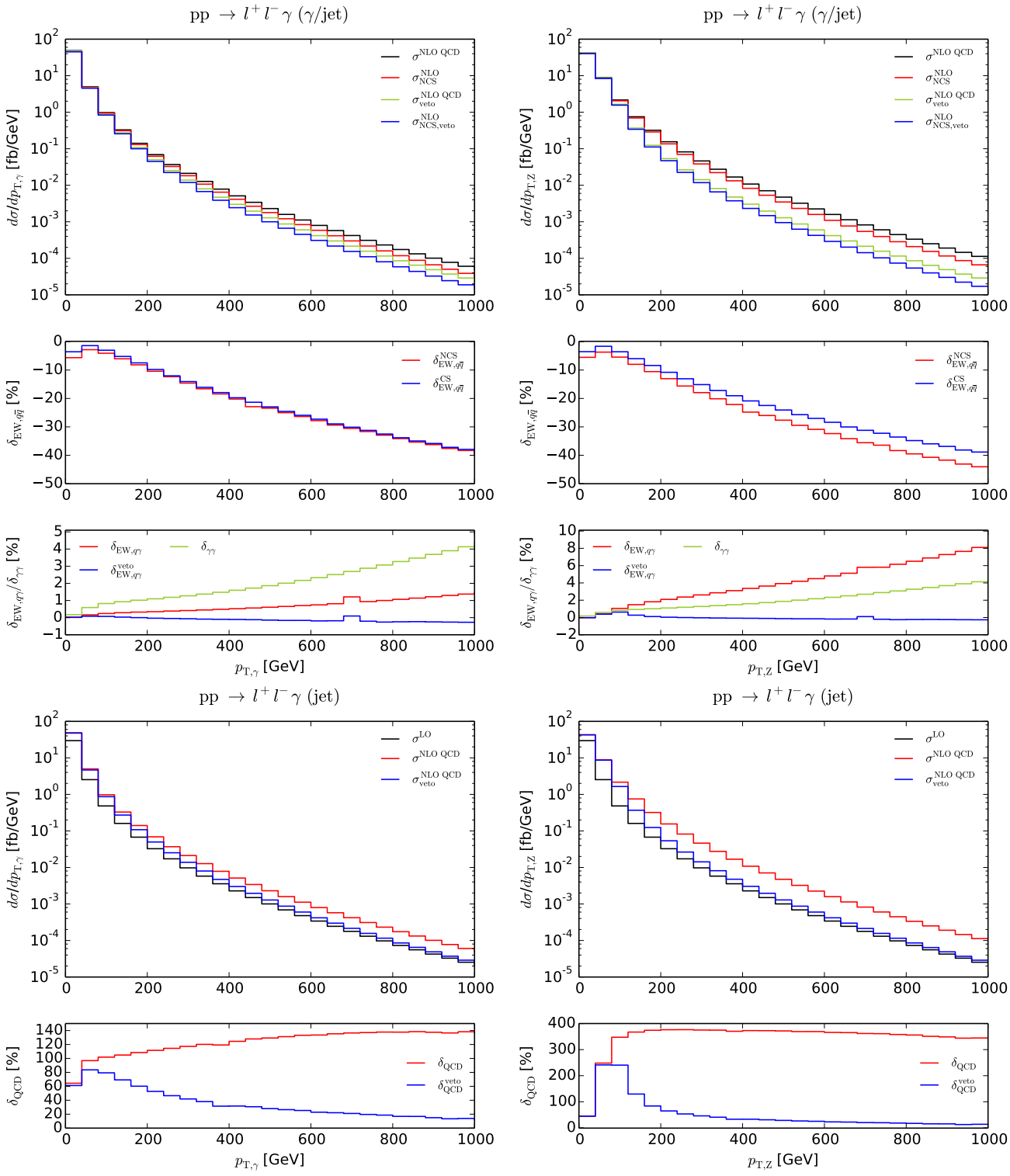

Figure 4.6: Distributions in the transverse momentum p_T of the hardest photon (left) and the Z boson (right), including EW (top) and QCD corrections (bottom). The upper boxes show absolute predictions, the lower ones relative corrections.

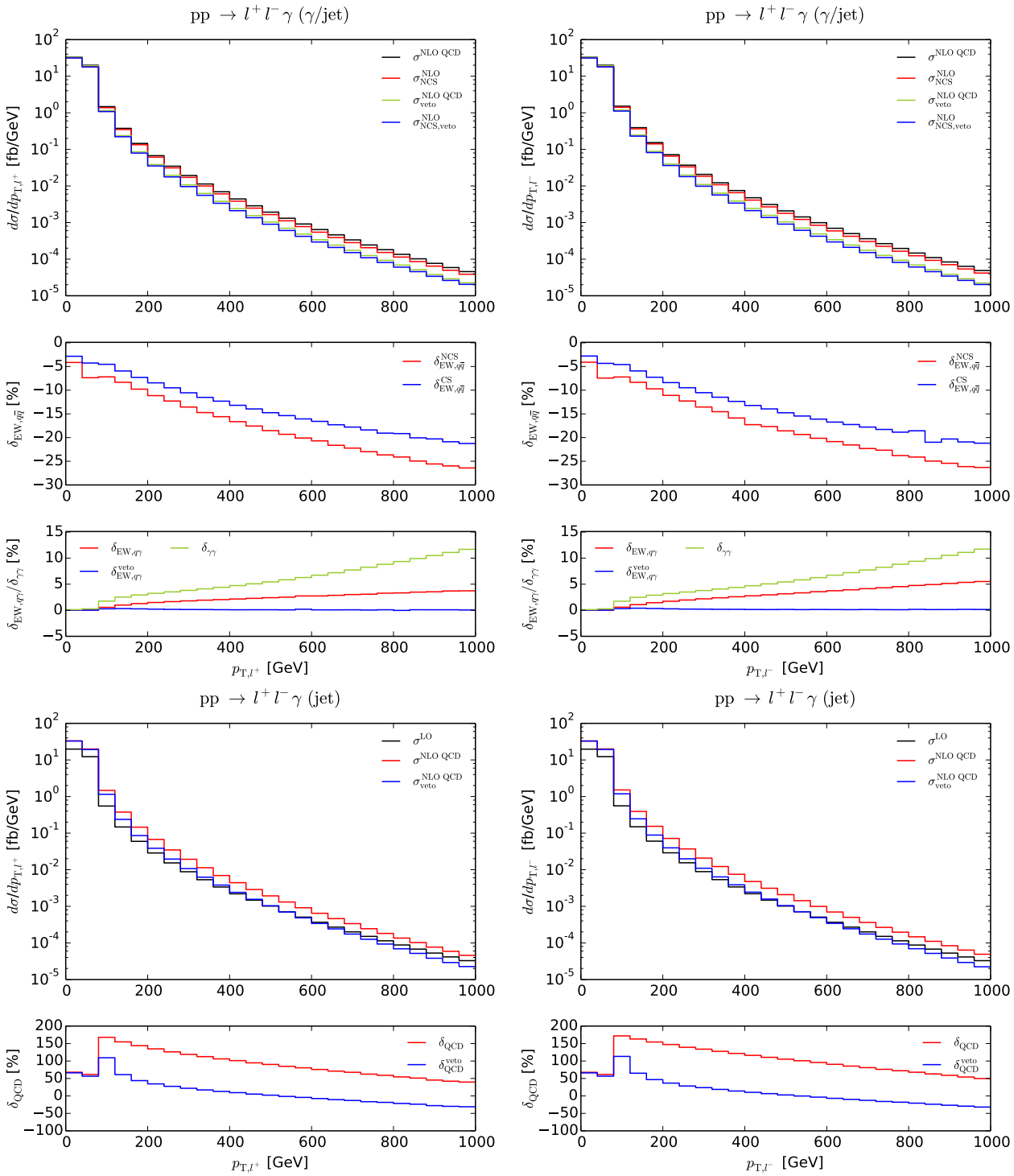

Figure 4.7: Distributions in the transverse momenta $p_{\mathrm{T},l^\pm}$ of the two charged leptons, including EW (top) and QCD corrections (bottom). The upper boxes show absolute predictions, the lower ones relative corrections.

4.6.2 Results on invariant-mass distributions

The invariant mass of the Z boson, $M_{l^+l^-}$, is defined in (4.8), and the invariant three-body mass of the Z-decay products and the photon is defined by

$$M_{l^+l^-\gamma} = \sqrt{(p_{l^+} + p_{l^-} + p_\gamma)^2}\,, \tag{4.15}$$

where p_{l^+}, p_{l^-}, and p_γ are the four-vectors of the charged leptons and the hardest photon, respectively. We always take the momentum of the hardest photon if there are two photons. The corresponding distributions are shown in Fig. 4.8.

The invariant-mass distribution of the two charged leptons exhibits two peaks already at LO. The larger one corresponds to the Z resonance originating from the propagator that is resonant in the invariant mass of the two charged leptons $M_{l^+l^-}$ at $M_{l^+l^-} = M_\mathrm{Z}$. The smaller one comes from the resonance in the invariant three-body mass $M_{l^+l^-\gamma}$, where the photon is radiated by one of the FS charged leptons leading to a shift of the peak. The location of the smaller peak mainly depends on the cut on the transverse momentum of the photon. With decreasing values of the cut on $p_{\mathrm{T},\gamma}$ the peak becomes less pronounced and moves towards the larger peak until they fuse. The QCD corrections are the leading corrections in this distribution. They are particularly large at low invariant masses and below the resonance with and without a jet veto. This is to some extent a result of our basic cuts, which allow invariant masses $M_{l^+l^-}$ down to 40 GeV, but at the same time demand transverse momenta $p_{\mathrm{T},l^\pm} > 25\,\mathrm{GeV}$. At LO, this leads to a strong suppression of the cross section at low $M_{l^+l^-}$, but at NLO QCD a jet recoil (with intermediate $p_{\mathrm{T,jet}} < 100\,\mathrm{GeV}$) in the real QCD corrections can lift such events over the cuts on $p_{\mathrm{T},l^\pm}$, leading to particularly large positive QCD corrections there. In the resonance region the EW corrections coming from the $q\overline{q}$ channel reach 20% in the CS and 40% in the NCS cases. Without photon recombination the shape distortion of the Z resonance is larger, since more events appear where the photon carries away energy and shifts events from higher to lower energies. The quark–photon-induced EW corrections are almost zero for low invariant masses and reach 1% at 300 GeV. In case of a jet veto they are well below one percent everywhere. The photon–photon-induced corrections are also tiny for invariant masses below 100 GeV, but grow up to 5% at 300 GeV.

Focusing on the invariant three-body mass we see that the QCD corrections are the dominating contribution in the region of low invariant masses, but decrease with and without a jet veto to 50% and 0%, respectively, for $M_{l^+l^-\gamma} = 2\,\mathrm{TeV}$. In this region, the $M_{l^+l^-\gamma}$ distribution receives large negative corrections between -23% and -28% from the EW corrections for the CS and the NCS case, respectively. The quark–photon-induced EW corrections are of the order of 1–2% and practically vanish in case of a jet veto, while the photon–photon-induced corrections reach 10% at 2 TeV. At high invariant mass the EW corrections are of the same order of magnitude as the QCD corrections and become the leading corrections in case of a jet veto.

4.6.3 Results on rapidity and angular distributions

In the following we present some rapidity and angular distributions along with the corresponding NLO corrections. As for the integrated cross section the QCD corrections yield typically the largest contributions and in most cases a jet veto has no sizeable impact. We only show the most interesting distributions in this section. Further distributions are listed in Appendix D.

Although the distributions in the rapidity differences $\Delta y_{\mathrm{Z}\gamma}$ and $\Delta y_{l^+\gamma}$ shown in Fig. 4.9 are different in their absolute values, the relative QCD and EW corrections are very similar in the two cases.

The QCD corrections are about 50% at zero rapidity distance and grow to 110% at $|\Delta y| = 4$. The quark–antiquark-induced EW corrections amount to roughly -3% in the CS case and vary

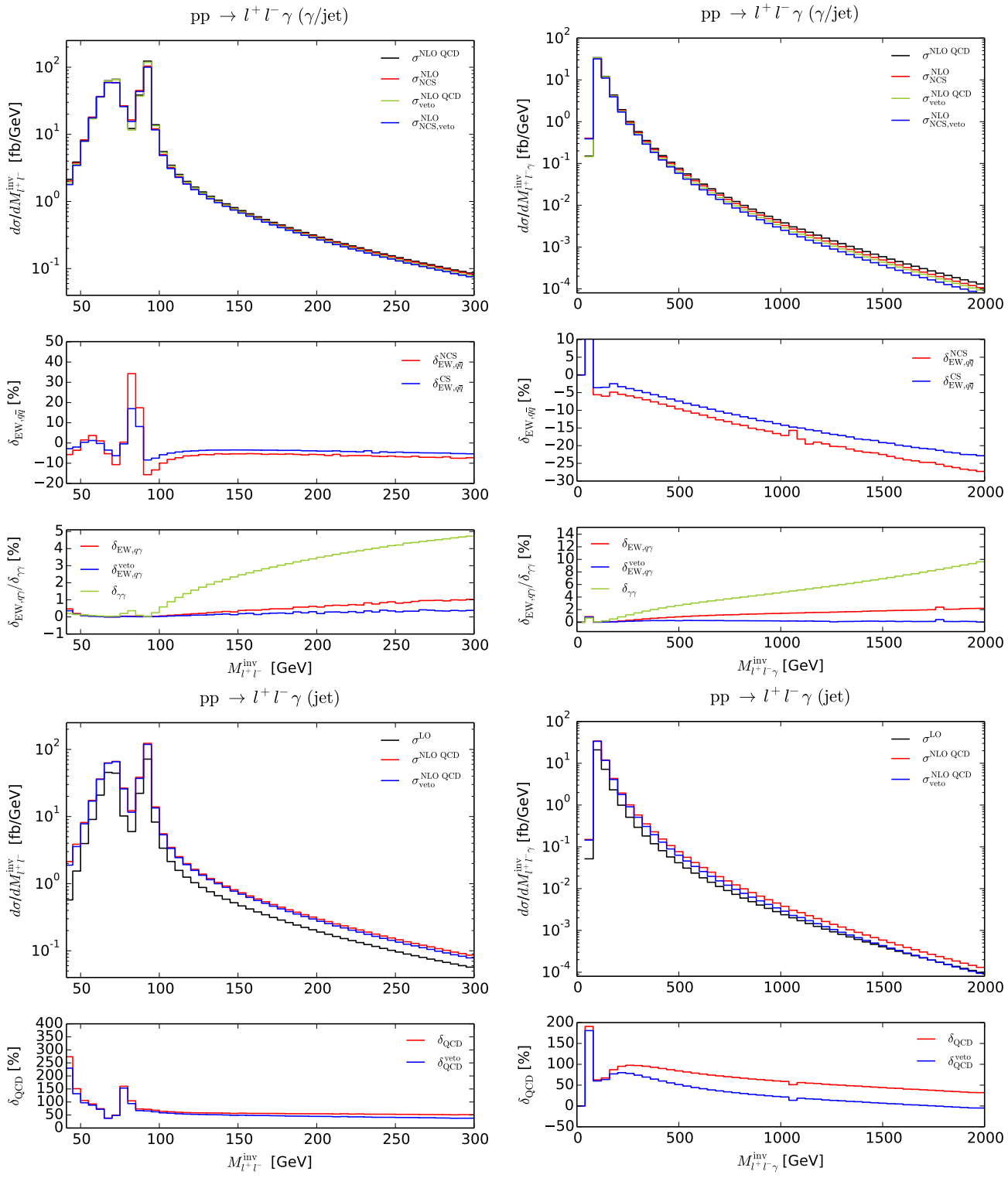

Figure 4.8: Distribution in the invariant mass $M_{l^+l^-}$ of the charged leptons (left) and distribution in the invariant three-body mass $M_{l^+l^-\gamma}$ of the charged leptons and the hardest photon (right), including EW (top) and QCD corrections (bottom). The upper boxes show absolute predictions, the lower ones relative corrections.

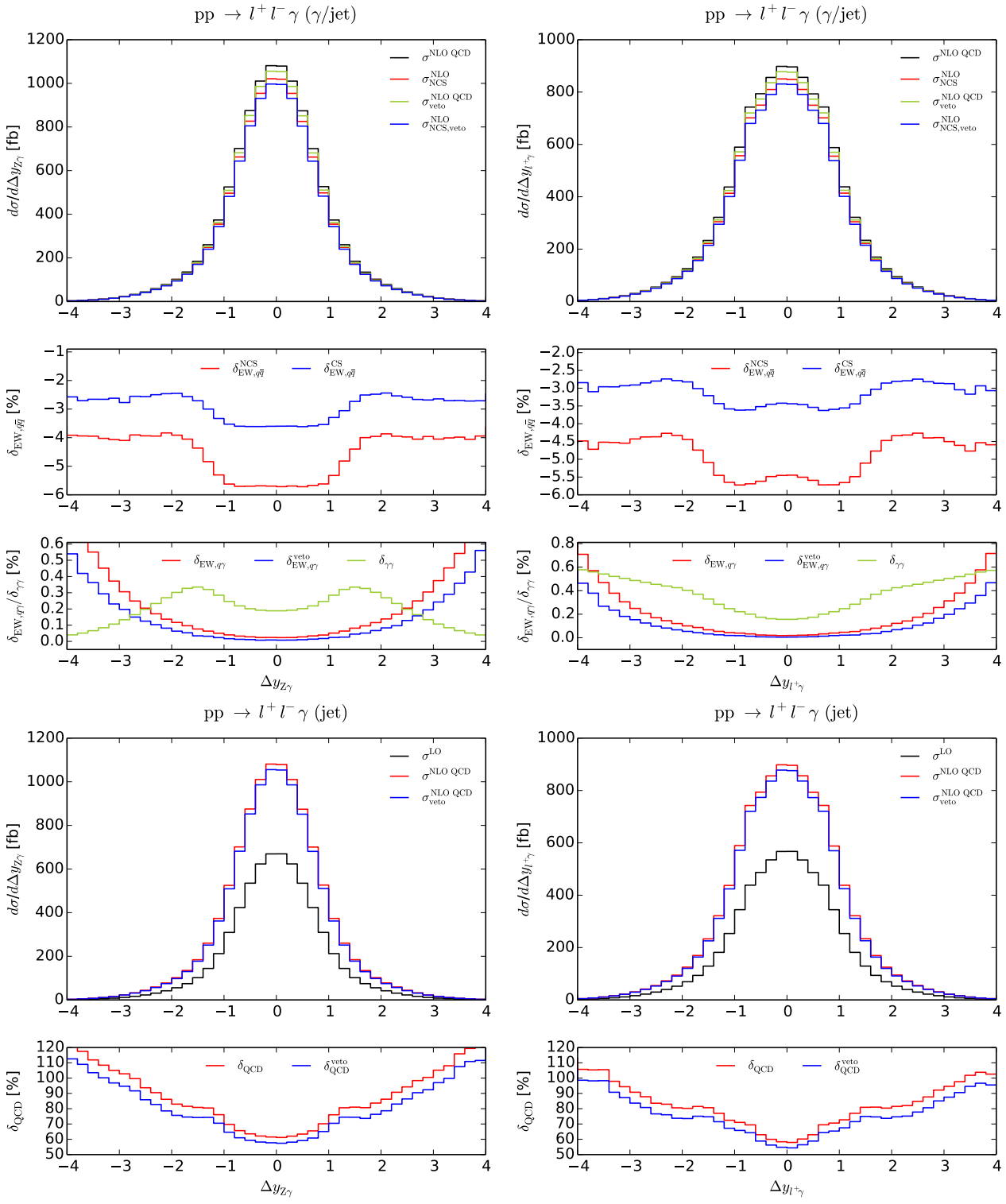

Figure 4.9: Distributions in the rapidity difference $\Delta y_{Z\gamma}$ between the hardest photon and the Z boson (left), and the rapidity difference $\Delta y_{l^+\gamma}$ between the charged lepton and the hardest photon (right), including EW (top) and QCD corrections (bottom). The upper boxes show absolute predictions, the lower ones relative corrections.

between -4% and -6% in the NCS case. The photon-induced corrections stay below 1% and are phenomenologically unimportant.

Next we focus on the rapidity difference and the azimuthal-angular difference between the charged leptons shown in Fig. 4.10. Starting with the rapidity difference we see that the EW corrections to the $q\bar{q}$ channel have a minimum at zero rapidity difference and increase up to -12% and -14% at $|\Delta y_{l^+l^-}| = 4$ in the CS and the NCS case, respectively. The corrections from the $q\gamma$ channels are below 4% and 2% with and without a jet veto, respectively. The photon–photon-induced corrections are below 5% for $|\Delta y_{l^+l^-}| < 2$ and increase steeply to 30% for $|\Delta y_{l^+l^-}| \sim 4$. However, in this region the cross section is very small.

The azimuthal-angular difference between the charged leptons has a peak around 160°. This peak is caused by the cut on the transverse momentum of the photon which eliminates events with back-to-back leptons in the transverse plane. Increasing this cut shifts the peak to smaller azimuthal angles. The NLO QCD corrections cause a very significant broadening of the peak, because jet recoil effects strongly influence the angle between the leptons when the decaying Z bosons receives a boost. The effect is strongest in the limit where the leptons are nearly collinear, a region that is rarely populated at LO, but receives large contributions from hard jet emission where the jet recoil and the boost of the Z boson are strongest. This also explains the sensitivity of this region to the jet veto. The EW corrections from the $q\bar{q}$ channels are of the order of -6% and -7% in the CS and the NCS cases, respectively, in the region of small angle differences and decrease at larger ones. The photon-induced corrections lie below about 1% and are phenomenologically unimportant.

In summary, in angular and rapidity distributions the EW corrections are suppressed with respect to the QCD corrections.

4.7 Invisible $\mathrm{Z} + \gamma$ production: $\mathrm{p\ p} \to \bar{\nu}\ \nu\ \gamma + X$

4.7.1 Results on total cross section

In Table 4.4 we present the LO cross sections σ^{LO} for different pp centre-of-mass energies $\sqrt{s}$ and different types of relative corrections δ defined in (4.4) for $\mathrm{pp} \to \mathrm{Z} + \gamma \to \bar{\nu}\nu + \gamma + X$.

Recall that we sum over all three lepton generations. Similar to the results in Table 4.3 we find that the relative corrections only marginally vary for the different collider energies. Here again the QCD corrections give the dominant contributions with $\sim 40{-}50\%$, but with 26% the amount of the gluon-induced channels is much larger than for $l^+l^-\gamma$ production. Owing to the neutral final state the dominant contribution inside the quark–antiquark-induced EW corrections results from pure weak corrections with -4.5% and the photonic corrections only contribute 0.3%. Again the quark–photon-induced corrections are phenomenologically negligible.

4.7.2 Results on transverse-momentum distributions

In the following we present differential distributions including QCD and EW corrections to $\mathrm{pp} \to \mathrm{Z} + \gamma \to \bar{\nu}\nu\gamma + X$ for a pp centre-of-mass energy of 14 TeV. In Fig. 4.11 we show distributions in the transverse-momentum of the photon and the missing transverse momentum. First we notice that the two distributions as well as the corresponding corrections are almost identical.

Since the photon neither couples to the Z boson nor to the neutrinos, the photon and the Z boson are always back to back in their centre-of-mass frame at LO. Corrections from the real radiation of jets or photons off the initial-state partons hardly distinguish between the produced Z boson or the hard photon, so that even the NLO corrections (both QCD and EW) almost

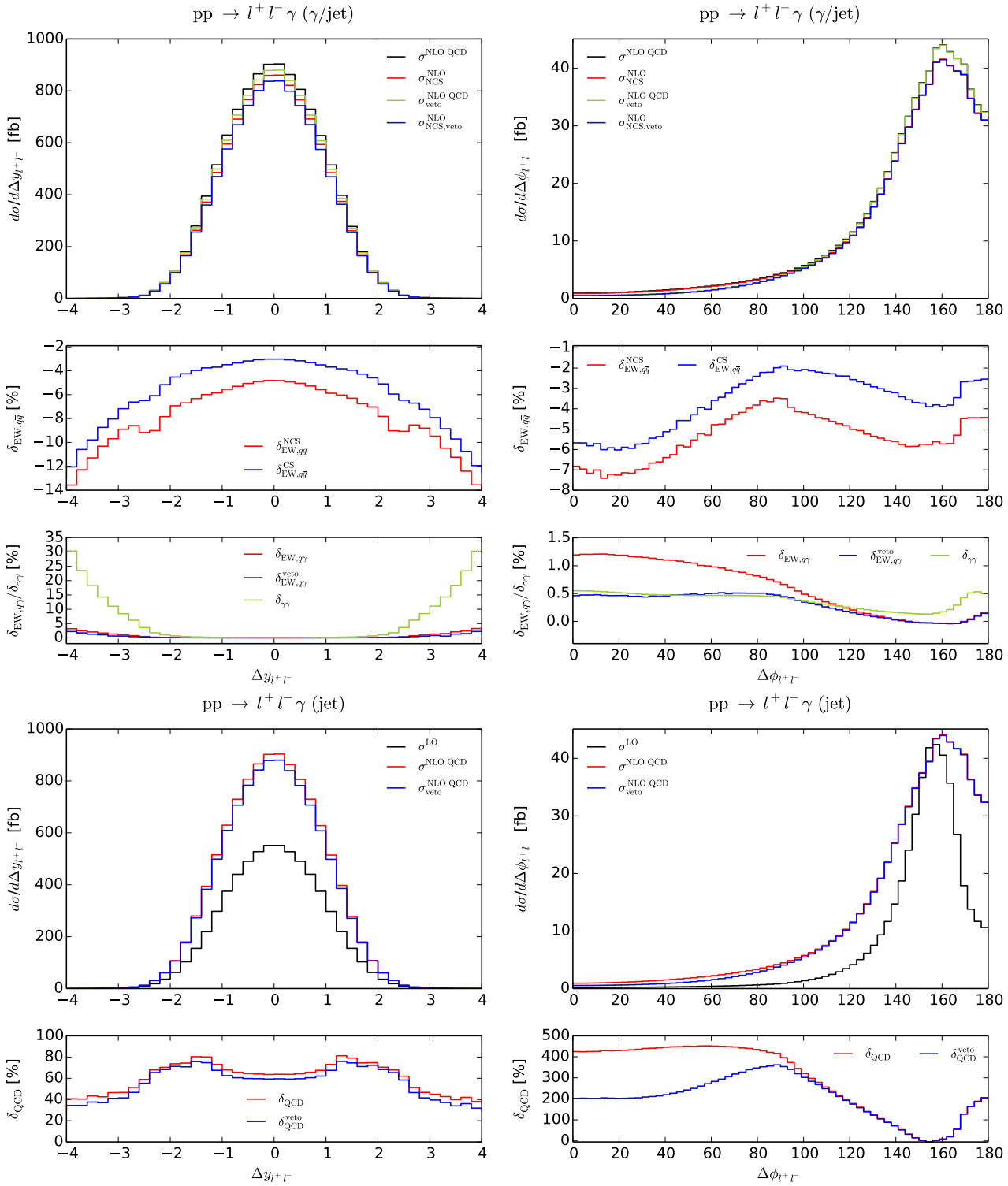

Figure 4.10: Distributions in the rapidity difference $\Delta y_{l^+l^-}$ (left) and the azimuthal-angle difference $\Delta\phi_{l^+l^-}$ (right) of the charged leptons, including EW (top) and QCD corrections (bottom). The upper boxes show absolute predictions, the lower ones relative corrections.

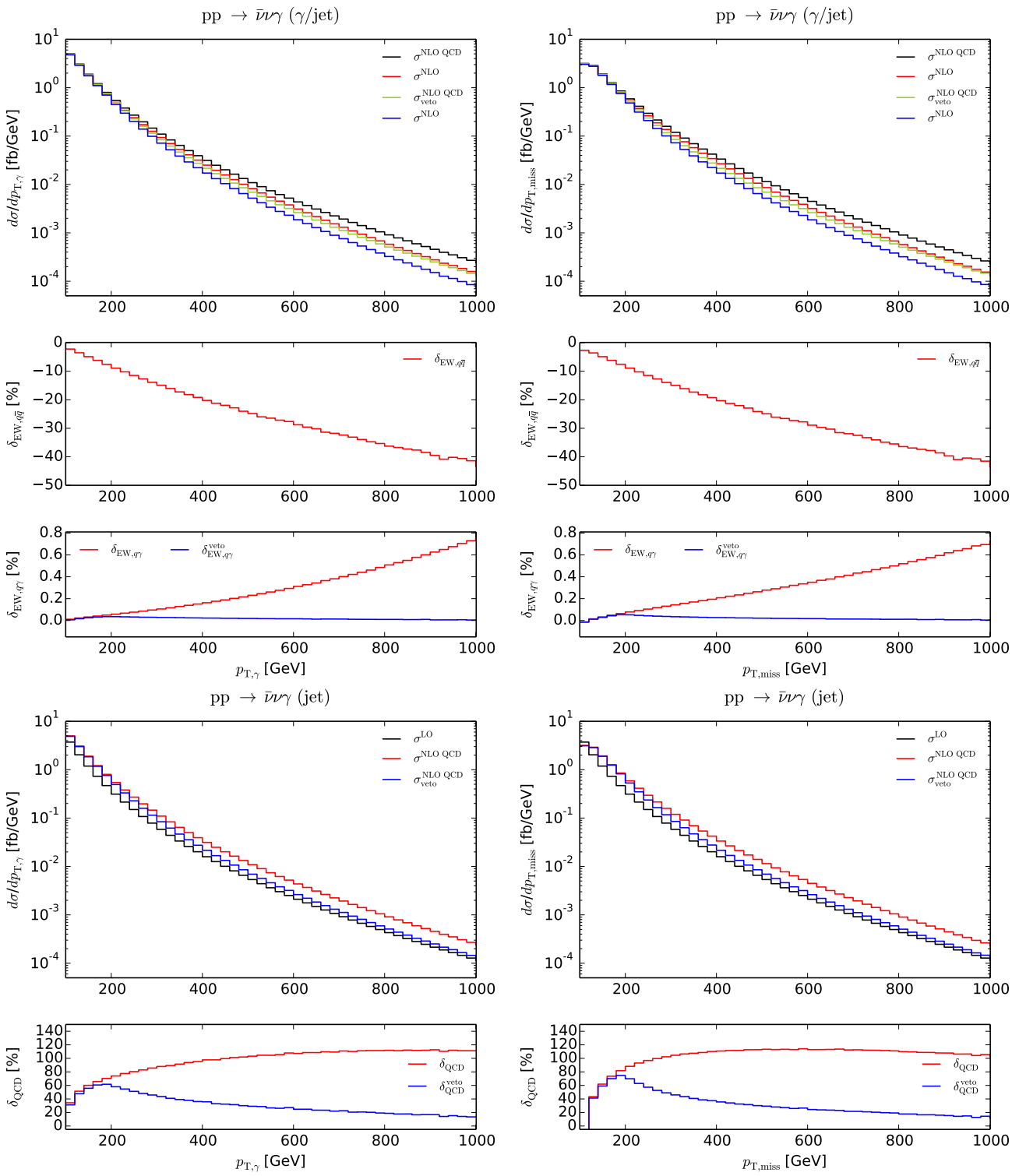

Figure 4.11: Distributions in the transverse momentum p_T of the photon (left) and the missing transverse momentum (right), including EW (top) and QCD corrections (bottom). The upper boxes show absolute predictions, the lower relative corrections.

$pp \to \bar{\nu}\nu\,\gamma + X$			
$\sqrt{s}$/ TeV	7	8	14
σ^{LO}/ fb	74.93(1)	91.03(1)	185.30(2)
$\delta_{EW,q\bar{q}}$/%	−4.15	−4.26	−4.68
$\delta^{frag}_{EW,q\gamma}$/%	0.03	0.03	0.03
$\delta^{veto,\,frag}_{EW,q\gamma}$/%	0.02	0.02	0.02
$\delta^{Frix}_{EW,q\gamma}$/%	0.03	0.03	0.03
$\delta^{veto,\,Frix}_{EW,q\gamma}$/%	0.02	0.02	0.02
δ^{frag}_{QCD}/%	46.24(3)	46.91(3)	51.46(4)
$\delta^{veto,\,frag}_{QCD}$/%	42.46(3)	42.52(3)	44.05(4)
δ^{Frix}_{QCD}/%	45.42(4)	46.08(3)	50.71(3)
$\delta^{veto,\,Frix}_{QCD}$/%	41.63(4)	41.69(3)	43.31(3)

Table 4.4: Integrated cross sections and relative corrections for $pp \to \bar{\nu}\nu\gamma + X$ at different LHC energies. Contributions from the photon-induced channels and QCD corrections are shown with a jet veto (veto) as well as without a jet veto using democratic clustering and fragmentation function (frag) or the Frixione isolation criterion (Frix) to separate photons and jets. The numbers in parentheses denote the integration error in the last digits. This error is omitted if it is negligible at the given accuracy.

coincide for the $p_{T,Z}$ (which is equivalent to $p_{T,miss}$) and $p_{T,\gamma}$ distributions. Furthermore the NLO corrections closely resemble the ones shown in Fig. 4.6 (left) for the $p_{T,\gamma}$ distribution for the $l^+l^-\gamma$ final state. The QCD corrections are similar, because they only affect the IS quarks and do not depend on the final state. The EW corrections corresponding to the $q\bar{q}$ channel are identical with the weak corrections including the large Sudakov logarithms and turn out to be of similar size quite independent of the final state. The photonic corrections, which only involve the IS quarks, are negligible for $\bar{\nu}\nu\gamma$ production, i.e. they are almost completely absorbed into the PDFs. The quark–photon-induced corrections roughly differ by a factor of two in the cases of $l^+l^-\gamma$ and $\bar{\nu}\nu\gamma$ production, since they depend on the FS particles: In the visible decay channel the IS photon (discussed in Section 4.6) can also couple to the FS charged leptons, whereas in the invisible decay channel it can only couple to the IS quarks.

4.7.3 Results on transverse-mass distributions

The transverse three-body mass of the neutrinos and the photon is given by

$$M_{T,\,\bar{\nu}\nu\gamma} = \sqrt{\left(p_{T,miss} + p_{T,\gamma}\right)^2 - \left(\mathbf{p}_{T,miss} + \mathbf{p}_{T,\gamma}\right)^2}\,, \tag{4.16}$$

where we always take the hardest photon if there are two. The corresponding distribution is shown on the left side of Fig. 4.12. Comparing this with the invariant three-body mass of the charged leptons and the photon given in Fig. 4.8, we see that the QCD corrections are flat and have the same trend in both distributions. This can be explained with the same argument as in case of the transverse-momentum distributions, since the QCD corrections only act on the IS quarks and do not depend on the FS leptons. Note that in the invisible decay channel the distribution only starts at 190 GeV at NLO and at 200 GeV at LO owing to the larger p_T cuts. The EW corrections to the $q\bar{q}$ channel are considerably larger in the invisible channel which is due to the fact that we consider the *transverse* three-body mass instead of

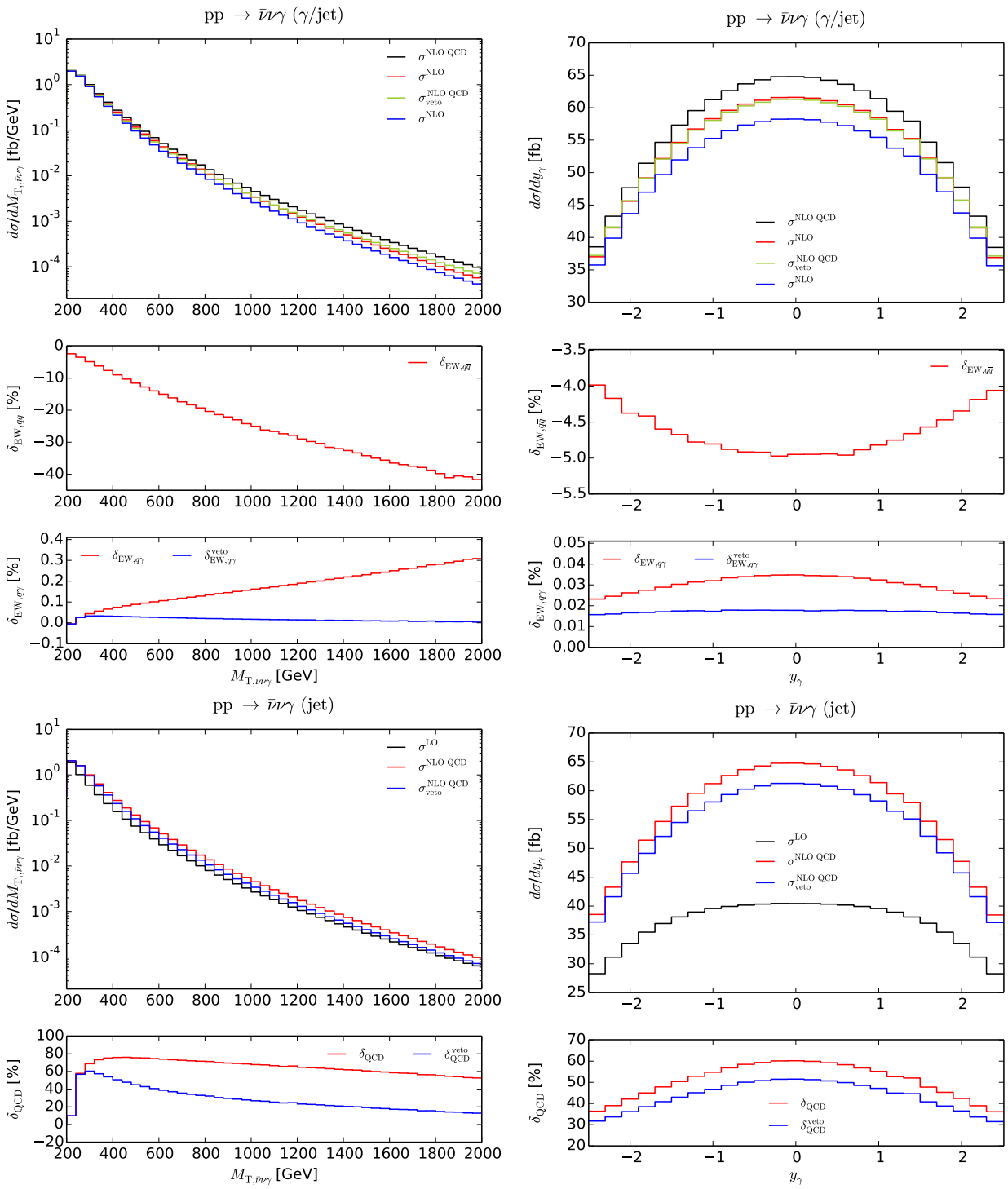

Figure 4.12: Distribution in the transverse three-body mass $M_{\mathrm{T},\bar{\nu}\nu\gamma}$ of the neutrino pair and the hardest photon and the rapidity y_γ of the hardest photon, including EW (top) and QCD corrections (bottom). The upper boxes show absolute predictions, the lower relative corrections.

the full three-body mass. If the latter gets large, there is still the possibility that all transverse momenta are moderate or small. By contrast a large transverse three-body mass requires some large transverse momenta, so that the kinematical configuration is closer to the Sudakov regime where all Minkowski products of momenta are large and EW corrections are strongly enhanced. The corrections from the quark–photon channel are below 1% with and without jet veto and therefore negligible.

4.7.4 Results on rapidity distributions

The rapidity distribution of the hardest photon is shown on the right side of Fig. 4.12. It receives large QCD corrections between 30% and 60%. The jet veto diminishes the QCD corrections by $5-10\%$. The EW corrections to the $q\bar{q}$ channel mainly originating from the purely weak corrections are of the order of -5% and almost flat and therefore reflecting the corrections to the integrated cross section. The EW corrections are small compared to the QCD corrections, but not completely negligible.

Conclusions

The production of a photon in association with a massive vector boson including the leptonic decays is one of the simplest processes to probe the EW gauge sector of the SM. As a part of the gauge-boson pair production processes it is of great interest in several phenomenological studies at a hadron collider as the LHC. $\mathrm{W} + \gamma$ production allows direct access to the coupling of the photon to the W boson and facilitates the investigation of deviations from the standard form of the $\mathrm{WW}\gamma$ vertex. The production of a charged lepton pair and a photon constitutes the main background process for the Higgs decay into a Z boson and a photon and is also used for the study of non-standard effects resulting in $\mathrm{ZZ}\gamma$ and $\mathrm{Z}\gamma\gamma$ couplings. The sub-process of $\mathrm{Z} + \gamma$ production where the Z boson decays invisibly in two neutrinos is an important signal within the searches of many exotic new-physics models.

In this work we presented a full calculation of QCD and EW NLO corrections for $\mathrm{W}^+ + \gamma$ production and for the charge-conjugated process of $\mathrm{W}^- + \gamma$ production as well as for $\mathrm{Z} + \gamma$ production. This calculation includes the leptonic decay of the vector bosons, and all off-shell effects of the intermediate states have taken into account by using the complex-mass scheme. Each of the $\mathrm{V} + \gamma$ production processes includes quark–antiquark-, gluon- and photon-induced channels. Additionally, the dilepton plus photon production involves contributions with two initial-state photons. A detailed discussion of the partonic channels can be found in Chapter 2. For the treatment of IR singularities we have applied the dipole subtraction formalism. Within the calculation of quark–antiquark-induced EW corrections we are faced with final-state photon radiation off fermions where we have considered two different scenarios. In one case we assume that a collinear photon–lepton system can not be separated in a detector so that such a configuration is treated as one quasi-particle. In a second scenario mimicking final-state muons we proceed from the assumption that the photon will be absorbed in the electromagnetic calorimeter of the detector and the muon is measured in the muon chamber. In that case photon and muon can be separated also if they are collinear. The final states of the partonic processes for photon-induced and QCD corrections contain photons and jets. For the actual distinction between hard photons and hard jets in their overlap region we applied two different implementations. We used the concept of democratic clustering in combination with a quark-to-photon fragmentation function or the Frixione isolation scheme. The details of the applied techniques are outlined in Chapter 3. For the QCD corrections we found large corrections which result from the appearance of new production channels (gluon-induced contributions). However, these large corrections come from events with hard jets, meaning that they should better considered as part of $\mathrm{V} + \mathrm{jet}$ production rather than $\mathrm{V} + \gamma$ production. For this reason we also calculated these contributions including the application of a jet veto.

Focussing on $\mathrm{W}^+ + \gamma$ production we found that the QCD corrections give the dominating contribution $\sim 150\%$ to the total cross section. The EW corrections only contribute with $2 - 3\%$ and around 1% for the $q\bar{q}$ and $q\gamma$ channel, respectively, and partially compensate each other. However, in several distributions the picture is different. Reflecting the general features of EW corrections we found that in the TeV range (Sudakov logarithms) the $q\bar{q}$ channel contributes with several 10% and significant corrections appear in the resonance region of the transverse mass distribution of the lepton pair. Additionally, the $q\gamma$ channel also contributes

with several 10% in case of no jet veto and, thus, partially compensates the QCD corrections. The application of a jet veto reduces the $q\gamma$ channel to almost zero but also the QCD corrections so that the EW quark–antiquark-induced corrections become the dominant contributions.

For the charge-conjugated process of $W^-+\gamma$ production we found very similar results. While the difference in total cross section at leading-order originates from the different PDF factors due the charge-conjugated initial state, the numerical values of the relative EW and QCD corrections to the total cross section are almost identical. In most oft the studied distributions we found no significant deviations in the shape of the distributions. However, in the p_T distributions of the charged leptons and the photon a difference is visible.

For the dilepton production in association with a photon we observe that again the QCD corrections of $\mathcal{O}(60\%)$ give the dominant contribution to the total cross section. The quark–antiquark-induced EW corrections contribute with around -3% and -5% for the case of dressed leptons and final-state muons, respectively. Here, the contributions from the $q\gamma$ and $\gamma\gamma$ channels are negligible. In some of the distributions the $q\gamma$ channel contributes up to a few percent but can not compensate the QCD corrections in the same order of magnitude as for $W+\gamma$ production. The $\gamma\gamma$ channel is negligible in the regions of large cross section. However, one should remember that the interpretation of photon-induced and, especially, double-photon induced contributions should be treated with caution due to the large uncertainties $\sim 100\%$ of the photon PDFs at large Bjorken-x.

The $Z+\gamma$ production process where the Z boson decays invisibly in two neutrinos has a much smaller total cross section at LO due the strong cuts on $p_{T,\text{miss}}$ and $p_{T,\gamma}$. The QCD corrections around 50% give the dominant contribution. The quark–antiquark-induced EW corrections are found to be of the order -5%. The $q\gamma$ channel is again negligible in the total cross section and also in the distributions it contributes less than 1%.

The numerical results presented in Chapter 4 of this thesis push the existing calculation of EW corrections to the level of complete EW NLO calculations for $V+\gamma$ production including the leptonic decays of the vector bosons and all off-shell effects. The contributions from all channels with initial-state photons are also included. The calculation of NLO corrections presented in this work have been implemented in a highly flexible Monte Carlo program which allows to calculate predictions for total cross sections and also arbitrary distributions in the form of histograms.

Appendix A

Monte Carlo phase-space integration

In this work we mostly discussed the partonic cross section, the PDFs and the treatment of various types of singularities inside them. In the end, the calculation of the hadronic cross section defined in Eq. (1.70) requires an integration which (due to the complicated structure of the integrand) can not be worked out analytically. For the numerical evaluation of the integrand we use the so-called Monte Carlo method. In this chapter we outline the technical details about this method and its application to the phase-space integration. In Section A.1 we summarize the basic strategy and present the global formulae which are applied and in Section A.2 we discuss the explicit parametrization of the phase space.

A.1 Basic concept

The basic idea of the Monte Carlo method is based on the law of large numbers. This law says that for a large set of n randomly created numbers u_i the sum of function values for a function f divided by N converges to the expectation of the function f

$$\frac{1}{n}\sum_{i=1}^{N} f\left(u_i\right) \to \frac{1}{b-a}\int_a^b \mathrm{d}u\, f\left(u\right) , \tag{A.1}$$

so that the integrals can be calculated by a discrete finite sum. A rather detailed overview about the theory and practical applications of the Monte Carlo method can be found e.g. in Ref. [105].

In order to apply the Monte Carlo method to the calculation of the total cross section we start with the definition of the hadronic cross section at NLO (as introduced in Eq. (1.70)) for an general process $A\left(p_A\right) + B\left(p_B\right) \to f + X$

$$\mathrm{d}\sigma_{AB\to f} = \sum_{a,b}\int_0^1 \mathrm{d}x_a \int_0^1 \mathrm{d}x_b \Big[f_{a|A}(x_a) f_{b|B}(x_b)\, \mathrm{d}\hat{\sigma}_{ab\to f}(x_a x_b S)\Big] . \tag{A.2}$$

Therein we omit arguments since they are not relevant for the phase-space integration. $\hat{\sigma}_{ab\to f}$ represents the IR-safe partonic cross section where all IR singularities are already treated with dipole subtraction or absorbed to the PDFs via a redefinition. $\hat{\sigma}_{ab\to f}$ is defined as

$$\mathrm{d}\hat{\sigma}_{ab\to f} = \frac{1}{2x_a x_b S}\int \mathrm{d}\Phi \left|\mathcal{M}\left(\Phi\right)\right|^2 , \tag{A.3}$$

where S is the hadronic centre-of-mass energy which is related with the partonic energy via $\hat{s} = x_a x_b S$. Φ represents the generic phase space and the various contributions from squared

amplitudes are denoted by $|\mathcal{M}|^2$. In summary, two different types of integrations $\mathrm{d}x_a/\mathrm{d}x_b$ and $\mathrm{d}\Phi$ have to be performed.

The integration over the parton energy fractions x_a/x_b leads to a complication: From the so-called flux factor $1/(x_a x_b S)$ in Eq. (A.3) it follows directly that the hadronic cross section shows a peak at the low-energy limits $x_{a/b} \to 0$. This peak can be avoided by introducing a lower cut $\hat{s}_{\min}$ on the level of the partonic centre-of-mass energy $\hat{s}$. In order to illustrate the consequences of this cut we introduce the following substitutions

$$x_a \to \tau = x_a x_b = \frac{\hat{s}}{S}\,, \qquad x_b \to x = x_b\,, \tag{A.4}$$

so that Eq. (A.2) transforms to

$$\mathrm{d}\sigma_{AB\to f} = \frac{1}{2S} \sum_{a,b} \int_{\tau_{\min}}^{1} \frac{\mathrm{d}\tau}{\tau} \int_{\tau}^{1} \frac{\mathrm{d}x}{x} \Big[f_{a|A}\left(\frac{\tau}{x}\right) f_{b|B}\left(x\right)\, \mathrm{d}\hat{\sigma}_{ab\to f}\left(\tau S\right) \Big]\,. \tag{A.5}$$

Therein the cut on the lower energy is included in $\tau_{\min} = \hat{s}_{\min}/S$. Choosing a non zero value for $\hat{s}_{\min}$ and so for $\tau_{\min}$ directly excludes the singular regions $x_a = x_b = 0$. In Eq. (A.5) we end up with the factor $1/(\tau x)$ in the integrand leading to a non-flat structure. The flattening of this factor is done by a specific choice for the mapping between a generated random number r and x or τ, respectively. In order to derive this mapping we start with the x-integration which can be rewritten as

$$\int \frac{\mathrm{d}x}{x} = \int \mathrm{d}r\, \frac{\mathrm{d}x(r)}{\mathrm{d}r} \frac{1}{x(r)}\,. \tag{A.6}$$

In order to flatten the singularity $1/x$ we suppose the following relation for the mapping

$$\frac{\mathrm{d}x(r)}{\mathrm{d}r} \propto x(r)\,. \tag{A.7}$$

Assuming the boundary conditions $x(0) = \tau$ and $x(1) = 1$ (defined by the integration limits in Eq. (A.5)) this relation can be fulfilled by

$$x(r_1) = \tau^{1-r_1}\,, \qquad g_x(x) = \left(\frac{\mathrm{d}x(r_1)}{\mathrm{d}r_1}\right)^{-1} = -\frac{1}{x \log \tau}\,, \tag{A.8}$$

where $g_x(x)$ denotes the inverse Jacobian related to the substitution $x \to r_1$. Here we use the random number r_1 instead of the generic r to indicate that the random numbers for the x- and τ-mapping are different. The mapping $x(r_1)$ is chosen such that the Monte Carlo integration is achieved over a flat integrand.

From Eqs. (A.5) and (A.8) it follows directly that the integrand of the τ-integration includes the form $(\log \tau)/\tau$. Applying the same procedure as described for x we find for the τ-mapping

$$\tau = \tau_{\min}^{\sqrt{1-r_2}}\,, \qquad g_\tau(\tau) = \left(\frac{\mathrm{d}\tau(r_2)}{\mathrm{d}r_2}\right)^{-1} = -\frac{2}{\log^2(\tau_{\min})} \frac{\log \tau}{\tau}\,, \tag{A.9}$$

where $\tau_{\min} = \hat{s}_{\min}/S$ and $g_\tau(\tau)$ represents the corresponding inverse Jacobian. Finally, the random numbers r_1 and r_2 can be translated to x_a and x_b with

$$x_a = \frac{\tau(r_2)}{x(r_1)}\,, \qquad x_b = x(r_1)\,, \tag{A.10}$$

and the phase-space density

$$g_{x,\tau}(x_a, x_b) = \frac{2}{\log^2(\tau_{\min})} \frac{1}{x_a x_b^2}\,, \tag{A.11}$$

which is the product of the inverse Jacobians in (A.8) and (A.9) expressed in terms of x_a and x_b.

The mapping discussed so far reflects the easiest choice to flatten the flux-factor in Eq. (A.3). However, in order to optimize the convergence of the numerical integration there are possibilities to adapt the mapping to the corresponding partonic process. In case of vector-boson production in association with a photon the dominant contribution to the total cross section arise from events related to the energy region around the mass of the vector boson. Finally, we use the knowledge about the shape of the cross section in addition to the mapping discussed in this section. Therewith we are able to achieve a concentration of events to the phase-space region where the integrand contributes most.

A.2 Generic phase-space decomposition

In general, the calculation of scattering amplitudes necessitates the calculation of several Feynman diagrams. These diagrams have various propagator structures which peak in different regions of the phase space. As it is worked out in detail in Appendix C of Ref. [106] the various phase-space parametrizations which are necessary to ensure a proper numerical integration can be constructed by the use of universal building blocks. This procedure will be outlined in the following.

In order to describe the construction of the phase space we consider a generic $2 \to n$ partonic scattering process described by

$$a(p_a) + b(p_b) \to c_1(k_1) + \ldots + c_n(k_n)\,, \tag{A.12}$$

where the momenta of the incoming particles p_a, p_b and the momenta of the outgoing particles k_i, $i = 1, 2, \ldots, n$ were given in parenthesis. In four dimensions the corresponding differential phase space is defined by

$$\mathrm{d}\Phi_{(2\to n)} = (2\pi)^{4-3n} \left[\prod_{i=1}^{n} \mathrm{d}^4 k_i\, \delta\left(k_i^2 - m_i^2\right) \theta\left(k_i^0\right)\right] \delta^{(4)}\left(p_a + p_b - \sum_{i=1}^{n} k_i\right)\,, \tag{A.13}$$

where the IS particles are assumed to be massless and the masses of the FS particles are denoted by $m_i = \sqrt{k_i^2}$. The phase-space integral $\int \mathrm{d}\Phi_{(2\to n)}$ then can be constructed by three different types of building blocks:

1. The phase-space integration over invariant where a resonant propagator occurs in the s-channel.

2. The phase-space integration of a particle decay: $i(p_{12}) \to f_1(k_1) + f_2(k_2)$.

3. The phase-space integration of a t-channel $2 \to 2$ scattering process:
   $i_1(p_1) + i_2(p_2) \to f_1(k_1) + f_2(k_2)$.

For a partonic process with an intermediate vector boson decaying in the s-channel the squared amplitude has the following Breit–Wigner structure

$$|\mathcal{M}|^2 \propto \frac{1}{(p^2 - M_\mathrm{V}^2)^2 + M_\mathrm{V}^2 \Gamma_\mathrm{V}^2}\,. \tag{A.14}$$

Starting from the generic phase-space integration in Eq. (A.3) we introduce a generic mapping $\mathbf{h}\,(\mathbf{r})$ transforming a set of random numbers $\mathbf{r}$ with $0 < r_i < 1$ and $i = 1, \ldots, 3n_f - 4$ to

the phase-space elements in Φ

$$\int \mathrm{d}\Phi \; |\mathcal{M}\left(p\left(\Phi\right)\right)|^2 = \int_0^1 \prod_{i=1}^{3n_f-4} \mathrm{d}r_i \, \frac{|\mathcal{M}\left(p\left(\mathbf{h}\left(\mathbf{r}\right)\right)\right)|^2}{g\left(p\left(\mathbf{h}\left(\mathbf{r}\right)\right)\right)} \,. \tag{A.15}$$

Therein we made the dependence of the particle momenta from the phase-space elements Φ or the random numbers $\mathbf{r}$ explicit. In case of a multidimensional function $\mathbf{h}\left(\mathbf{r}\right)$ the general transformation of the variables reads

$$\int \frac{\mathrm{d}\mathbf{h}}{\mathbf{h}} = \int \mathrm{d}\mathbf{r} \left| \frac{\mathrm{d}\mathbf{h}\left(\mathbf{r}\right)}{\mathrm{d}\mathbf{r}} \right| \frac{1}{\mathbf{h}\left(\mathbf{r}\right)} \,, \tag{A.16}$$

where $|\ldots|$ denotes the determinant. Therewith the density in Eq. (A.15) is given by

$$g\left(p\left(\mathbf{h}\left(\mathbf{r}\right)\right)\right) = \left| \frac{\mathrm{d}\mathbf{h}\left(\mathbf{r}\right)}{\mathrm{d}\mathbf{r}} \right|^{-1} \,. \tag{A.17}$$

For our purposes we choose the following specific mapping

$$h_{\mathrm{prop}}\left(r\right) = M_{\mathrm{V}}\Gamma_{\mathrm{V}} \tan\left[y_1 + (y_2 - y_1)r\right] + M_{\mathrm{V}}^2 \,, \tag{A.18}$$

where we introduce the abbreviations

$$y_{1/2} = \arctan\left(\frac{p_{\mathrm{min/max}}^2 - M_{\mathrm{V}}^2}{M_{\mathrm{V}}\Gamma_{\mathrm{V}}} \right) \,. \tag{A.19}$$

The values p_{min} and p_{max} describe the limits of the phase-space integration. The mapping $h_{\mathrm{prop}}\left(r\right)$ chosen in Eq. (A.18) results in the phase-space density

$$g_{\mathrm{prop}}(h_{\mathrm{prop}}\left(r\right), p^2\left(r\right)) = \frac{M_{\mathrm{V}}\Gamma_{\mathrm{V}}}{(y_2 - y_1)[(p^2\left(r\right) - M_{\mathrm{V}}^2)^2 + M_{\mathrm{V}}^2\Gamma_{\mathrm{V}}^2]} \tag{A.20}$$

which will exactly cancel the denominator in (A.14) so that the total integrand in Eq. (A.15) is flat. Finally, this mapping ensures is that during the Monte Carlo phase-space integration most of the random numbers will be sampled in regions of the phase space where the propagator becomes resonant and which give the dominant contribution to the total cross section.

For the description of the decay of particle i we first introduce the total energy squared of the decay products

$$s_{12} = (k_1 + k_2)^2 \,. \tag{A.21}$$

Therewith the particle decay is described in the rest frame of i by the use of the polar angle $\hat{\phi}$ and the azimuthal angle $\hat{\theta}$ (the hat indicates: rest frame of i). The phase-space integral then reads

$$\begin{aligned} \int \mathrm{d}\Omega_d\left(s_{12}, k_1^2, k_2^2\right) &= \int \mathrm{d}^4k_1 \int \mathrm{d}^4k_2 \, \delta\left(k_1^2 - m_1^2\right) \theta\left(k_1^0\right) \delta\left(k_2^2 - m_2^2\right) \theta\left(k_2^0\right) \delta^{(4)}\left(p_{12} - k_1 - k_2\right) \\ &= \frac{\lambda^{1/2}\left(s_{12}, k_1^2, k_2^2\right)}{8 s_{12}} \int_0^{2\pi} \mathrm{d}\hat{\phi} \int_{-1}^{1} \mathrm{d}\cos\hat{\theta} \\ &= \frac{1}{g_d\left(s_{12}, k_1^2, k_2^2\right)} \int_0^1 \mathrm{d}r_1 \int_0^1 \mathrm{d}r_2 \,, \end{aligned} \tag{A.22}$$

where the first line shows the differential phase space derived from Eq. (A.13). In line 2 we introduce the integration values $\hat{\phi}$ and $\cos\hat{\theta}$ and we use the Kaellen function

$$\lambda(x,y,z) = x^2 + y^2 + z^2 - 2(xy + xz + yz)\,. \tag{A.23}$$

The integration of the values $\hat{\phi}$ and $\cos\hat{\theta}$ is then transformed to an integration of random numbers in line 3. The application of the Monte Carlo method (as discussed at the beginning of Section A.1) uses the simple mappings

$$\hat{\phi} = 2\pi r_1\,, \qquad \cos\hat{\theta} = 2r_2 - 1\,, \tag{A.24}$$

where $r_{1/2}\,\epsilon\,[0,1]$ represent two different random numbers. Therewith the corresponding density $g_d\,(s_{12}, k_1^2, k_2^2)$ is given by

$$g_d\left(s_{12}, k_1^2, k_2^2\right) = \frac{2s_{12}}{\pi\lambda^{1/2}\left(s_{12}, k_1^2, k_2^2\right)}\,. \tag{A.25}$$

The momenta of the decay products are then defined as

$$\hat{k}_1^\mu = \left(\hat{k}_1^0, \hat{\mathbf{k}}_1\right)\,, \qquad \hat{k}_2^\mu = \left(\hat{k}_2^0, \hat{\mathbf{k}}_2\right)\,, \tag{A.26}$$

where the energy $\hat{k}_{1/2}^0$ and the absolute value of the three-momentum $|\hat{\mathbf{k}}_{1/2}|$ are given by

$$\begin{aligned}
\hat{k}_1^0 &= \frac{s_{12} + k_1^2 - k_2^2}{2\sqrt{s_{12}}}\,, \qquad |\hat{\mathbf{k}}_1| = \frac{\lambda^{1/2}\left(s_{12}, k_1^2, k_2^2\right)}{2\sqrt{s_{12}}}\,, \\
\hat{k}_2^0 &= \frac{s_{12} + k_2^2 - k_1^2}{2\sqrt{s_{12}}}\,, \qquad |\hat{\mathbf{k}}_2| = \frac{\lambda^{1/2}\left(s_{12}, k_2^2, k_1^2\right)}{2\sqrt{s_{12}}}\,,
\end{aligned} \tag{A.27}$$

with s_{12} defined in Eq. (A.21). Since the momenta $\hat{k}_{1/2}$ are calculated in the rest frame of particle i they have to be boosted to the laboratory frame. This boost is described by the matrix $\mathcal{B}\,(Q^0, \mathbf{Q})$ transforming an arbitrary four-vector k^μ to the rest frame of Q^μ and its inverse transformation $\mathcal{B}\,(Q^0, -\mathbf{Q})$ is then used for the Lorentz transformation from rest frame to laboratory frame

$$k^0 = \gamma\hat{k}^0 + \mathbf{b}\hat{\mathbf{k}}\,, \qquad \mathbf{k} = \hat{\mathbf{k}} + \mathbf{b}\frac{\mathbf{b}\hat{\mathbf{k}}}{1-\gamma} + \mathbf{b}\hat{k}^0\,, \tag{A.28}$$

where we introduce $\mathbf{b} = \mathbf{Q}/m$, $\gamma = Q^0/m$ and $m = \sqrt{Q^2}$. Since the decay of the particle i is isotropic the coordinate system can be chosen arbitrarily. If we choose the flight direction of particle f_1 as the x_3-axes the momenta of the decay products f_1 and f_2 are given by

$$k_1 = \mathcal{B}\left(p_{12}^0, -\mathbf{p}_{12}\right)\mathcal{R}\left(\hat{\phi}, \cos\hat{\theta}\right)\begin{pmatrix} \frac{p_{12}^2 + k_1^2 - k_2^2}{2\sqrt{p_{12}^2}} \\ 0 \\ 0 \\ \frac{\lambda^{1/2}\left(p_{12}^2, k_1^2, k_2^2\right)}{2\sqrt{p_{12}^2}} \end{pmatrix}\,, \qquad k_2 = p_{12} - k_1\,, \tag{A.29}$$

in the laboratory frame. Therein the rotation matrix $\mathcal{R}\left(\hat{\phi}, \cos\hat{\theta}\right)$ is given by

$$\mathcal{R}\left(\hat{\phi}, \cos\hat{\theta}\right) = \begin{pmatrix} 1 & 0 & 0 & 0 \\ 0 & \cos\hat{\phi} & \sin\hat{\phi} & 0 \\ 0 & -\sin\hat{\phi} & \cos\hat{\phi} & 0 \\ 0 & 0 & 0 & 1 \end{pmatrix}\begin{pmatrix} 1 & 0 & 0 & 0 \\ 0 & \cos\hat{\theta} & 0 & \sin\hat{\theta} \\ 0 & 0 & 1 & 0 \\ 0 & -\sin\hat{\theta} & 0 & \cos\hat{\theta} \end{pmatrix}\,. \tag{A.30}$$

For the description of the $2 \to 2$ scattering process mentioned in point 3 two particle with momenta p_1 and p_2 transform in two particles with momenta k_1 and k_2. The phase-space integration can be parametrized by an integration of the polar angle $\hat{\phi}$ and the Mandelstam variable $t = (p_1 - k_1)^2$ in the rest frame of $p_{12} = p_1 + p_2$. The x_3-axes is chosen in $\mathbf{p}_1$ direction so that the momenta are given by

$$\hat{p}_{1/2} = \begin{pmatrix} \frac{p_{12}^2 + p_1^2 - p_2^2}{2\sqrt{p_{12}^2}} \\ 0 \\ 0 \\ \pm \frac{\lambda^{1/2}\left(p_{12}^2, p_1^2, p_2^2\right)}{2\sqrt{p_{12}^2}} \end{pmatrix}, \qquad \hat{k}_1 = \mathcal{R}\left(\hat{\phi}, \cos\hat{\theta}\right) \begin{pmatrix} \frac{p_{12}^2 + k_1^2 - k_2^2}{2\sqrt{p_{12}^2}} \\ 0 \\ 0 \\ \frac{\lambda^{1/2}\left(p_{12}^2, k_1^2, k_2^2\right)}{2\sqrt{p_{12}^2}} \end{pmatrix}, \tag{A.31}$$

and $\hat{k}_2 = \hat{p}_1 + \hat{p}_2 - \hat{k}_1$. The integral then reads

$$\begin{aligned} \int \mathrm{d}\Omega_p\left(p_1, p_2, k_1^2, k_2^2\right) &= \int \mathrm{d}^4 k_1 \int \mathrm{d}^4 k_2\, \delta\left(k_1^2 - m_1^2\right) \theta\left(k_1^0\right) \delta\left(k_2^2 - m_2^2\right) \theta\left(k_2^0\right) \delta^{(4)}\left(p_{12} - k_1 - k_2\right) \\ &= \frac{1}{4\lambda^{1/2}\left(s_{12}, p_1^2, p_2^2\right)} \int_0^{2\pi} \mathrm{d}\hat{\phi} \int_{t_{\min}}^{t_{\max}} \mathrm{d}t\,, \end{aligned} \tag{A.32}$$

where the variable t is defined as

$$t = k_1^2 + p_1^2 - \frac{(s_{12} + k_1^2 - k_2^2)(s_{12} + p_1^2 - p_2^2) - \lambda^{1/2}\left(s_{12}, k_1^2, k_2^2\right) \lambda^{1/2}\left(s_{12}, p_1^2, p_2^2\right) \cos\hat{\theta}}{2 s_{12}} \tag{A.33}$$

and exclusively depends on the azimuthal angle $\hat{\theta}$. s_{12} is defined Eq. (A.21). The integration limits $t_{\max/\min}$ reflecting the values $\cos\hat{\theta} = \mp 1$ read

$$t^{\max/\min} = k_1^2 + p_1^2 - \frac{(s_{12} + k_1^2 - k_2^2)(s_{12} + p_1^2 - p_2^2) \pm \lambda^{1/2}\left(s_{12}, k_1^2, k_2^2\right) \lambda^{1/2}\left(s_{12}, p_1^2, p_2^2\right)}{2 s_{12}}\,. \tag{A.34}$$

In analogy to Eq. (A.28) the momenta of the FS particles f_1 and f_2 in the laboratory frame can be derived from the momenta in the rest frame with a Lorentz boost and a rotation

$$k_{1/2} = \mathcal{B}\left(p_{12}^0, -\mathbf{p}_{12}\right) \mathcal{R}\left(-\tilde{\phi}, \cos\tilde{\theta}\right) \hat{k}_{1/2}\,, \tag{A.35}$$

where the angles $\tilde{\phi}$ and $\tilde{\theta}$ have to be calculated from the boosted incoming momentum $\tilde{p}_1 = \mathcal{B}\left(p_{12}^0, \mathbf{p}_{12}\right) p_1$ with the following relations

$$\tilde{\phi} = \begin{cases} \arctan\left(\frac{\tilde{p}_1^2}{\tilde{p}_1^1}\right) & \text{if } \tilde{p}_1^1 > 0 \\ \pi + \arctan\left(\frac{\tilde{p}_1^2}{\tilde{p}_1^1}\right) & \text{if } \tilde{p}_1^1 < 0 \end{cases}, \qquad \cos\tilde{\theta} = \frac{\tilde{p}_1^3}{|\tilde{\mathbf{p}}_1|}\,. \tag{A.36}$$

The tilde indicates the rest frame of $p = p_1 + p_2$.

Appendix B

Loop integrals

In this chapter we discuss the numerical evaluation of one-loop integrals used for the calculation of virtual QCD and EW corrections to the processes defined in Eqs. (2.1), (2.3) and (2.4). In Section B.1 we introduce the common conventions to describe one-loop integrals and in Section B.2 we outline the technical details of the reduction of tensor integrals.

B.1 General structure of tensor integrals

The calculation of one-loop diagrams with M external legs requires the computation of N-point tensor integrals with $N \leq M$. The general form of a N-point tensor integral with rank P is given by [61]

$$T^{N,\mu_1\dots\mu_P}(p_1,\dots,p_{N-1},m_0,\dots,m_{N-1}) = \frac{(2\pi\mu)^{4-D}}{\mathrm{i}\pi^2}\int d^Dq \frac{q^{\mu_1}\dots q^{\mu_P}}{D_0D_1\dots D_{N-1}}\,, \tag{B.1}$$

where the momenta $p_1, p_2-p_1, p_3-p_2, \dots, p_{N-2}-p_{N-1}$ indicate the incoming external momenta (see Fig. B.1). The denominator factors are defined as

$$D_k = (q+p_k)^2 - m_k^2 + \mathrm{i}\epsilon\,, \quad k = 0,1,\dots,N-1\,, \quad p_0 = 0\,. \tag{B.2}$$

Therein p_k and m_k indicate the momentum and the mass of the particle of the k-th loop propagator. The tensor integrals are totally symmetric in the Lorentz indices μ_k and they are invariant under permutations of the propagators D_k. $\mathrm{i}\epsilon$ (where $\epsilon > 0$) is an infinitesimally small imaginary part which is used for regularising singularities of the integrand. The tensor integrals are defined with an analytical continuation in $D = 4 - 2\epsilon$ dimensions which is necessary to allow regularization of the UV divergences. In order to conserve the correct mass dimension of the integral this necessitates the introduction of the mass scale μ.

The 1-, 2-, 3-, 4- and 5-point functions which appear in the calculation of one-loop amplitudes for a general $2 \to 3$ process are commonly labeled with $T^1 = A$, $T^2 = B$, $T^3 = C$, $T^4 = D$ and $T^5 = E$. The case $P = 0$ in Eq. (B.1) defines the scalar N-point integral T_0^N where no integration momenta appear in the numerator of the loop integral.

Due to Lorentz covariance a tensor decomposition of the following structure is possible

$$T^{N,\mu_1\dots\mu_P}(p_1,\dots,p_{N-1},m_0,\dots,m_{N-1}) = \sum_{i_1,\dots,i_P=0}^{N-1} T^N_{i_1\cdots_P} p_{i_1\mu_1}\dots p_{i_P\mu_P}\,, \tag{B.3}$$

the tensor coefficients $T^N_{i_1\cdots_P}$ are totally symmetric. The correct terms depending on the external momenta p_i and the metric tensor $g_{\mu\nu}$ can be derived from Eq. (B.3) in the following way: we

reject all term with an odd number of p_0's and we replace products with even numbers of p_0 according to the following scheme

$$\begin{aligned} p_{0\mu_1}p_{0\mu_2} &\longrightarrow g_{\mu_1\mu_2} \\ p_{0\mu_1}p_{0\mu_2}p_{0\mu_3}p_{0\mu_4} &\longrightarrow g_{\mu_1\mu_2}g_{\mu_3\mu_4} + g_{\mu_1\mu_3}g_{\mu_2\mu_4} + g_{\mu_1\mu_4}g_{\mu_2\mu_3}\,. \end{aligned} \tag{B.4}$$

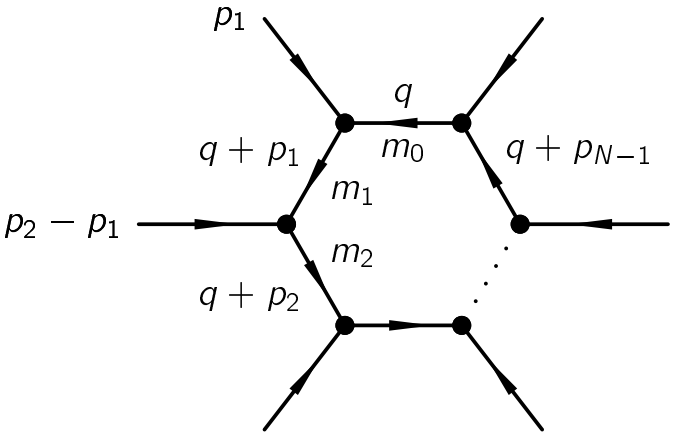

Figure B.1: General N-point tensor integral.

Therewith the decompositions for the lowest order integrals are

$$\begin{aligned} B_\mu &= p_{1\mu}B_1\,, \\ B_{\mu\nu} &= g_{\mu\nu}B_{00} + p_{1\mu}p_{1\nu}B_{11}\,, \\ C_\mu &= \sum_{i=1}^{2} p_{i\mu}C_i\,, \\ C_{\mu\nu} &= g_{\mu\nu}C_{00} + \sum_{i,j=1}^{2} p_{i\mu}p_{j\nu}C_{ij}\,, \\ C_{\mu\nu\rho} &= \sum_{i=1}^{2}(g_{\mu\nu}p_{i\rho} + g_{\nu\rho}p_{i\mu} + g_{\mu\rho}p_{i\nu})\,C_{i00}\,, \\ &\quad + \sum_{i,j,k=1}^{2} p_{i\mu}p_{j\nu}p_{k\rho}C_{ijk}\,. \end{aligned} \tag{B.5}$$

B.2 Explicit calculation of tensor integrals

For the explicit calculation of one-loop integrals we use the fortran-library `COLLIER` [59]. The applied method for the reduction of tensor integrals and the calculation of scalar integrals depends on the number of external momenta of the one-loop integral.

For the numerical evaluation of 1-point and 2-point functions we use explicit analytical expressions from Refs. [61, 107]. For $N = 3, 4$ the tensor integrals will be reduced via Passarino–Veltman algorithm [107] to integrals with lower rank P and integrals with lower N which formally can be written as

$$\Delta T^{N,\mu_1\ldots\mu_P} = [T^{N,\mu_1\ldots\mu_{P-1}}, T^{N,\mu_1\ldots\mu_{P-2}}, T^{N-1,\mu_1\ldots\mu_P}]\,, \tag{B.6}$$

where on the r.h.s. a linear combination of reduced tensor integrals is indicated by $[\dots]$ and $\Delta = \det(Z)$ denotes the the determinant of the Gram matrix

$$Z = \begin{pmatrix} 2p_1p_1 & \dots & 2p_1p_{N-1} \\ \vdots & & \vdots \\ 2p_{N-1}p_1 & \dots & 2p_{N-1}p_{N-1} \end{pmatrix} . \tag{B.7}$$

The system of linear equations given in Eq. (B.6) can be solved by calculating the inverse of the determinant Δ. In regions of the phase space where Δ becomes small this leads to instabilities. Finally, it would result in a linear dependence of the equations. Since this linear dependence appears even for the scalar integrals this issue also persists for other reduction methods. For critical phase-space points where the determinant of the Gram matrix is small the strategy of solving the system of linear equations is the following: we substitute the rank in Eq. (B.6) by $P \to P + 1$ which results in

$$\Delta T^{N,\mu_1\dots\mu_{P+1}} = [T^{N,\mu_1\dots\mu_P}, T^{N,\mu_1\dots\mu_{P-1}}, T^{N-1,\mu_1\dots\mu_P}] . \tag{B.8}$$

Note, that tensor integral $T^{N,\mu_1\dots\mu_P}$ now arises on the l.h.s. At zeroth order we neglect terms of $\mathcal{O}(\Delta)$ and then Eq. (B.8) simplifies to

$$0 = [T^{N,\mu_1\dots\mu_P}, T^{N,\mu_1\dots\mu_{P-1}}, T^{N-1,\mu_1\dots\mu_P}] , \tag{B.9}$$

where $T^{N,\mu_1\dots\mu_P}$ can be calculated from integrals of lower rank P and integrals with a lower number of external legs N. For higher precision the expansion in Δ then can be enhanced to $\mathcal{O}(\Delta^k)$ which necessitates the calculation of tensor integrals with higher rank up to $T^{N,\mu_1\dots\mu_{P+k}}$. Various expansion methods were proposed in Ref. [61] and all of them are implemented in `COLLIER`.

Appendix C

Distributions for $\mathrm{p\ p} \to l^- \bar{\nu}_l\ \gamma + X$

In this chapter we list distributions in various observables for the $\mathrm{W}^- + \gamma$ production at a collider energy of 14 TeV. For each observable we show absolute plots for complete NLO and NLO QCD corrections (large boxes). The corresponding cross sections are defined in Eqs. (4.3) and (4.1), respectively. We also show relative EW corrections for the $q\bar{q}$ and the $q\gamma$ channel as well as relative QCD corrections (small boxes). The relative corrections are defined in Eq. (4.2). For the quark–antiquark-induced correction we show results for the collinear-safe and the non-collinear-safe case. For photon-induced and QCD corrections we present results with and without a jet veto at 100 GeV.

We show distributions in the transverse momenta of the hardest photon and the charged lepton in Fig. C.1. Fig. C.2 displays distributions in the transverse mass of the charged lepton and the neutrino and the transverse three-body mass of the charged lepton, the neutrino and the hardest photon. In Figs. C.3 and C.4 we present various distributions on rapidity y and the azimuthal-angle ϕ. While the absolute values for the differential cross section for $\mathrm{W}^+\gamma$ (presented in Section 4.4) and $\mathrm{W}^-\gamma$ differ due to different PDF factors the shape of the relative corrections look very similar.

In order to illustrate the explicit difference in the relative corrections between $\mathrm{W}^+\gamma$ and $\mathrm{W}^-\gamma$ production we compared in Section 4.5 the distributions of the transverse momentum for the charged lepton and the transverse mass of the lepton–neutrino-pair. These two distributions demonstrate the largest and smallest deviation between $\mathrm{W}^+\gamma$ and $\mathrm{W}^-\gamma$ production. In addition to Fig. 4.5 we show in Figs. C.5–C.7 the comparison of both processes for further observables.

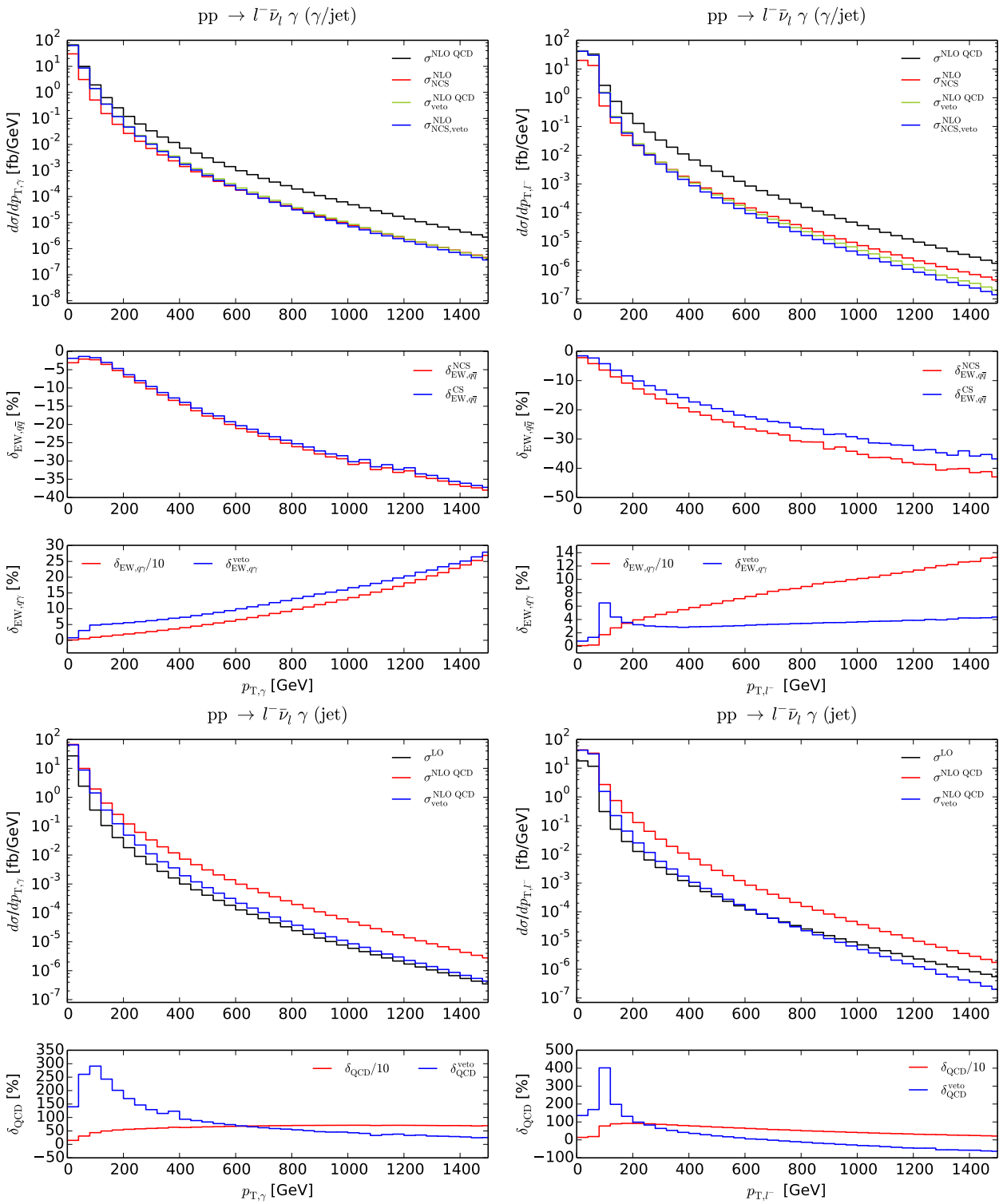

Figure C.1: Distributions in the transverse momentum p_{T} of the photon (left) and the charged lepton (right), including EW (top) and QCD corrections (bottom). For all corrections absolute (upper box) and relative corrections (lower boxes) are shown.

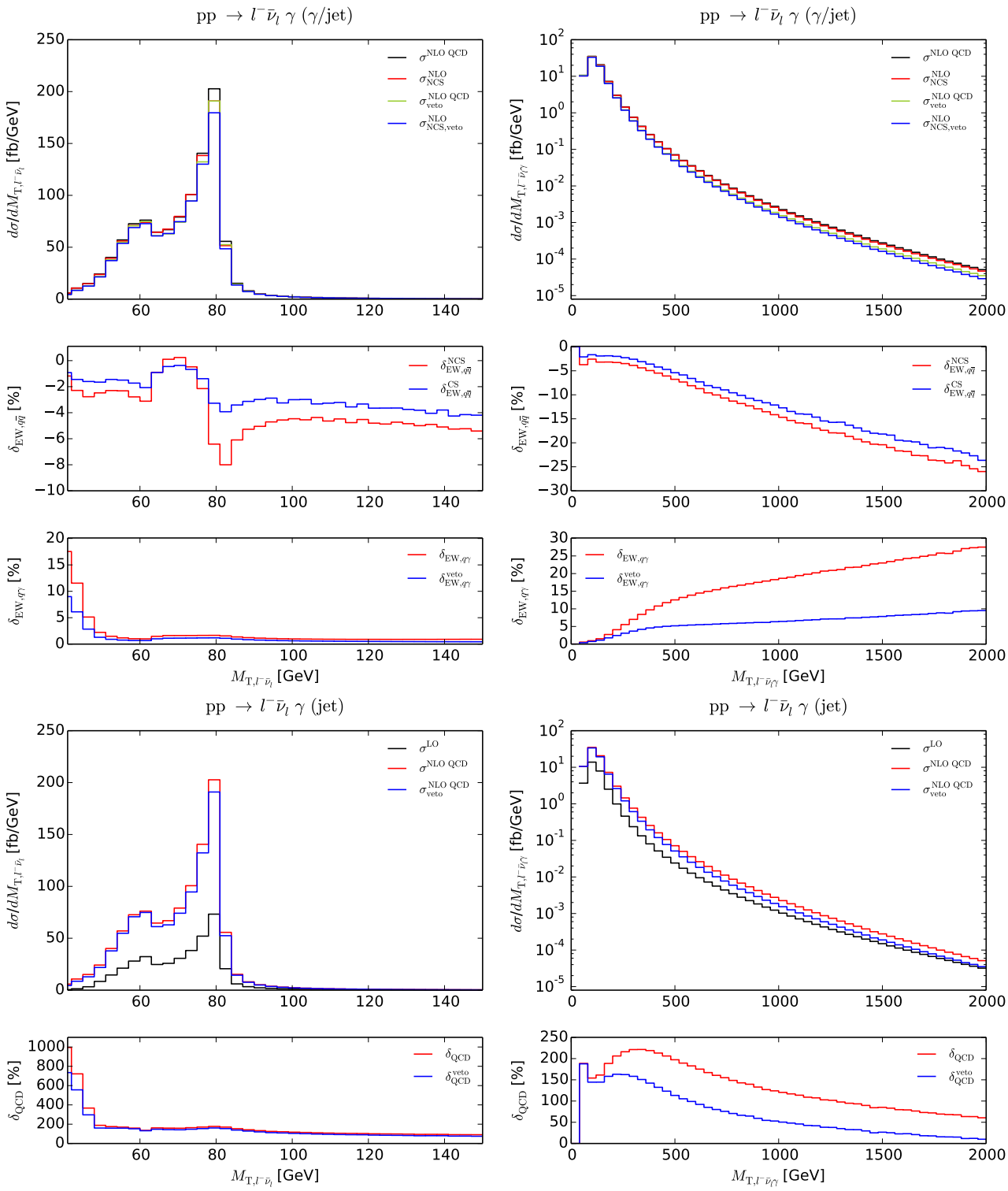

Figure C.2: Distribution in the transverse mass $M_{\mathrm{T},l^-\nu}$ of the charged lepton and neutrino pair (left) and distribution in the transverse three-body mass $M_{\mathrm{T},l^-\nu\gamma}$ of the charged lepton, the neutrino, and the hardest photon (right), including EW (top) and QCD corrections (bottom). For all corrections absolute (upper box) and relative corrections (lower boxes) are shown.

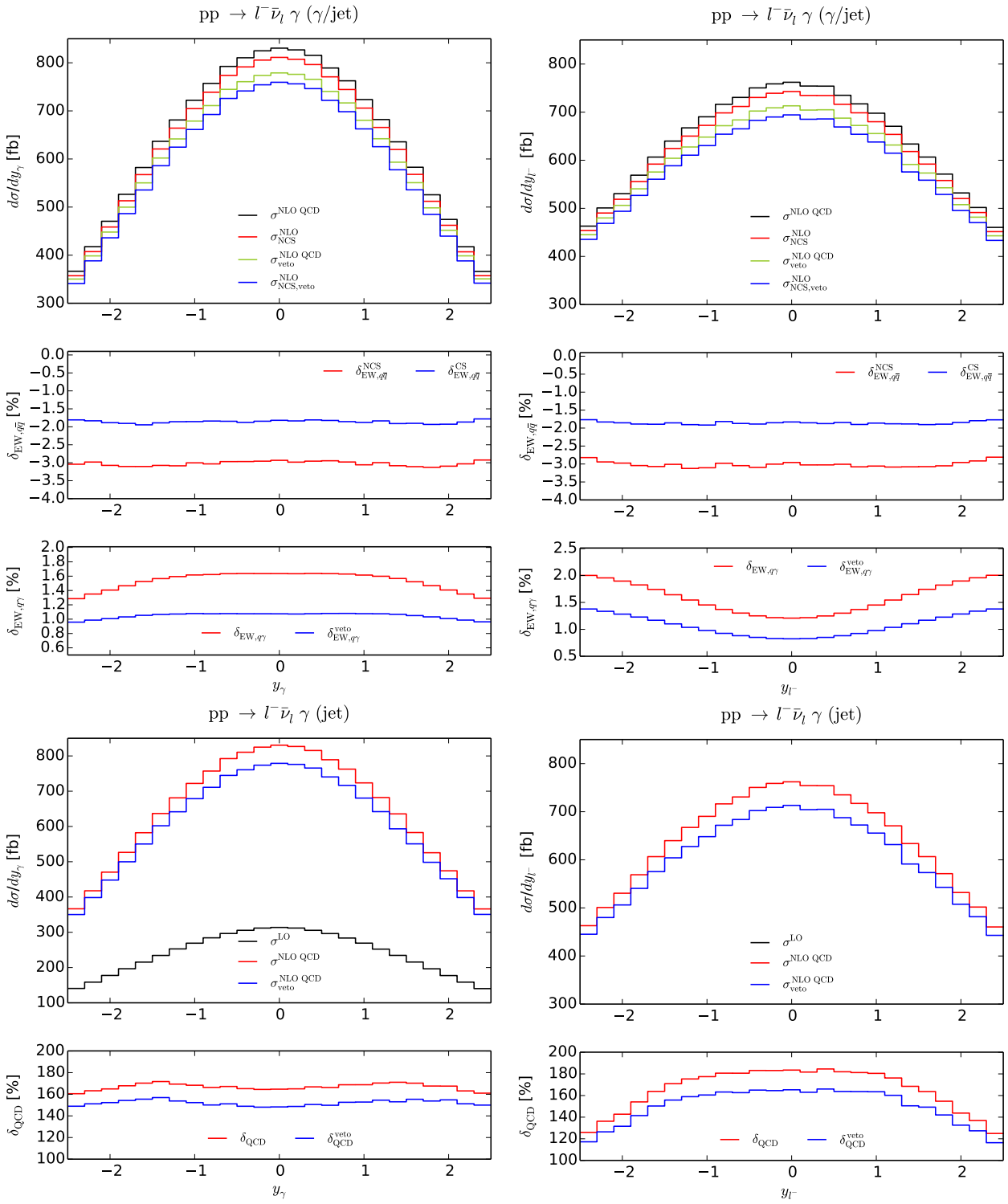

Figure C.3: Distributions in the rapidity y_γ of the photon (left) and the rapidity y_{l^-} of the charged lepton (right), including EW (top) and QCD corrections (bottom). For all corrections absolute (upper box) and relative corrections (lower boxes) are shown.

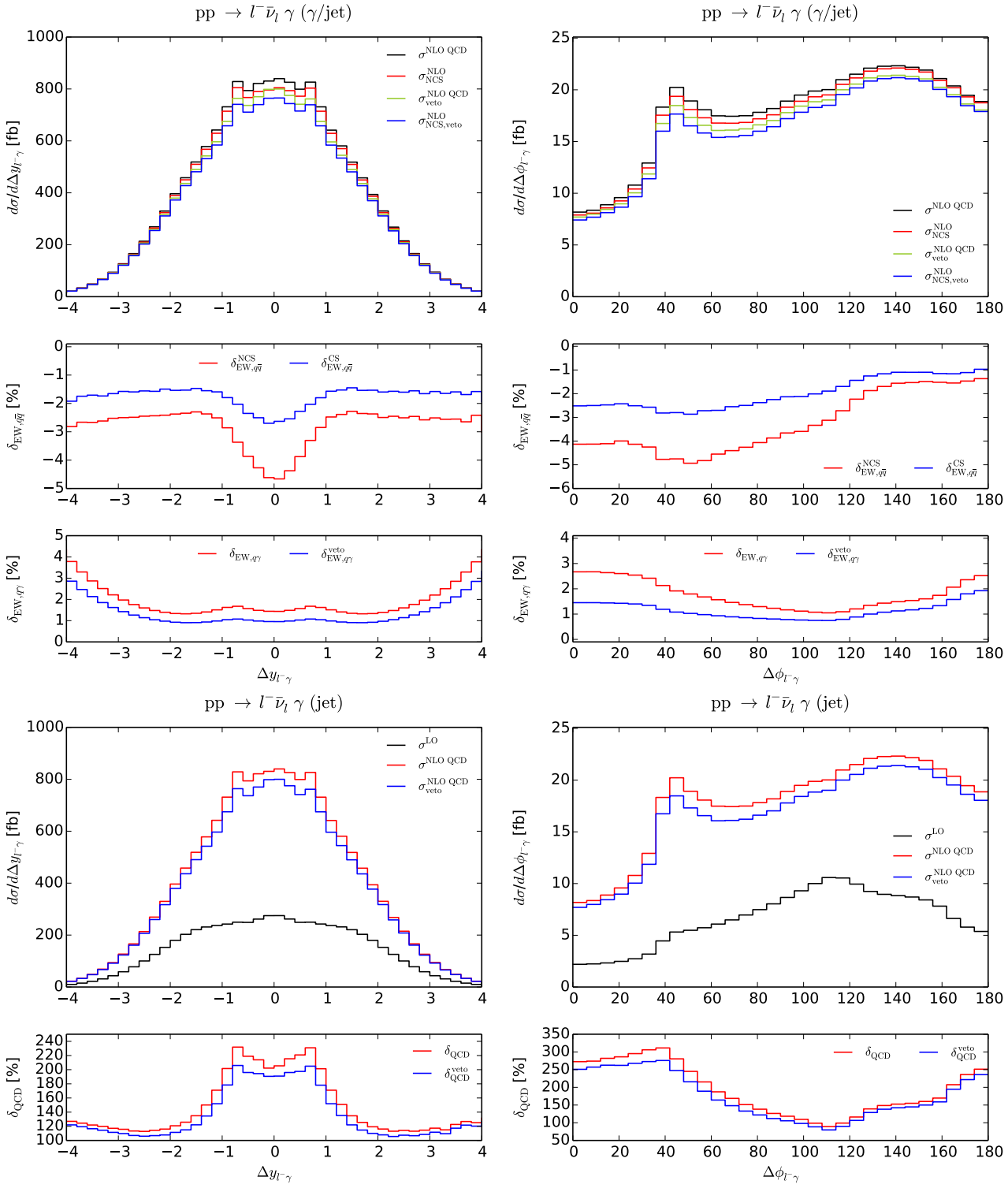

Figure C.4: Distributions in the rapidity difference $\Delta y_{l^-\gamma}$ (left) and the azimuthal-angle difference $\Delta\phi_{l^-\gamma}$ (right) of the charged lepton and the photon, including EW (top) and QCD corrections (bottom). For all corrections absolute (upper box) and relative corrections (lower boxes) are shown.

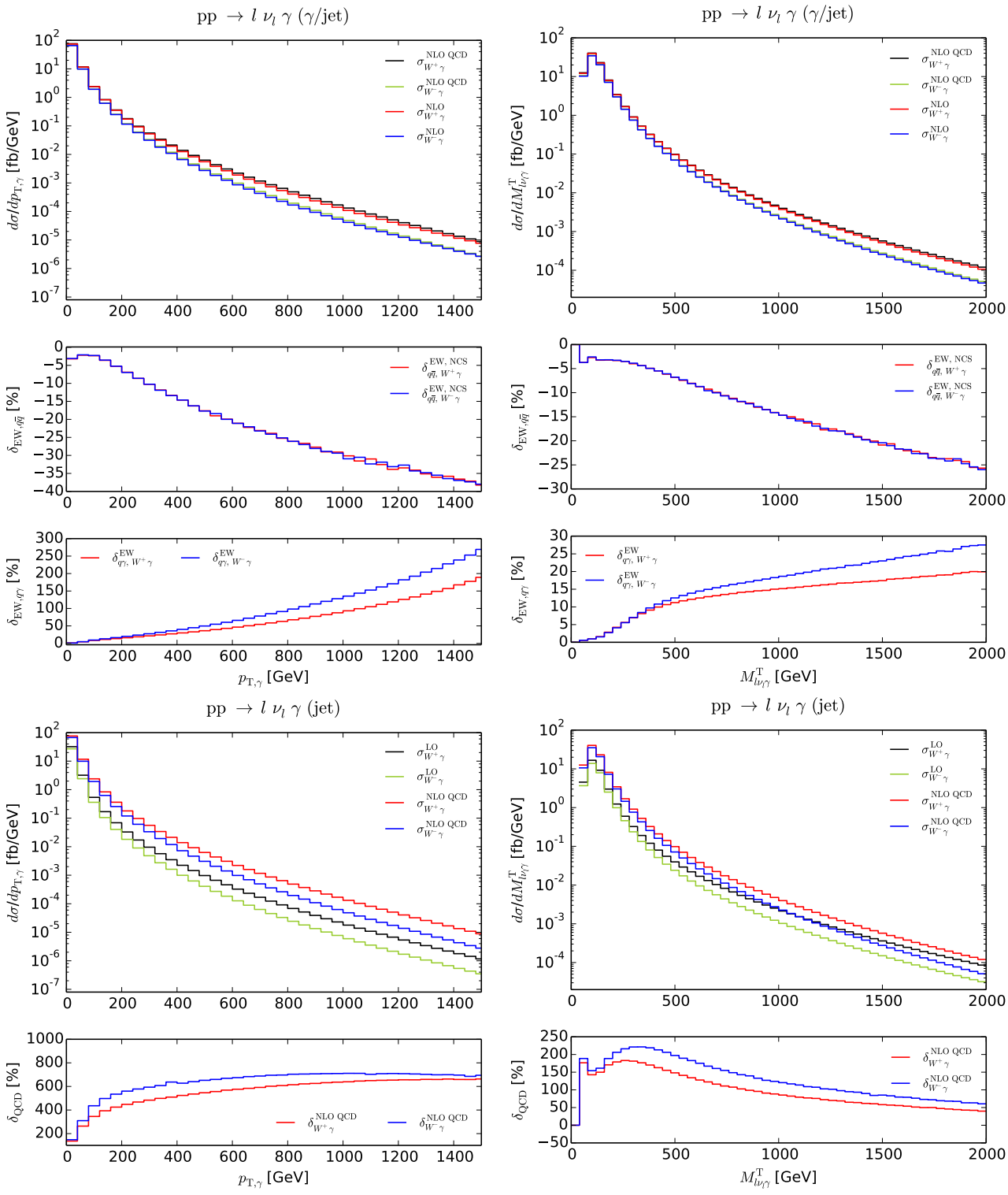

Figure C.5: Distributions in the transverse momentum p_{T} of the photon (left) and the transverse three-body mass $M_{\mathrm{T},l\nu\gamma}$ of the charged lepton, the neutrino, and the hardest photon (right), including EW (top) and QCD corrections (bottom). For all corrections absolute (large box) and relative corrections (small boxes) are shown.

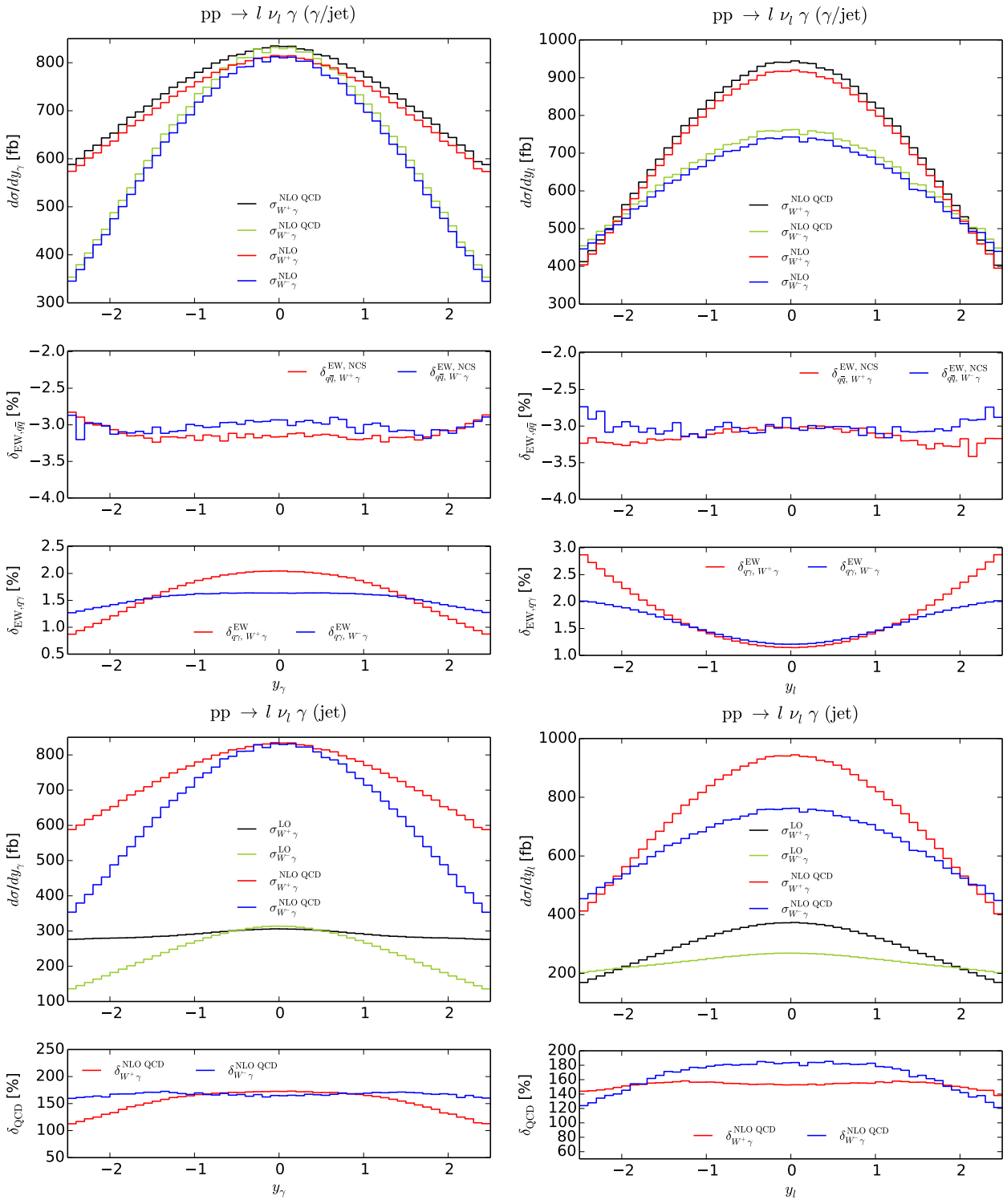

Figure C.6: Distributions in the rapidity y_γ of the photon (left) and the rapidity y_l of the charged lepton (right), including EW (top) and QCD corrections (bottom). For all corrections absolute (large box) and relative corrections (small boxes) are shown.

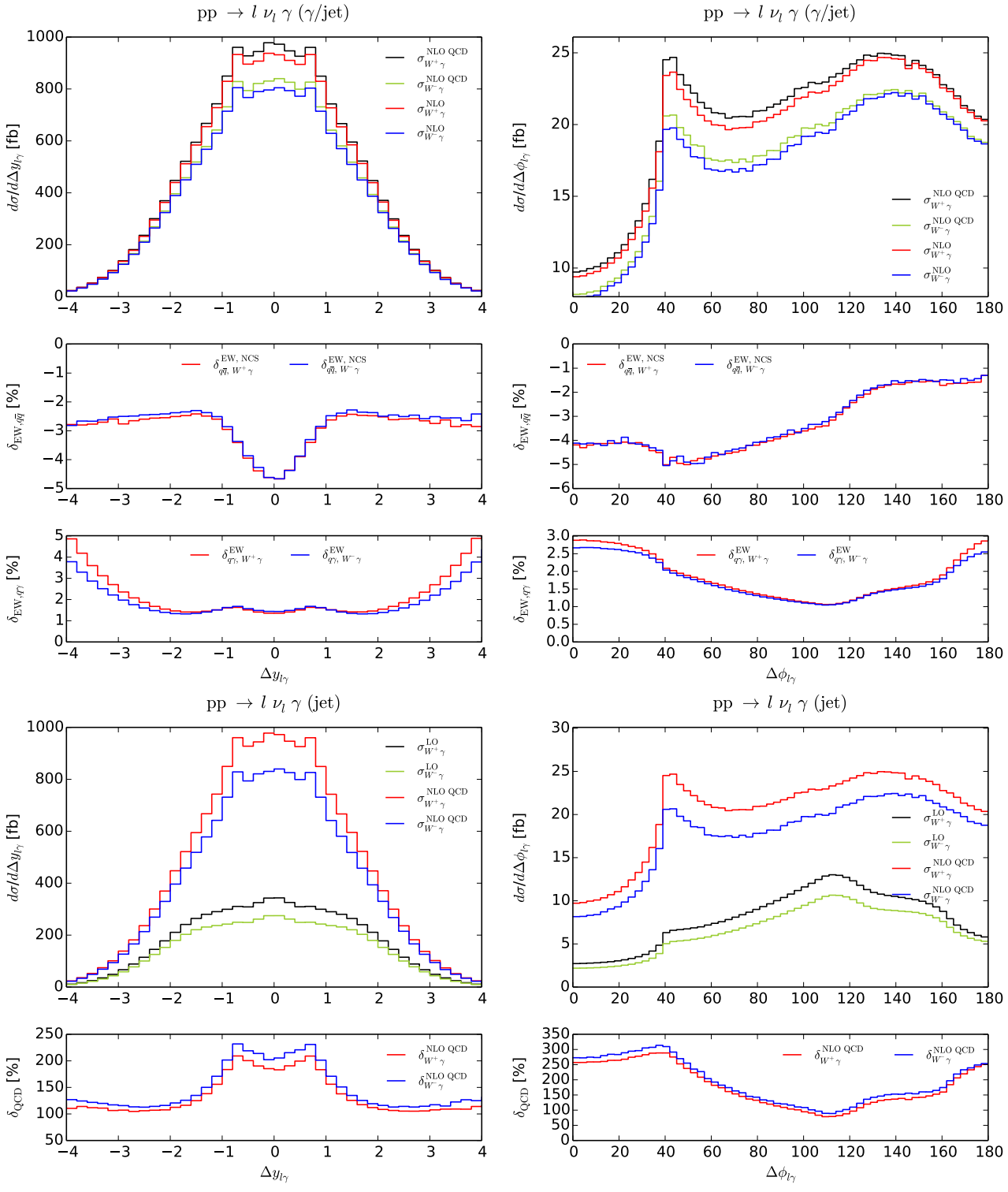

Figure C.7: Distributions in the rapidity difference $\Delta y_{l\gamma}$ (left) and the azimuthal-angle difference $\Delta\phi_{l\gamma}$ (right) of the charged lepton and the photon, including EW (top) and QCD corrections (bottom). For all corrections absolute (large box) and relative corrections (small boxes) are shown.

Appendix D

Distributions for $\mathrm{p\ p} \to l^+\ l^-\ \gamma + X$

In this chapter we list further distributions in various observables for $pp \to l^+l^-\gamma$ at a collider energy of 14 TeV. For each observable we show absolute plots for complete NLO and NLO QCD corrections (large boxes). The QCD NLO cross section and the complete NLO cross section are defined in Eqs. (4.3) and (4.1), respectively. In addition, we also present relative corrections for EW and QCD corrections. Due to the different final state of the $q\bar{q}$ and the $q\gamma$ channel we show these contributions apart from each other. The relative corrections are defined in Eq. (4.2). In case of the quark–antiquark-induced correction we show results for the collinear-safe and the non-collinear-safe case. For photon-induced and QCD corrections results are presented with and without the application of a jet veto at 100 GeV

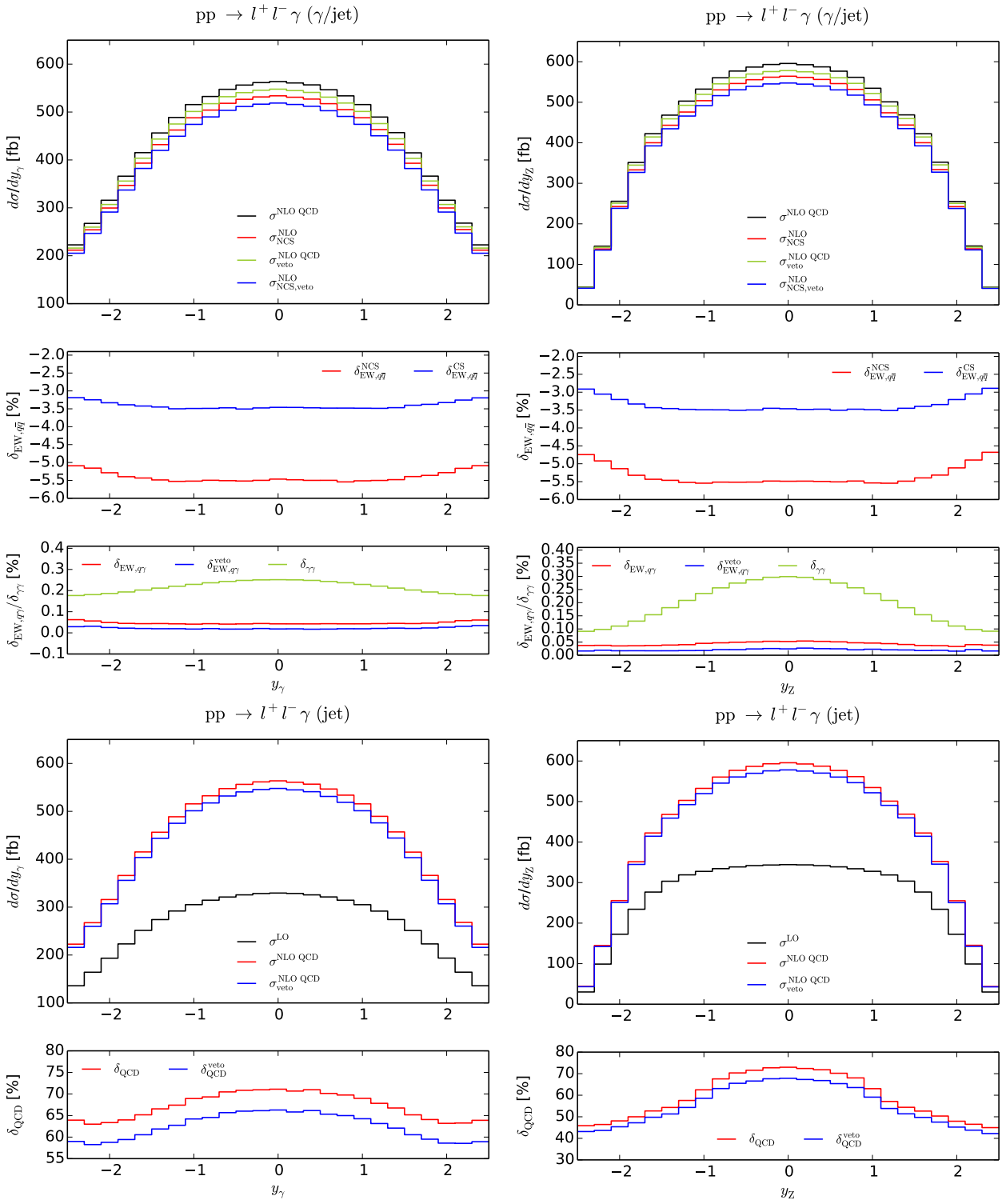

Figure D.1: Distributions in the rapidity y of the hardest photon (left) and the Z boson (right), including EW (top) and QCD corrections (bottom). The upper boxes show absolute predictions, the lower relative.

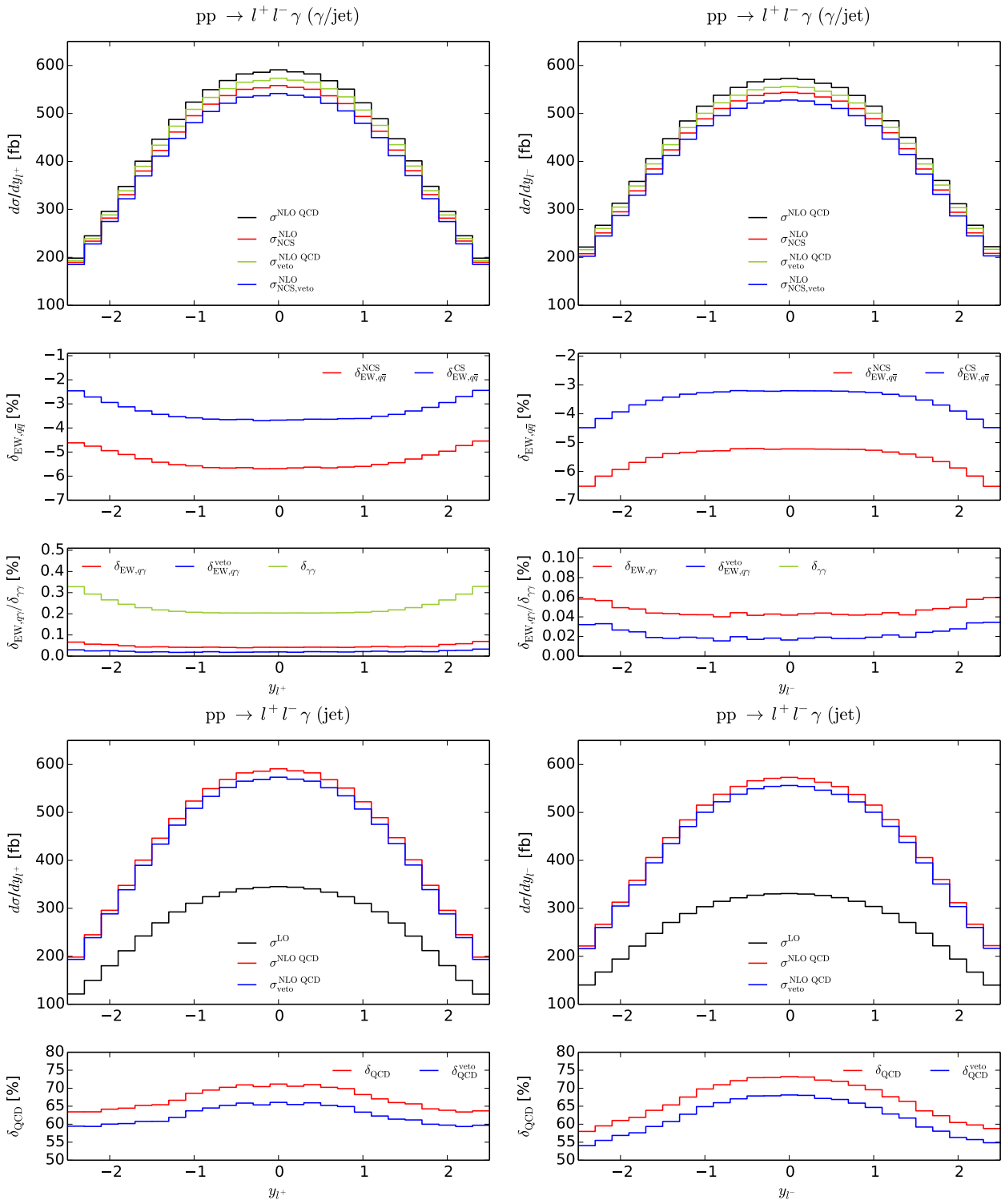

Figure D.2: Distributions in the rapidities $y_{l^\pm}$ of the two charged leptons, including EW (top) and QCD corrections (bottom). The upper boxes show absolute predictions, the lower relative.

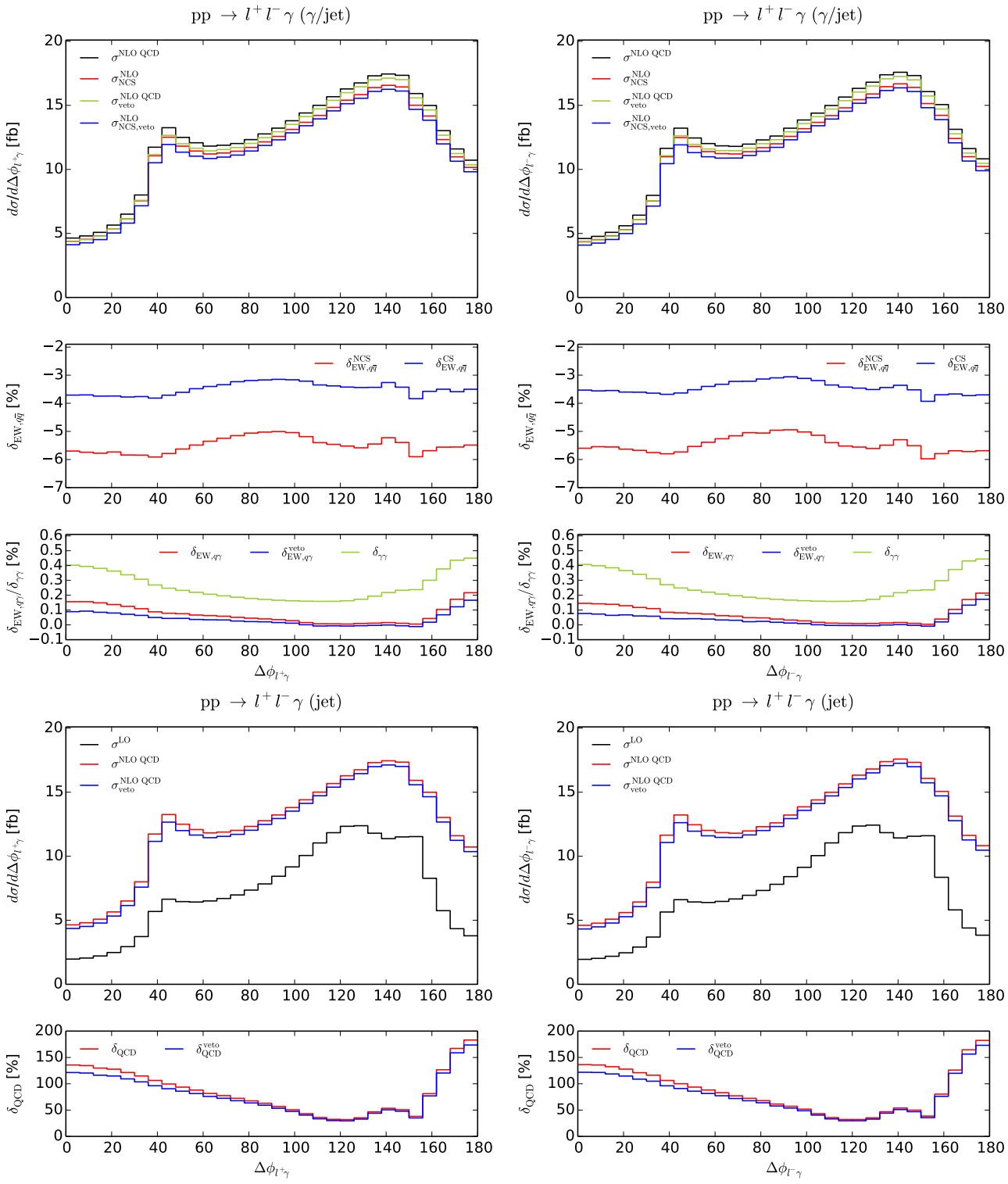

Figure D.3: Distributions in the azimuthal-angle differences $\Delta\phi_{l^\pm\gamma}$ between the charged lepton and the hardest photon, including EW (top) and QCD corrections (bottom). The upper boxes show absolute predictions, the lower relative.

List of Figures

Bibliography

[1] **ATLAS** Collaboration, G. Aad et al., *Observation of a new particle in the search for the Standard Model Higgs boson with the ATLAS detector at the LHC*, *Phys. Lett.* **B716** (2012) 1–29, [arXiv:1207.7214].

[2] O. W. Greenberg, *Spin and Unitary Spin Independence in a Paraquark Model of Baryons and Mesons*, *Phys. Rev. Lett.* **13** (1964) 598–602.

[3] M. Y. Han and Y. Nambu, *Three Triplet Model with Double SU(3) Symmetry*, *Phys. Rev.* **139** (1965) B1006–B1010.

[4] H. Fritzsch, M. Gell-Mann, and H. Leutwyler, *Advantages of the Color Octet Gluon Picture*, *Phys. Lett.* **B47** (1973) 365–368.

[5] S. L. Glashow, *Partial Symmetries of Weak Interactions*, *Nucl. Phys.* **22** (1961) 579–588.

[6] A. Salam, *Weak and Electromagnetic Interactions*, *Conf. Proc.* **C680519** (1968) 367–377.

[7] S. Weinberg, *A Model of Leptons*, *Phys. Rev. Lett.* **19** (1967) 1264–1266.

[8] S. L. Glashow, J. Iliopoulos, and L. Maiani, *Weak Interactions with Lepton-Hadron Symmetry*, *Phys. Rev.* **D2** (1970) 1285–1292.

[9] P. W. Higgs, *Broken symmetries, massless particles and gauge fields*, *Phys. Lett.* **12** (1964) 132–133.

[10] P. W. Higgs, *Broken Symmetries and the Masses of Gauge Bosons*, *Phys. Rev. Lett.* **13** (1964) 508–509.

[11] P. W. Higgs, *Spontaneous Symmetry Breakdown without Massless Bosons*, *Phys. Rev.* **145** (1966) 1156–1163.

[12] F. Englert and R. Brout, *Broken Symmetry and the Mass of Gauge Vector Mesons*, *Phys. Rev. Lett.* **13** (1964) 321–323.

[13] T. W. B. Kibble, *Symmetry breaking in non Abelian gauge theories*, *Phys. Rev.* **155** (1967) 1554–1561.

[14] M. S. Neubauer, *Diboson production at colliders*, *Ann.Rev.Nucl.Part.Sci.* **61** (2011) 223–250.

[15] **D0 Collaboration** Collaboration, V. M. Abazov et al., *$W\gamma$ production and limits on anomalous $WW\gamma$ couplings in $p\bar{p}$ collisions*, *Phys.Rev.Lett.* **107** (2011) 241803, [arXiv:1109.4432].

[16] **CMS Collaboration** Collaboration, S. Chatrchyan et al., *Measurement of the W gamma and Z gamma inclusive cross sections in pp collisions at $\sqrt{s}$ = 7 TeV and limits on anomalous triple gauge boson couplings*, *Phys.Rev.* **D89** (2014) 092005, [arXiv:1308.6832].

[17] **ATLAS Collaboration** Collaboration, G. Aad et al., *Measurements of $W\gamma$ and $Z\gamma$ production in pp collisions at $\sqrt{s} = 7$ TeV with the ATLAS detector at the LHC*, *Phys.Rev.* **D87** (2013), no. 11 112003, [arXiv:1302.1283].

[18] **ATLAS Collaboration** Collaboration, G. Aad et al., *Search for new resonances in $W\gamma$ and $Z\gamma$ final states in pp collisions at $\sqrt{s} = 8$ TeV with the ATLAS detector*, *Phys.Lett.* **B738** (2014) 428–447, [arXiv:1407.8150].

[19] M. Schott and J. Zhu, *Diboson production in proton-proton collisions at $\sqrt{s} = 7$ TeV*, *Int.J.Mod.Phys.* **A29** (2014), no. 26 1430053, [arXiv:1406.7731].

[20] P. J. Fox, R. Harnik, J. Kopp, and Y. Tsai, *Missing Energy Signatures of Dark Matter at the LHC*, *Phys. Rev.* **D85** (2012) 056011, [arXiv:1109.4398].

[21] G. Belanger, M. Heikinheimo, and V. Sanz, *Model-Independent Bounds on Squarks from Monophoton Searches*, *JHEP* **08** (2012) 151, [arXiv:1205.1463].

[22] E. Gabrielli, M. Heikinheimo, B. Mele, and M. Raidal, *Dark photons and resonant monophoton signatures in Higgs boson decays at the LHC*, *Phys. Rev.* **D90** (2014), no. 5 055032, [arXiv:1405.5196].

[23] F. Maltoni, A. Martini, K. Mawatari, and B. Oexl, *Signals of a superlight gravitino at the LHC*, *JHEP* **04** (2015) 021, [arXiv:1502.01637].

[24] **CDF** Collaboration, T. Aaltonen et al., *Search for large extra dimensions in final states containing one photon or jet and large missing transverse energy produced in $p\bar{p}$ collisions at $\sqrt{s}$ = 1.96-TeV*, *Phys. Rev. Lett.* **101** (2008) 181602, [arXiv:0807.3132].

[25] **D0** Collaboration, V. M. Abazov et al., *Search for large extra dimensions via single photon plus missing energy final states at $\sqrt{s}$ = 1.96-TeV*, *Phys. Rev. Lett.* **101** (2008) 011601, [arXiv:0803.2137].

[26] **ATLAS** Collaboration, G. Aad et al., *Search for new phenomena in events with a photon and missing transverse momentum in pp collisions at $\sqrt{s} = 8$ TeV with the ATLAS detector*, *Phys. Rev.* **D91** (2015), no. 1 012008, [arXiv:1411.1559]. [Erratum: Phys. Rev.D92,no.5,059903(2015)].

[27] **CMS** Collaboration, V. Khachatryan et al., *Search for new phenomena in monophoton final states in proton-proton collisions at $\sqrt{s}$ = 8 TeV*, arXiv:1410.8812.

[28] B. C. Allanach, J. P. Skittrall, and K. Sridhar, *Z boson decay to photon plus Kaluza-Klein graviton in large extra dimensions*, *JHEP* **11** (2007) 089, [arXiv:0705.1953].

[29] A. Freitas and P. Schwaller, *Multi-Photon Signals from Composite Models at LHC*, *JHEP* **01** (2011) 022, [arXiv:1010.2528].

[30] K. D. Lane and E. Eichten, *Two Scale Technicolor*, *Phys. Lett.* **B222** (1989) 274.

[31] K. Hagiwara, R. D. Peccei, D. Zeppenfeld, and K. Hikasa, *Probing the weak boson sector in $e^+e^- \to W^+W^-$*, *Nucl.Phys.* **B282** (1987) 253–307.

[32] U. Baur, T. Han, and J. Ohnemus, *QCD corrections to hadronic $W\gamma$ production with nonstandard $WW\gamma$ couplings*, *Phys.Rev.* **D48** (1993) 5140–5161, [hep-ph/9305314].

[33] D. De Florian and A. Signer, *W gamma and Z gamma production at hadron colliders*, *Eur.Phys.J.* **C16** (2000) 105–114, [hep-ph/0002138].

[34] **CDF** Collaboration, T. Aaltonen et al., *Limits on Anomalous Trilinear Gauge Couplings in $Z\gamma$ Events from $p\bar{p}$ Collisions at $\sqrt{s} = 1.96$ TeV*, *Phys. Rev. Lett.* **107** (2011) 051802, [arXiv:1103.2990].

[35] **D0** Collaboration, V. M. Abazov et al., *$Z\gamma$ production and limits on anomalous $ZZ\gamma$ and $Z\gamma\gamma$ couplings in $p\bar{p}$ collisions at $\sqrt{s} = 1.96$ TeV*, *Phys. Rev.* **D85** (2012) 052001, [arXiv:1111.3684].

[36] **CMS** Collaboration, V. Khachatryan et al., *Measurement of the $Z\gamma$ production cross section in pp collisions at 8 TeV and search for anomalous triple gauge boson couplings*, *JHEP* **04** (2015) 164, [arXiv:1502.05664].

[37] R. Brown, D. Sahdev, and K. Mikaelian, $W^{\pm}$ *Z0 and* $W^{\pm}$ γ *Pair Production in Neutrino e, p p, and anti-p p Collisions*, *Phys.Rev.* **D20** (1979) 1164.

[38] F. M. Renard, *Tests of Neutral Gauge Boson Selfcouplings With $e^+e^- \to \gamma Z$*, *Nucl. Phys.* **B196** (1982) 93.

[39] J. Smith, D. Thomas, and W. van Neerven, *QCD Corrections to the Reaction $p\bar{p} \to W\gamma$ X*, *Z.Phys.* **C44** (1989) 267.

[40] J. Ohnemus, *Order α_s calculations of hadronic $W^{\pm}\gamma$ and $Z\gamma$ production*, *Phys.Rev.* **D47** (1993) 940–955.

[41] J. Ohnemus, *Hadronic $Z\gamma$ production with QCD corrections and leptonic decays*, *Phys. Rev.* **D51** (1995) 1068–1076, [hep-ph/9407370].

[42] U. Baur, T. Han, and J. Ohnemus, *QCD corrections and anomalous couplings in $Z\gamma$ production at hadron colliders*, *Phys. Rev.* **D57** (1998) 2823–2836, [hep-ph/9710416].

[43] J. M. Campbell, R. K. Ellis, and C. Williams, *Vector boson pair production at the LHC*, *JHEP* **1107** (2011) 018, [arXiv:1105.0020].

[44] M. Grazzini, S. Kallweit, and D. Rathlev, *$W\gamma$ and $Z\gamma$ production at the LHC in NNLO QCD*, *JHEP* **07** (2015) 085, [arXiv:1504.01330].

[45] M. Grazzini, S. Kallweit, D. Rathlev, and A. Torre, *$Z\gamma$ production at hadron colliders in NNLO QCD*, *Phys. Lett.* **B731** (2014) 204–207, [arXiv:1309.7000].

[46] W. Beenakker, A. Denner, S. Dittmaier, R. Mertig, and T. Sack, *High-energy approximation for on-shell W pair production*, *Nucl.Phys.* **B410** (1993) 245–279.

[47] M. Beccaria, G. Montagna, F. Piccinini, F. Renard, and C. Verzegnassi, *Rising bosonic electroweak virtual effects at high-energy e+ e- colliders*, *Phys.Rev.* **D58** (1998) 093014, [hep-ph/9805250].

[48] P. Ciafaloni and D. Comelli, *Sudakov enhancement of electroweak corrections*, *Phys.Lett.* **B446** (1999) 278–284, [hep-ph/9809321].

[49] J. H. Kühn and A. Penin, *Sudakov logarithms in electroweak processes*, hep-ph/9906545.

[50] V. S. Fadin, L. N. Lipatov, A. D. Martin, and M. Melles, *Resummation of double logarithms in electroweak high-energy processes*, *Phys. Rev.* **D61** (2000) 094002, [hep-ph/9910338].

[51] A. Denner and S. Pozzorini, *One loop leading logarithms in electroweak radiative corrections. 1. Results*, *Eur.Phys.J.* **C18** (2001) 461–480, [hep-ph/0010201].

[52] E. Accomando, A. Denner, and S. Pozzorini, *Electroweak correction effects in gauge boson pair production at the CERN LHC*, *Phys.Rev.* **D65** (2002) 073003, [hep-ph/0110114].

[53] W. Hollik and C. Meier, *Electroweak corrections to gamma Z production at hadron colliders*, *Phys. Lett.* **B590** (2004) 69–75, [hep-ph/0402281].

[54] E. Accomando, A. Denner, and C. Meier, *Electroweak corrections to $W\gamma$ and $Z\gamma$ production at the LHC*, *Eur.Phys.J.* **C47** (2006) 125–146, [hep-ph/0509234].

[55] E. W. N. Glover and A. G. Morgan, *Measuring the photon fragmentation function at LEP*, *Z. Phys.* **C62** (1994) 311–322.

[56] E. W. N. Glover and A. G. Morgan, *The Photon + 1 jet event rate with the cone algorithm in hadronic events at LEP*, *Phys. Lett.* **B334** (1994) 208–214.

[57] S. Frixione, *Isolated photons in perturbative QCD*, *Phys.Lett.* **B429** (1998) 369–374, [hep-ph/9801442].

[58] S. Dittmaier, *Weyl-van der Waerden formalism for helicity amplitudes of massive particles*, *Phys.Rev.* **D59** (1998) 016007, [hep-ph/9805445].

[59] A. Denner, S. Dittmaier, and L. Hofer, *COLLIER - A fortran-library for one-loop integrals*, *PoS* **LL2014** (2014) 071, [arXiv:1407.0087].

[60] A. Denner and S. Dittmaier, *Reduction of one loop tensor five point integrals*, *Nucl.Phys.* **B658** (2003) 175–202, [hep-ph/0212259].

[61] A. Denner and S. Dittmaier, *Reduction schemes for one-loop tensor integrals*, *Nucl.Phys.* **B734** (2006) 62–115, [hep-ph/0509141].

[62] A. Denner and S. Dittmaier, *Scalar one-loop 4-point integrals*, *Nucl.Phys.* **B844** (2011) 199–242, [arXiv:1005.2076].

[63] T. Hahn, *Generating Feynman diagrams and amplitudes with FeynArts 3*, *Comput.Phys.Commun.* **140** (2001) 418–431, [hep-ph/0012260].

[64] T. Hahn and C. Schappacher, *The Implementation of the minimal supersymmetric standard model in FeynArts and FormCalc*, *Comput.Phys.Commun.* **143** (2002) 54–68, [hep-ph/0105349].

[65] T. Hahn and M. Perez-Victoria, *Automatized one loop calculations in four-dimensions and D-dimensions*, *Comput.Phys.Commun.* **118** (1999) 153–165, [hep-ph/9807565].

[66] S. Dittmaier and M. Roth, *LUSIFER: A LUcid approach to SIx FERmion production*, *Nucl.Phys.* **B642** (2002) 307–343, [hep-ph/0206070].

[67] G. P. Lepage, *A New Algorithm for Adaptive Multidimensional Integration*, *J.Comput.Phys.* **27** (1978) 192.

[68] G. P. Lepage, *VEGAS: AN ADAPTIVE MULTIDIMENSIONAL INTEGRATION PROGRAM*, . CLNS-80/447.

[69] A. Denner, S. Dittmaier, M. Hecht, and C. Pasold, *NLO QCD and electroweak corrections to $W + \gamma$ production with leptonic W-boson decays*, *JHEP* **04** (2015) 018, [arXiv:1412.7421].

[70] A. Denner, S. Dittmaier, M. Hecht, and C. Pasold, *NLO QCD and electroweak corrections to $Z + \gamma$ production with leptonic Z-boson decays*, arXiv:1510.08742.

[71] **SLD Electroweak Group, DELPHI, ALEPH, SLD, SLD Heavy Flavour Group, OPAL, LEP Electroweak Working Group, L3** Collaboration, S. Schael et al., *Precision electroweak measurements on the Z resonance*, *Phys. Rept.* **427** (2006) 257–454, [hep-ex/0509008].

[72] J. Goldstone, A. Salam, and S. Weinberg, *Broken Symmetries*, *Phys. Rev.* **127** (1962) 965–970.

[73] A. Denner, *Techniques for calculation of electroweak radiative corrections at the one loop level and results for W physics at LEP-200*, *Fortsch.Phys.* **41** (1993) 307–420, [arXiv:0709.1075].

[74] L. D. Faddeev and V. N. Popov, *Feynman Diagrams for the Yang-Mills Field*, *Phys. Lett.* **B25** (1967) 29–30.

[75] A. Denner, S. Dittmaier, M. Roth, and D. Wackeroth, *Predictions for all processes e+ e- —> 4 fermions + gamma*, *Nucl.Phys.* **B560** (1999) 33–65, [hep-ph/9904472].

[76] A. Denner, S. Dittmaier, M. Roth, and L. H. Wieders, *Electroweak corrections to charged-current e+ e—> 4 fermion processes: Technical details and further results*, *Nucl. Phys.* **B724** (2005) 247–294, [hep-ph/0505042]. [Erratum: Nucl. Phys.B854,504(2012)].

[77] A. Denner and S. Dittmaier, *The Complex-mass scheme for perturbative calculations with unstable particles*, *Nucl.Phys.Proc.Suppl.* **160** (2006) 22–26, [hep-ph/0605312].

[78] M. L. Ciccolini, S. Dittmaier, and M. Krämer, *Electroweak radiative corrections to associated WH and ZH production at hadron colliders*, *Phys. Rev.* **D68** (2003) 073003, [hep-ph/0306234].

[79] A. Sirlin, *Radiative Corrections in the* $\mathrm{SU(2)_L} \times \mathrm{U(1)}$ *Theory: A Simple Renormalization Framework*, *Phys. Rev.* **D22** (1980) 971–981.

[80] R. P. Feynman, *Very high-energy collisions of hadrons*, *Phys. Rev. Lett.* **23** (1969) 1415–1417.

[81] J. D. Bjorken and E. A. Paschos, *Inelastic Electron Proton and gamma Proton Scattering, and the Structure of the Nucleon*, *Phys. Rev.* **185** (1969) 1975–1982.

[82] A. Huss, *Mixed QCD-electroweak $\mathcal{O}(\alpha_s\alpha)$ corrections to Drell-Yan processes in the resonance region*. PhD thesis, Freiburg U., 2014.

[83] T. Kinoshita, *Mass singularities of Feynman amplitudes*, *J.Math.Phys.* **3** (1962) 650–677.

[84] T. Lee and M. Nauenberg, *Degenerate Systems and Mass Singularities*, *Phys.Rev.* **133** (1964) B1549–B1562.

[85] **NNPDF Collaboration** Collaboration, R. D. Ball et al., *Parton distributions with QED corrections*, *Nucl.Phys.* **B877** (2013) 290–320, [arXiv:1308.0598].

[86] K.-P. Diener, S. Dittmaier, and W. Hollik, *Electroweak higher-order effects and theoretical uncertainties in deep-inelastic neutrino scattering*, *Phys.Rev.* **D72** (2005) 093002, [hep-ph/0509084].

[87] S. Catani and M. H. Seymour, *A general algorithm for calculating jet cross sections in NLO QCD*, *Nucl. Phys.* **B485** (1997) 291–419, [hep-ph/9605323].

[88] S. Catani, S. Dittmaier, M. H. Seymour, and Z. Trocsanyi, *The Dipole formalism for next-to-leading order QCD calculations with massive partons*, *Nucl.Phys.* **B627** (2002) 189–265, [hep-ph/0201036].

[89] S. Dittmaier, *A General approach to photon radiation off fermions*, *Nucl.Phys.* **B565** (2000) 69–122, [hep-ph/9904440].

[90] S. Dittmaier, A. Kabelschacht, and T. Kasprzik, *Polarized QED splittings of massive fermions and dipole subtraction for non-collinear-safe observables*, *Nucl.Phys.* **B800** (2008) 146–189, [arXiv:0802.1405].

[91] A. Denner, S. Dittmaier, T. Kasprzik, and A. Mück, *Electroweak corrections to W + jet hadroproduction including leptonic W-boson decays*, *JHEP* **0908** (2009) 075, [arXiv:0906.1656].

[92] A. Denner, S. Dittmaier, T. Kasprzik, and A. Mück, *Electroweak corrections to dilepton + jet production at hadron colliders*, *JHEP* **06** (2011) 069, [arXiv:1103.0914].

[93] A. Denner, S. Dittmaier, T. Kasprzik, and A. Mück, *Electroweak corrections to monojet production at the LHC*, *Eur. Phys. J.* **C73** (2013), no. 2 2297, [arXiv:1211.5078].

[94] A. Denner, S. Dittmaier, T. Gehrmann, and C. Kurz, *Electroweak corrections to hadronic event shapes and jet production in e+e- annihilation*, *Nucl.Phys.* **B836** (2010) 37–90, [arXiv:1003.0986].

[95] **ALEPH Collaboration** Collaboration, D. Buskulic et al., *First measurement of the quark to photon fragmentation function*, *Z. Phys.* **C69** (1996) 365–378.

[96] J. Küblbeck, M. Böhm, and A. Denner, *Feyn Arts: Computer Algebraic Generation of Feynman Graphs and Amplitudes*, *Comput.Phys.Commun.* **60** (1990) 165–180.

[97] **Particle Data Group** Collaboration, J. Beringer et al., *Review of Particle Physics (RPP)*, *Phys.Rev.* **D86** (2012) 010001.

[98] D. Bardin, A. Leike, T. Riemann, and M. Sachwitz, *Energy Dependent Width Effects in e+ e- Annihilation Near the Z Boson Pole*, *Phys.Lett.* **B206** (1988) 539–542.

[99] L. J. Dixon, Z. Kunszt, and A. Signer, *Vector boson pair production in hadronic collisions at order α_s : Lepton correlations and anomalous couplings*, *Phys.Rev.* **D60** (1999) 114037, [hep-ph/9907305].

[100] S. Haywood et al., *Electroweak physics*, hep-ph/0003275.

[101] M. Grazzini, *Vector-boson pair production at NNLO*, *PoS* **LL2014** (2014) 027, [arXiv:1407.1618].

[102] U. Baur, S. Errede, and G. L. Landsberg, *Rapidity correlations in $W\gamma$ production at hadron colliders*, *Phys.Rev.* **D50** (1994) 1917–1930, [hep-ph/9402282].

[103] Z. Bern et al., *Left-Handed W Bosons at the LHC*, *Phys.Rev.* **D84** (2011) 034008, [arXiv:1103.5445].

[104] C. Berger et al., *Next-to-Leading Order QCD Predictions for W+3-Jet Distributions at Hadron Colliders*, *Phys.Rev.* **D80** (2009) 074036, [arXiv:0907.1984].

[105] F. James, *Monte carlo theory and practice*, *Reports on Progress in Physics* **43** (1980), no. 9 1145.

[106] M. Roth, *Precise predictions for four fermion production in electron positron annihilation*. PhD thesis, Zurich, ETH, 1999. hep-ph/0008033.

[107] G. Passarino and M. Veltman, *One Loop Corrections for e^+ e^- Annihilation Into μ^+ μ^- in the Weinberg Model*, *Nucl.Phys.* **B160** (1979) 151.

List of publications

Publications on the results presented in this thesis:

- A. Denner, S. Dittmaier, M. Hecht and C. Pasold, *NLO QCD and electroweak corrections to $W + \gamma$ production with leptonic W-boson decays*, *JHEP* **1504** (2015) 018, `arXiv:1412.7421`
- A. Denner, S. Dittmaier, M. Hecht and C. Pasold, *NLO QCD and electroweak corrections to $Z + \gamma$ production with leptonic Z-boson decays*, `arXiv:1510.08742`

Earlier publications:

- T. Flacke and C. Pasold, *Constraints on split-UED from Electroweak Precision Tests*, Phys. Rev. D **85** (2012) 126007, `arXiv:1111.7250`

Talks given on various subjects of this thesis:

- Terascale Alliance Annual Workshop 2014, DESY Hamburg (02.12.2014)
- DPG-Frühjahrstagung 2014, Johannes Gutenberg-Universität Mainz (27.03.2014)

Danksagung

Obwohl naturgemäß auf dem Titelblatt einer Dissertation nur ein einziger Name steht, gibt es doch eine ganze Reihe von Personen, ohne die es diese Arbeit niemals gegeben hätte. Für die Zeit der Promotion ist es daher unerlässlich, dass man auf das Verständnis und den Rückhalt zahlreicher Personen zählen kann. All diesen Personen möchte ich an dieser Stelle erwähnen und mich für deren Unterstützung (ob nun bewusst oder unbewusst) bedanken.

Mein Dank gilt zunächst Prof. Dr. Ansgar Denner, der mir die Promotion innerhalb seiner Arbeitsgruppe erst ermöglicht hat, und mich während der gesamten Zeit mit sehr viel Geduld, stets einem offenem Ohr und unentbehrlichen Tipps begleitet und unterstützt hat. Weiterhin gilt mein Dank an Dr. Robert Feger und Jean-Nicolas Lang, die mich bei meinen Kämpfen mit Fortran bzw. Python permanent unterstützt haben und durch die ich in zahlreichen Diskussionen sehr viel lernen und Zeit sparen konnte.

Ebenfalls bedanken möchte ich mich bei Prof. Dr. Stefan Dittmaier und Markus Hecht als Mitglieder Wgamma- und Zgamma-Crew für die angenehme und erfolgreiche Zusammenarbeit, den Aufenthalt in Freiburg sowie die unglaubliche Geduld während der zahlreichen Vergleiche zur Fehlersuche und in den langen Telefonkonferenzen.

In diesem abschließenden Absatz möchte ich all denen widmen, die mir in der Welt fernab der Physik und der fachlichen Probleme Rückhalt gegeben und mich motiviert haben. Ein sehr großer Dank geht dabei an meine Eltern, die mich über die gesamte Zeit bedingungslos unterstützt, motiviert und (falls notwendig) aufgebaut haben. Abschließend möchte ich hier auch meine engen Freunde erwähnen, die mich in dieser spannenden und herausfordernden Zeit abseits des universitären Alltags begleitet, unterstützt und gut dosiert für Ablenkung gesorgt haben. Mein Dank geht an: RK, AK, SL, JL, SS, CP, DM, KG, SG.